Delft University Of Technology
Master Degree in Sustainable Energy Technology

Probabilistic Design of Airfoils for Horizontal Axis Wind Turbines

Piero Mazza
Delft - 11/03/2020

Delft University of Technology
Master Degree in Sustainable Energy Technology

Probabilistic Design of Airfoil for Horizontal Axis Wind Turbine

Thesis Committee:
Prof.dr. S.J. Watson
Dr.ir W.A. Timmer
Dr.ir G. La Rocca

Supervisor:
Dr. R.B.S Pereira
Candidate:
Piero Mazza

Delft - 11/03/2020

ABSTRACT

This work follows the wind energy airfoil probabilistic design approach presented in [R. Pereira et al, 2018, IOP Conf. Series: Journal of Physics 1037 (2018) 022042, 'Probabilistic Design of Airfoil for Horizontal Axis Wind Turbines']. This approach allows to derive a probability density function which gives an estimation of how much the angle of attack is likely to fluctuate, according to the considered non-uniform perturbations in the wind speed. Several combinations of the perturbation sources are possible in practice as well as several extents of each perturbation source. A probabilistic design space mapping will be carried out to evaluate what wind situations are possible in practice and how much each specific wind situation is likely to occur. The proposed model will also be validated by employing the aero-elastic simulation tool: FAST. Finally, the probabilistic approach will be used to design airfoils and in particular it will be used to optimize the airfoil aerodynamic performance over the operational range of angles of attack. The airfoil optimization will be performed with the genetic multi-objective optimization tool: Optiflow, for different relative thicknesses as well as using different cost functions.

Acknowledgments

'A window can't close your mind in,
the future might be old to the eyes of those who dream..

All the roads that separate
All the songs that mitigate
Love and Hate are glued in the heart
All the power of the drum
All the flair of the guitar
It's the strings that touch your heart'

Through a Window

Un grazie infinito va, e andrà sempre, alla mia famiglia tutta e in particolare ai miei genitori, per il supporto incodizionato che mi hanno costantemente riservato. Se dovessi scrivere una seconda tesi elencando passo passo tutti i momenti in cui sono stati determinanti non basterebbe il tempo che ho dedicato a questo lavoro. Le scelte che sto prendendo mi stanno portando lontano, ma sappiamo tutti che la parola 'casa' per me avrà sempre un solo significato.

A special 'obrigado' goes to Ricardo Pereira, for all the hours spent answering to all my questions and stimulating my curiosity. I've learned a lot under his supervision and also thanks to his passion and creativity, the learning has never been boring.

I would also like to thank Gael De Oliveira, for his help with Optiflow, and prof. Bierbooms for suggesting useful papers I used in the thesis.

Contents

List of Tables

List of Figures

ABBREVIATIONS

ABL = Atmospheric Boundary Layer;
AEP = Annual Energy Production;
AoA = Angle of Attack;

BEM = Blade Element Momentum theory;
BL = Boundary Layer;

C = Combined Values Case (sec: 3.3);
CF = Cost Function;
CV = Control Volume;
cdf = Cumulative Distribution Function;
CST = Class function Shape function Transformation technique;

DOFs = Degrees of Freedom;

FAST = Fatigue, Aerodynamics, Structural and Turbulence code;

H = High Values Case (sec: 3.3);
HAWT = Horizontal Axis Wind Turbine;
HSS = High Speed Shaft;

IEC = International Electrotechnical Commission;

L = Low Value Case (sec: 3.3);
LE = Leading Edge;

MF = Mingle Factor;
MOST = Monin-Obunkhov Similarity Theory;

NSGA = Non-dominated Sorting Genetic Algorithm;

pdf = Probability Density Function;

TE = Trailing Edge;
TI = Turbulence Intensity;
TSR = Tip Speed Ratio;

WS = Wind Shear;

YM = Yaw Misalignment;

LIST OF SYMBOLS

a = Axial Induction Factor [-];
a = scale parameter (Weibull) [-];
$\overline{a}$ = Azimuthally and Radially averaged induction factor [-];
$\hat{a_G}$ = distribution parameter for the conditional probability of turbulence intensity given the wind speed [-];
A = Amplitude of a wave function;
A (or B) = Generic Event (in probability);
α (or AoA) = Angle of Attack [°];
α = exponent of the wind shear power law [-];
α_i = spacial growth rate of the T-S wave;
A_c = Charnock's constant;
A_r = Rotor Area [m^2];

b = term to scale the standard deviation of the wind speed [$\frac{m}{s}$];
B = Number of Blades [-];
β = Yaw Misalignment Angle [°];
β = Coefficient for wind shear in stable atmospheric conditions [-];
β = Boat-tail angle [°];

c = Chord [m];
C = Class Function;
C_t = Thrust Coefficient [-];
C_D = Drag Coefficient [-];
C_L = Lift Coefficient [-];
C_n = Normal Force Coefficient [-];
C_t = Tangential Force Coefficient [-];

D = Drag Force [N];
δ = Relative Perturbation induced by atmospheric turbulence [-];
δ^* = Displacement Thickness [m];

E = Young's Modulus [$\frac{N}{m^2}$];
ϵ = Strain [-];

f (or h, g) = Generic Function;
F = Force [N];
F = Prandtl's Tip Loss Factor [-];
F = Class of Events;
φ = Phase of a wave function;
ϕ = Inflow Angle [°];
Φ_m = Analytic function for wind shear;

γ_1 = Coefficient for wind shear in unstable atmospheric conditions [-];

h = Height [m];
H = Shape Factor [-];

I = Turbulence Intensity [-];

J = Jacobian;
k = Reduced Frequency [Hz];
k = von Karman Constant [-];
k = shape parameter (Weibull) [-];
K = coefficient in Glauert correction;
K = Correction Coefficient for the azimuthally and radially averaged induction factor [-];
χ = Skew Wake Angle [°];
$K_{r,n}$ = Binomial Coefficient for Bernstein polynomials [-];

L = Lift Force [N];
L = Monin-Obukhov Length [m];
λ = Tip Speed Ratio [-];

MF = Mingle Factor [-];
Ma = Mach Number [-];
μ = mean value;

n = maximum amplification ratio of the T-S wave;

ω = frequency [Hz];
Ω = Angular Velocity [$\frac{rad}{s}$];

pf = penalization factor [-];
p (or P) = probability [-];
ψ = Azimuth Angle [°];
Ψ_m = Analytic function for wind shear;

Q = Torque [Nm];

Re = Reynold's Number [-];
Re_Θ = Reynold's number based on momentum thickness [-];
$Re_{\Theta,0}$ = Reynold's number at the instability point [-];
r = Radial Position [m];
R = Rotor Radius [m];

ρ = Air Density [$\frac{kg}{m^3}$];

S = Shape Function;
S = Sample Space;
σ = stress [$\frac{N}{m^2}$];
σ = Standard deviation;
σ^2 = Variance;

t = time [s];
t = thickness [m];
T = Thrust Force [N];
τ = Time Constant [s];
θ = Structural Pitch Angle [°];
θ_p = Section Pitch Angle [°];
Θ = Momentum thickness [m];

u = wind speed within the boundary layer [$\frac{m}{s}$]; U = Wind speed outside the boundary layer [$\frac{m}{s}$]; $\widetilde{u}$ = Deviation from the mean wind speed [$\frac{m}{s}$];
u_i = Induced axial velocity [$\frac{m}{s}$];
u_* = friction velocity [$\frac{m}{s}$];
U_∞ = Far upstream axial wind speed [$\frac{m}{s}$];

V_{rel} = Relative wind speed seen by the airfoil [$\frac{m}{s}$];

w_{case} = Weighting Coefficient for each case [-];

z_0 = Surface Roughness [m];
ζ = Atmospheric Stability Parameter [-];

$|$ = 'given' in conditional probability definition;
$\cap$ = Intersection;
$\perp$ = normal (or perpendicular);
$\|$ = parallel;

Chapter 1

Introduction

The increasing trend of greenhouse gases emissions is one of the most actual and challenging issue the world has to tackle. Predictions done by OECD estimates that at the current emission rate, the temperature increase in 2100 will range between 3.7 and 5.6 °, with respect of the pre-industrial period, while today, the temperature increase with respect of the pre-industrial ages is about 1 ° [1]. It has been proven that the main reason for the increase in temperature is due to the increase in the greenhouse gases concentration in the atmosphere, among which, the carbon dioxide has the largest share. In particular, projection predicts a 50% increase in the global greenhouse gases and the main cause is found in a 70% growth in CO_2 emissions related to energy use [1].

In this framework, renewable energies seem to be the most promising solution. The main advantage of renewables, of course, is the carbon dioxide-free production of energy. With the technological development, these technologies are becoming cheaper and consequently cost competitive with the carbon-based technology, having also promising room for further improvements. Among the several renewables, this work will deal with wind energy, in particular, addressing the most spread wind energy technology, namely wind turbine with an horizontal axis. Wind turbine technology is continuously improving; the current trend shows how the size of wind turbines is increasing [55] and the larger the wind turbine the more challenging its design will be. Moreover, the offshore technology, is making big steps as well, so that the offshore limits, in terms of distance from the land, are being progressively overcome. This would in first instance increase the maximum available wind speed, but also the space in which a wind turbine could be placed increases consistently. Several works in the literature mention an average lifetime of a wind turbine to be around 20 years, but, nowadays, efforts are starting to be put in trying to increase the wind turbine lifetime; in this perspective, fatigue becomes crucial. Fatigue refers to the possibility of failure due to cyclic loads. The loads to which a wind turbine is subject to are dependent on the angle of attack seen by the rotor blades and consequently a cyclic variation of the angle of attack over a revolution will lead to load variation over a revolution and increasing fatigue damage. Being able to provide an estimation for how the load will change over a revolution might lead to a more robust design for wind turbines.

As for the power production plants, the final goal of wind turbine is to yield the largest possible amount of energy. The amount of energy that can be extracted from a wind turbine strongly depends on the wind conditions. The issue is that the wind conditions change continuously and they are extremely hard to predict in advance. This holds true because several non-homogeneous perturbation effects affect the wind speed magnitude and in particular, the relative wind speed will be different at different azimuthal positions [32]. This means that the angle of attack will vary over a generic revolution. The angle of attack of an airfoil is strictly related to the Lift produced by the airfoil, which is the force that allows the energy production. Generally speaking, airfoils are designed according to a specific value of angle of attack, often referred to as design angle of attack, and they are optimized accordingly. The problem is that, as discussed before, a specific airfoil will never constantly operate at the design angle of attack; this means that the aerodynamic airfoil performance will never be constantly optimal. This work follows the probabilistic design approach presented in [32], which attempts to estimate how much is the angle of attack likely to fluctuate over a revolution, in order to design airfoils whose performance will be optimized for the estimated range of angle of attack experienced by the airfoil over a revolution and not according to the design value. The term 'probabilistic' refers to the impossibility of predicting turbulence intensity in a deterministic way. For this reason, the need for a probabilistic approach arises in this work.

At the end of the project, the thesis objectives that the author is willing to achieve are listed below:

- To understand how different perturbation sources and different combination of perturbation sources affect the angle of attack and understanding how the different perturbation sources have been modelled;
- To verify the proposed model and method by using the aero-elastic simulation software (FAST);
- To determine which environmental conditions are relevant for the estimation of the angle of attack range over which the aerodynamic performance will be optimized and estimate their probability of occurrence;
- To design airfoils with the probabilistic approach by employing a genetic multi-objective optimization software (OptiFlow);

Finally, a road map is presented to discuss the layout of the thesis, as shown in Figure 1.1, where the content of each chapter is sketched. Chapter 2 will provide the theoretical background necessary for the understanding of the aerodynamics of an airfoil and of and horizontal axis wind turbine; a brief analysis of the unsteady effects as well as a summary of the main wind energy airfoil requirements will also be discussed. Chapter 3 will introduce the concept of probability starting from the simple example of a dice rolling. Subsequently, the formulation of the probabilistic model will be presented and a preliminary model analysis carried out. At the end of the chapter, a probabilistic design space mapping will be performed. The main aim of this section is to determine which wind conditions are relevant for airfoil designing purposes, how much they influence the angle of attack fluctuations and how much they are likely to occur in practice. In order to evaluate the accuracy of the model prediction, a verification must be done and it will be performed by employing an aero-elastic simulation tool, namely FAST. Chapter 5 will describe the genetic multi-objective optimization tool (Optiflow) which has been used to design and optimize airfoils. Chapter 6 will present and discuss the results of the optimization and finally, in chapter 7, the main conclusion will be drawn.

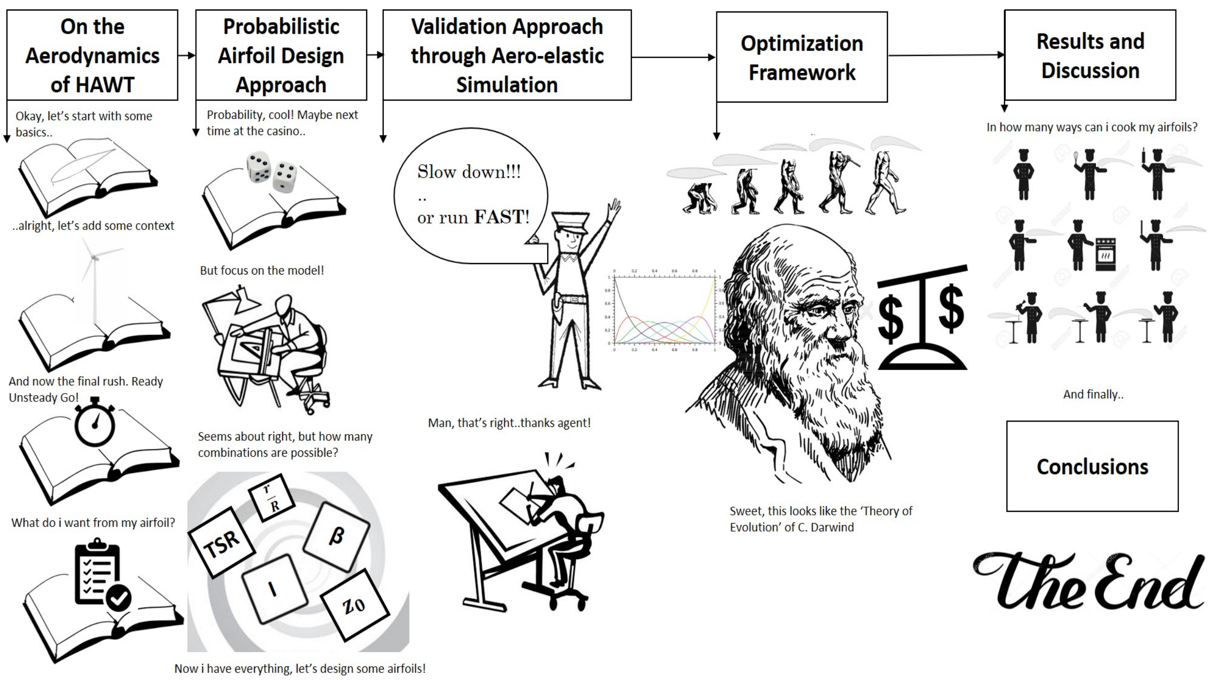

Figure 1.1: *Graphic description of the thesis layout*

Chapter 2

Aerodynamics of Horizontal Axis Wind Turbine

The term 'aerodynamics' refers to the study of the air movement and of the interaction of an air flow with a solid object flowing through it. The present work focuses on probabilistic airfoil design for Horizontal Axis Wind Turbine (HAWT), and therefore, this chapter will discuss what are the main aerodynamic phenomena which occur when a wind turbine is operating. In particular, the aerodynamics of a wind turbine can be sub-divided in two main categories: section 2.1, where the analysis is focused on the airfoil length-scale, and section 2.2 where the interaction of the wind flow with the whole wind turbine system is evaluated. Insights about the unsteady phenomena related with wind turbine will be provided in section section 2.3 and finally, in section 2.4, the main aerodynamic requirements needed to optimize the aerodynamic performance of an airfoil will be presented.

2.1 Airfoil Aerodynamics

The geometry of a wind turbine blade is characterized by a span-wise length considerably larger than its chord (large aspect ratio) and it has been observed that the tangential component of the wind velocity is much smaller than the velocity component in the stream-wise direction. This argument justifies the assumption of two dimensional flow at a given blade cross section, meaning that the wind speed over the blade span is assumed to be zero [3]. In order to realize such an ideal system, the wind turbine blade is assumed to be of infinite span; this assumption is useful to simplify the problem, as it allows to neglect three-dimensional effects.

2.1.1 Airfoil Definitions

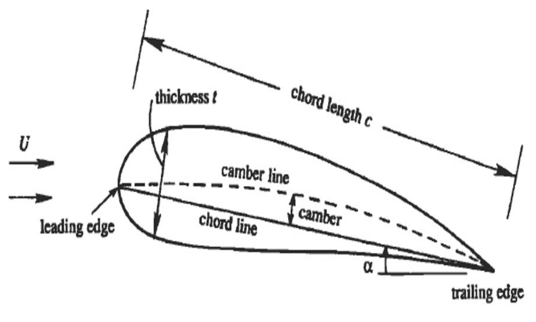

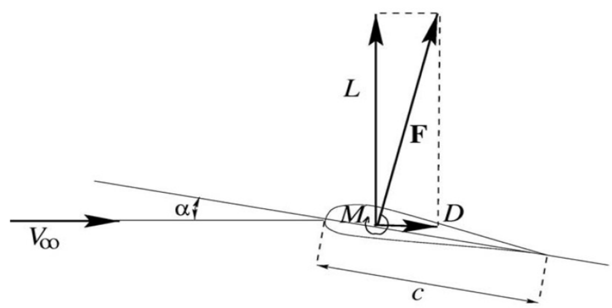

Figure 2.1: *(a) Typical airfoil geometry and (b) forces acting on an airfoil [3]*

This section describes a generic airfoil geometry shape, providing basic definitions. An airfoil can be defined as the cross section of a generic wing. The typical airfoil shape is illustrated in Figure 2.1a. The leading edge (LE) is the part of the airfoil profile which directly experiences the airflow; the LE nose shape is a relevant parameter for the transition and stall characteristics of the airfoil. The trailing edge (TE) is the rear edge of the airfoil; in potential flow, the trailing edge is subject to the Kutta condition, which states that the TE has to be a stagnation point, or otherwise, the flow must leave the TE in a smooth way [6]. Moreover, due to manufacturing feasibility, a minimum TE thickness of 0.25% of the chord is required [42]. The chord (c) of the airfoil is defined as the straight line connecting the leading edge with the trailing edge. The camber line is described as the line that is equally spaced between the upper and the lower surface of the airfoil, while, the camber of a generic airfoil expresses the maximum height that the camber line reaches above the chord line. The thickness is defined as the distance between the upper and the lower surface of the airfoil [2]. The location of the maximum thickness is an important parameter as well when it comes to airfoil design.

2.1.2 Aerodynamic Forces acting on an Airfoil

The aerodynamic forces acting on an airfoil as well as the resulting polar curves will be discussed in this section. Figure 2.1b shows the forces an airfoil is subjected to. The aerodynamic force F exerted by the inflow on the airfoil can be decomposed into two forces, namely: Lift and Drag. Therefore, Lift and Drag can be respectively defined as the force component perpendicular and parallel to the flow direction. When an incoming flow approaches an airfoil, the upper and lower surface of the airfoil act in such a way to cause a flow acceleration on the suction side, which leads to a higher velocity field with respect of the one experienced by the lower surface. The larger velocity field across the suction side generates a low pressure region while the lower surface of the airfoil experiences a high pressure region. This pressure difference will therefore generate a Lift force that pushes up the airfoil. Indeed, Lift is calculated by integrating the pressure distribution over the airfoil surface [3]. The pressure distribution across the whole airfoil surface is directly related to the angle of attack, defined as the angle α (or AoA) between the chord line and the relative wind speed direction. This means that by varying the AoA, the pressure distribution across the airfoil will change and the aerodynamic force will be affected by this change. It is common practice to refer to Lift and Drag in terms of the Lift and Drag coefficients, which can be expressed as [3]:

$$C_l = \frac{L}{\frac{1}{2}\rho V_\infty^2 c} \tag{2.1.1}$$

$$C_d = \frac{D}{\frac{1}{2}\rho V_\infty^2 c} \tag{2.1.2}$$

Where, in this definition, L and D are the the Lift and Drag force per unit of length $\left[\frac{N}{m}\right]$, ρ is the air density, c is the chord and V_∞ is the undisturbed upstream wind speed seen by the airfoil. Sometimes, Lift and Drag are used as a measure of the aerodynamic efficiency, as:

$$\eta_{aerodynamic} = \frac{L}{D} = \frac{C_l}{C_d} \tag{2.1.3}$$

This expression can be easily explained by pointing out that Lift is the useful effect which allows to overcome gravity while Drag is a force which acts as a resistance for the incoming flow, mostly due to pressure (Form Drag) or to skin friction (Skin Friction Drag). Maximizing this quantity would therefore allow to reach the highest possible Lift while keeping the Drag as low as possible.

Generally speaking, by looking at the Lift polar (depicted in Figure 2.2b) , three regions can be identified [3]. A region where the Lift coefficient increases linearly with the AoA, a region where C_l still increases along with the AoA but with a non-linear dependency and a post-stall region. The post-stall region begins after the stall AoA (defined as the angle of attack where $\frac{dC_l}{dAoA} = 0$) is reached. In stall conditions, the flow separation point shifts towards the LE of the airfoil leading to an earlier separation of the boundary layer, with respect of the separation point that would result from an AoA $< AoA_{stall}$, which provokes Lift losses. The Drag polar shows how the Drag coefficient increases roughly with a quadratic dependence of the AoA. This means that for low values of AoA the Drag coefficient is close to 0; when the AoA increases, the Drag coefficients will rise faster than the Lift coefficient. This means that when the C_l reaches its maximum, the C_d will be large enough to make the ratio $\frac{C_l}{C_d}$ to be non maximum. In particular, when an airfoil stalls the contribution of Form Drag becomes too large, resulting in a significant decrease in aerodynamic efficiency. This also means that a possible way through witch stall can be prevented is by reducing Drag [3].

Aerodynamic efficiency is one of the most important requirements for a wind energy airfoil and it would be ideal if the airfoil could always operate at the point of maximum efficiency. In order to

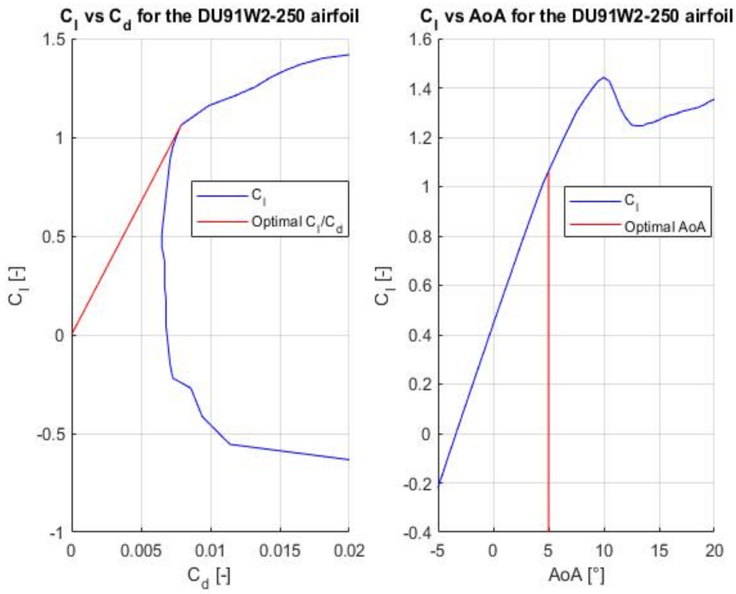

Figure 2.2: *(a) Lift coefficient as a function of the Drag coefficient and (b) Lift coefficient vs. Angle of attack for the DU97W2-250 airfoil*

evaluate what is the point of maximum efficiency, the Lift coefficient can be plotted as a function of the Drag coefficient, as can be seen in Figure 2.2a. This allows to see what is the angle of attack which maximizes the $\frac{C_l}{C_d}$ ratio, which is referred to as design (or optimal) angle of attack [3]. The optimal angle of attack can be found as the angle at which $\frac{d\frac{C_l}{C_d}}{d\alpha} = 0$.

2.1.3 Viscous Effects

This section will introduce the concept of boundary layer (BL) as well as the integral BL parameters and it will relate them to the concept of flow separation.

When studying the interaction between a fluid and an object, if the analysis is carried out away from the wall of the object, the fluid can be considered to be inviscid [2]. However, in real flow analysis, viscous effects are crucial and in particular the boundary layer is of importance because it allows to account for the role that viscosity plays in proximity of an object. When a fluid flows over a layer, the dominant effect of the viscous force will make the flow velocity to be zero at the wall (also known as non-slip condition). This holds up to the point where the flow is far enough from the layer that the effect of viscosity becomes negligible. The boundary layer is, therefore, the region that divides the zone in which a flow is assumed to be inviscid and the region where the flow is considered to be viscid. In general terms, the thickness of the boundary layer is a function of the Reynold's number (Re) and the surface roughness; in particular, the lower the Re the larger the thickness of the boundary layer will be, which means the larger the region where the viscous effects dominate, while if Re is large, the thickness of the boundary layer becomes considerably smaller than the characteristic length of the object. Moreover, the larger the surface roughness the larger the boundary layer thickness will be [5].

The boundary layer is usually studied according to its integral parameters, namely displacement and momentum thickness. Displacement (δ^*) and momentum (Θ) thickness are respectively related to the changes in mass flow-rate and momentum flux of a fluid flowing over an object due to the effect of viscosity. In particular, the key idea is to represent a viscid flow by modifying the thickness of object's surface rather than the velocity distribution of the flow itself. If the flow is assumed to be inviscid, its velocity magnitude will be larger than for a viscid flow in the BL. In order for a viscid and an inviscid flow to have the same mass flowrate, the thickness of the object across which the inviscid flow is flowing should be slightly larger than for a viscid flow. The displacement thickness can be therefore defined as the amount of additional thickness that an object should have in order for the inviscid mass-flow rate and the viscid mass flowrate to be equivalent. Similarly to the displacement thickness definition, the momentum thickness indicates how much the thickness of an object should grow for the momentum flux of a viscid and an inviscid flow to be the same. The displacement and momentum thickness can be defined as [5]:

$$\delta^*(x) = \int_0^\infty \left(1 - \frac{u}{U}\right) dy \tag{2.1.4}$$

$$\Theta(x) = \int_0^\infty \frac{u}{U} \left(1 - \frac{u}{U}\right) dy \tag{2.1.5}$$

Where the reference system is X aligned with the stream-wise direction and Y which represents the distance normal to the airfoil surface and u and U are the velocity magnitude within and outside the BL, respectively. Following these definitions, the shape factor (H) can be introduced as [5]:

$$H(x) = \frac{\delta^*}{\Theta} \tag{2.1.6}$$

The shape factor can be therefore seen as the ratio between the change in the mass flowrate and the variation in the momentum flux between the fictitious inviscid flow and the real viscid flow, due to effect of viscosity.

Something that it is closely related to the boundary layer is flow separation. Flow separation can be classified according to the chord-wise position at which the flow starts separating; two types of separation are possible [3]:

- Trailing Edge separation: it starts at the trailing edge and it slowly shifts towards the Leading Edge along with the increase of the AOA. In this case, a soft stall is expected. Due to the flow acceleration on the upper surface of the airfoil, a minimum pressure point can be found; this can be thought of in terms of the Bernoulli's principle, where an increase in the flow velocity results in a decrease of the pressure. Consequently, moving from the minimum pressure point towards the TE, pressure will necessarily increase. This means that the flow flowing over the airfoil surface will always experience an adverse pressure gradient. If the adverse pressure gradient becomes too large, the flow will not have enough energy to go through and separation occurs. The velocity profile in adverse pressure gradient is s-shaped [3], this means, that as long as the flow is not reversed, separation can be prevented.
- Leading Edge separation: it starts at the leading edge. This separation needs way more attention than the previous, because it may lead to an almost immediate separation of the entire boundary layer. This would imply a significant and immediate Lift loss. For this reason, the shape of the LE is crucial in order to avoid leading edge separation [3].

In order to evaluate when the BL is expected to separate, the shape factor is generally used, and in particular, for a turbulent flow separation is expected to occur for $2 < H(x) < 3$ [3], while for a laminar flow, BL separation is expected to take place whether H(x) > 3.5 [11].

2.1.4 Flow Regimes

This section will initially discuss the different flow regimes in which a flow can operate, namely laminar and turbulent to consequently analyze their relationship with the so called 'clean' and 'rough' performance of the airfoil. Indeed, both laminar and turbulent flow are important when considering airfoil applications; the conditions of the surface of the airfoil are important for the flow transition and broadly speaking, the larger the surface roughness of the airfoil the larger the portion of the airfoil which experiences a turbulent flow will be, because of an earlier transition. When talking about wind turbine airfoils, the airfoil roughness will increase over time due to the contamination of dust, insects, other impurities and erosion on the airfoil surface. Consequently, in the first period of the airfoil life, the performance of the airfoils can be associated to a clean configuration, while, over time, the aerodynamic performance gradually shifts towards the rough configuration.

In order to differentiate among the two different flow regimes, the typical values of some characteristic properties such as Reynold's number, wall shear stress and streamlines shape will be used to describe each regime. The laminar regime can be described by a low Re, low wall shear stress and by roughly parallel stream lines (laminar velocity vector can be approximated as if it has only one component in the stream-wise direction). Conversely, the turbulent regime is characterized by high Re, high wall shear stress and non parallel streamlines (turbulent velocity vector will have three components $\overrightarrow{V} = u\widehat{i} + v\widehat{j} + w\widehat{k}$) [5]. The transitional 'regime' is considered to be in between the above mentioned regimes, meaning that it cannot be defined neither laminar nor turbulent.

The laminar wall shear stress can be expressed as $\tau_l = \mu \frac{dU}{dy}$ [5]; from this definition, it can be seen that the wall shear stress is proportional to the vertical velocity gradient and to the dynamic viscosity. The turbulent wall shear can be defined as $\tau_t = \tau_l - \rho \overline{uv}$, where the term $-\rho\overline{uv}$ is referred to as Reynolds stress [5]. As deeply discussed in [2], the Reynolds stress allows to account for the rate of momentum which is transferred from the fluctuation component of the velocity ($\widetilde{u}$) to the mean velocity component of the flow ($\overline{U}$). In particular, when a turbulent flow streams over an airfoil, the mixing will act in such a way to transfer energy from outside the boundary layer into the boundary layer region, increasing its velocity magnitude. This means that the kinetic energy of the fluid in the BL will be larger than for a laminar flow; this larger amount of kinetic energy will make the flow to be more resistant to withstand the adverse pressure gradient, leading to a later separation of the boundary layer. On the other hand, a laminar flow is usually associated to a lower Drag than for a turbulent flow. The reason for this can be attributed to the value of the skin friction at the wall in laminar or turbulent flow. If the velocity magnitude in the boundary layer increases, when a turbulent flow is considered, the vertical velocity gradient ($\frac{\partial U}{\partial y}$) will be larger and consequently the wall shear stress will be larger as well leading to higher values of Drag than for a laminar flow.

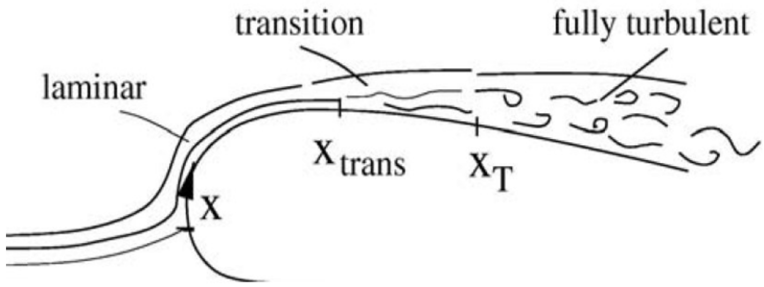

Figure 2.3: Scheme of the transition process over an airfoil [3]

Figure 2.3, which schematizes the transition process across an airfoil, is helpful to discuss the relationship between the Reynold's number and the different regimes. The Reynold's number is defined to be proportional to the characteristic length of the airfoil, namely the chord fraction. Close to the leading edge, the distance over which the BL is developing will be low, resulting in a low Re, and consequently the flow can be considered to be laminar. While advancing, the distance covered by the fluid becomes larger and larger, making the Re number to increase. Finally, when the flow start approaching the TE region, the distance covered by the flow will be close the chord value, which would make the Re to be high; this is associated to the turbulent regime. The point at which transition occurs (x_{trans}), is strongly dependent on the surface roughness of the LE, which, in wind energy foils, arises from contamination and erosion, as mentioned before. In order to evaluate the impact of the roughness on the airfoil performance, two different configurations can be studied, namely *clean* and *rough*. The clean configuration assumes a free transition of the boundary layer, which is the most common way through which a fluid can transit from laminar to turbulent regime in airfoil applications. This transition is dominated by the Tollmien-Schlichting wave (T-S wave), which can be defined as 'the most unstable eigen-mode of Orr-Sommerfeld equation' according to [12]. Conversely, the rough configuration is evaluated by forcing transition at a specific chord-wise position [30]. From the experimental point of view, the rough configuration can be obtained by placing a zigzag tape either on one or on both sides of the airfoils. The increased roughness obtained through the zigzag tape increases the momentum thickness Θ, making the shape factor (H) to decrease [30].

A comparison between the lift polar curves in clean (left-hand figure) and rough (right-hand figure) configurations is shown in Figure 2.4, which represents three different airfoils with a 30% relative thickness for different Reynold's numbers. From the comparison, it is quite clear that a premature turbulent transition would strongly affect the Lift coefficient, which results in much lower values than in the clean configuration. Given the large effects on the C_l, the roughness sensitivity analysis cannot be neglected and it must be taken into account when designing airfoils. No references could be found in the literature about what is the percentage of time, with respect of the airfoil lifetime, in which the airfoil's surface conditions can be associated to a clean or rough configuration.

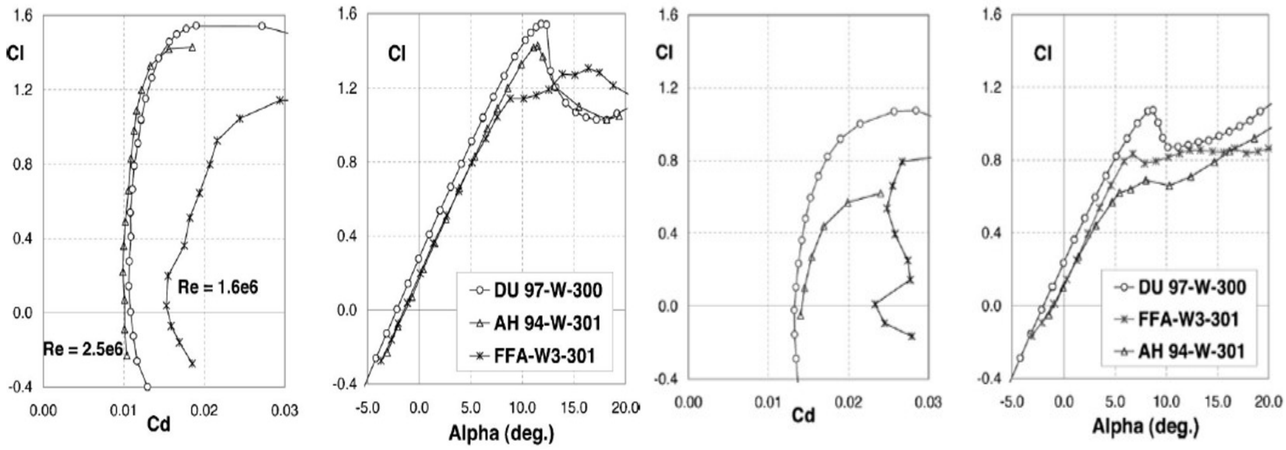

Figure 2.4: *Comparison of the C_l vs C_d and C_l vs. AoA curves between 'clean' (left) and 'rough' (right) configuration, for 30 % thick airfoils with different Reynolds number, namely Re = 2.0 $\times 10^6$ (DU), Re = 1.6 $\times 10^6$ (FFA) and Re = 1.5 $\times 10^6$ (AH).*

The present work focuses on airfoil design, which will be later performed by using the RFOIL program; RFOIL predicts transition by using the e^n method and consequently only this method will be presented in this section. The e^n method lies on the assumption that transition occurs when the most unstable T-S wave in the BL has grown by a factor e^n [9] [11]. Where n is the maximum amplification ratio defined as [10]:

$$n = max\ \tilde{n}(x;\omega) = -\int_{x_0}^{x} \alpha_i(\omega)\, dx \tag{2.1.7}$$

Where ω is the frequency, $x_0(\omega)$ indicates the location of the instability point, $-\alpha_i$ is the spacial growth rate of the T-S wave and n(x; ..) expresses the amplitude growth of the disturbance along the surface. As discussed in [11], by using the Falkner-Skan profile family to solve the Orr-Sommerfeld equation, it is possible to compute the amplification factor. In particular, the logarithmic of the maximum amplification ratio n can be obtained by integrating the local amplification rate between the critical Reynold's number (at the instability point) and the Reynold's number at maximum momentum thickness. The expression for the maximum amplification ratio would therefore be [11]:

$$n = \int_{Re_{\theta,0}}^{Re_\theta} \frac{dn}{dRe_\theta}\, dRe_\theta \tag{2.1.8}$$

Where $Re_\theta = \frac{U(x)\Theta(x)}{\nu}$ [3] is the Reynold's number based on momentum thickness, while $Re_{\theta,0}$ is the critical Reynold's number. Besides, the expressions for $(\frac{dn}{dRe_\theta})$ and $Re_{\theta,0}$ are showed below [11]:

$$\frac{dn}{dRe_\theta} = 0.01[(2.4H - 3.7 + 2.5tanh(1.5H - 4.65))^2 + 0.25]^{0.5} \tag{2.1.9}$$

$$log_{10}(Re_{\theta,0}) = \left(\frac{1.415}{H-1} - 0.489\right) tanh\left(\frac{20}{H-1} - 12.9\right) + \frac{3.295}{H-1} + 0.44 \tag{2.1.10}$$

It should be pointed out that these relationships have been derived as if they are only dependent on the shape factor, neglecting the influence of the momentum thickness [11], which would change Re_Θ. Although this is a reasonable assumption, because for small values of $\frac{u}{U}$ the shape factor decreases much faster than the increase in momentum thickness, while for values of $\frac{u}{U}$ close to 0.5, where the momentum thickness is around maximum, the variation of the momentum thickness along with the acceleration of the flow within the BL will be very small.

2.2 HAWT Aerodynamics

This section considers the aerodynamic phenomena relevant at the rotor-scale. It must be pointed-out that when considering the whole wind turbine system 3-Dimensional effects play a relevant role and the 2-D aerodynamics is not able to accurately compute the aerodynamic performance of the blade section. Indeed, in a rotating blade, the separation which occurs after stall depends on the Coriolis and the Centrifugal force, which are not accounted for in the 2-D aerodynamics [58]. At large AoAs, when the BL massively separates, the Coriolis force pushes the flow towards the trailing edge of the airfoil, which can be seen as a favourable pressure gradient locally applied on the flow. Moreover, the Coriolis force also acts in order to extract mass from the separation bubble region, which is then re-directed in the span-wise direction by the effect of the Centrifugal force. This implies a reduction in the volume of the separation bubble, because part of the flow has been shifted towards the blade tip. The consequence is that the separation bubble region will experience a pressure drop, which will increase the blade loading. The 2-D post stall characteristics of the airfoil are not able to describe this process [23].

2.2.1 Blade Element Momentum (BEM) Theory

This section explores and discuss the Blade Element Momentum Theory (BEM), which is the main model used to study the aerodynamics of a horizontal axis wind turbine. BEM is a model which couples the Blade Element theory with the Momentum theory allowing to derive the relevant equations that regulate the aerodynamics of a HAWT. The Blade Element theory divides the blade into a number of elements, over which, the normal component of the force (dF_N) is exerted. At each span-wise location, the normal component of the force is assumed to be the same for all the blades. The Momentum theory assumes that the Thrust force is uniformly distributed over a thin actuator disk. The Blade Element Momentum theory states that, considering a blade element (dr) and a thin annular disk with the same thickness (dr), the sum of the normal component of the force on the blades must be the same of the thrust on the annular disk, under the following assumptions [3]:

- Each annular element has no radial dependency, meaning that each annular disk cannot influence the others. There is no radial flow across the blades;
- The force that the blades exert on the flow is constant over an annular disk, which also means that the annular disk is infinitesimal and the rotor has infinite number of blades;
- 3-D effects are neglected, only 2-D aerodynamics is considered;

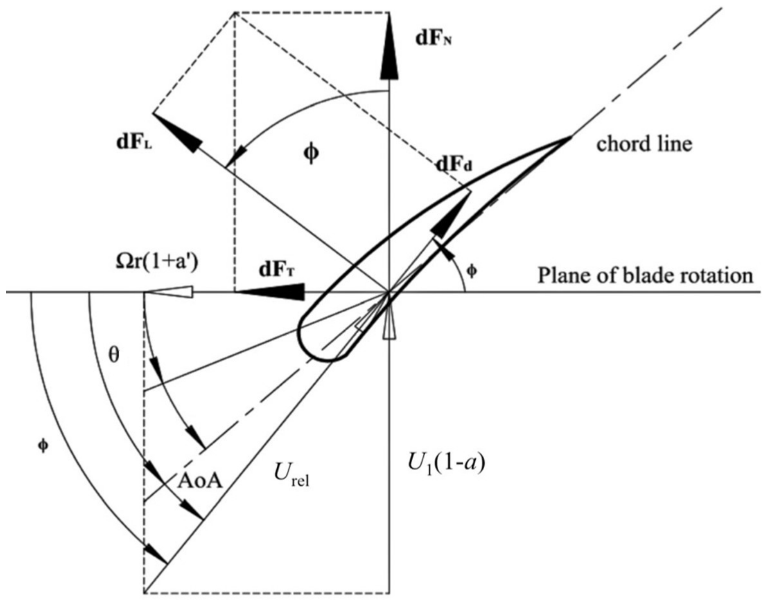

Figure 2.5: *Blade Element Momentum Theory - Inflow Geometry [3]*

By looking at Figure 2.5 some parameters and correlations need to be defined. $\phi = \theta + AoA$ is the Inflow Angle, which is the angle that allows to relate the relative velocity seen by the airfoil with its components, namely rotational speed and axial wind speed. θ is the section pitch angle, which is given by the sum of the blade pitch angle at the tip and the structural pitch angle. The structural pitch angle is related with the geometry of the blade and with the twisting of the blade. Twisting the blade is important in order to have a constant AoA over the blade span. By looking at the velocity triangles of two blade sections, near the root and close to the tip, it can be observed that, due to the difference in the rotational component of the relative wind speed, the only way in which the same AoA can be achieved is by reducing the structural pitch angle moving from the root towards the tip of the blade. It is also worth noticing that the rotational and the axial wind speed components of the relative velocity have been corrected by the terms a and a'; The first term is referred to as axial induction factor and it is used to account for the reduction of the wind speed, between far upstream the rotor and the rotor level, stressing that the wind turbine itself constitutes an obstacle for the upcoming wind, influencing its velocity magnitude. The angular induction factor is introduced to include in the analysis the effect of the rotation of the blades on the relative velocity seen by the airfoil between close upstream and downstream the rotor (e.g. wake); indeed, the turning of the blade induces a rotation in the air surrounding the rotor, in the opposite direction of the one of the blades. Consequently, the relative velocity in the near wake of the rotor is given by an axial component which is unchanged with respect of upstream the rotor, and by an additional component in the tangential direction, with an opposite sign with respect of the rotational speed of the rotor. This additional component is represented by the term a' [3].

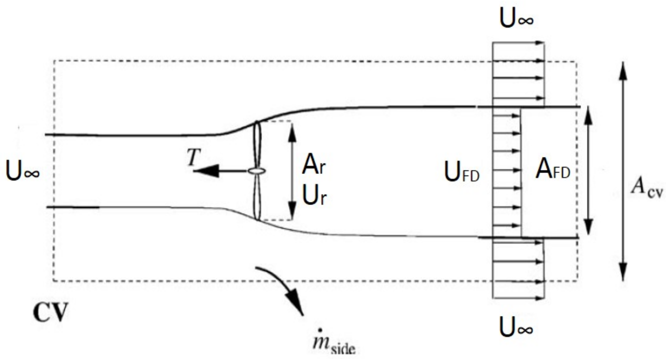

Figure 2.6: *Circular control volume (CV) around a wind turbine [3]*

The 1-D Momentum theory assumes stationary, incompressible and frictionless flow, as well as no external force acting on the fluid. Under this assumptions the Bernoulli equation is valid. This equation is used in combination with the conservation of mass and the axial momentum conservation in the integral form, which, under the assumption of ideal rotor, allows to derive important correlations between the wind velocity magnitude at different sections in the stream wise direction, namely: far upstream (subscript ∞), rotor (subscript R) and far downstream (subscript FD), as illustrated in Figure 2.6. This figure also shows the wake expansion of the streamlines due to the presence of the rotor disk and due to the thrust force exerted by the wind turbine blades on the wind. The thrust force can be defined as the force that results from the pressure drop (between close upstream and close downstream) across the rotor, resulting in $T = \Delta p\ A_R$. The pressure drop can be found by applying the Bernoulli equation over a streamline between far upstream and far downstream the rotor, leading to the following expression [3]:

$$T = \frac{1}{2}\rho A_R(U_\infty^2 - U_{FD}^2) \tag{2.2.1}$$

By applying the axial conservation in the integral form and the conservation of mass, it is possible to define the wind velocity magnitude at the rotor level as the average between the velocity magnitude far upstream and far downstream the rotor as follows:

$$U_R = \frac{1}{2}(U_\infty + U_{FD}) \tag{2.2.2}$$

By introducing the induction factor a as the relative difference between the wind speed far upstream the rotor and the wind speed at the rotor level:

$$a = \frac{U_\infty - U_R}{U_\infty} \tag{2.2.3}$$

It follows that:

$$U_R = U_\infty(1-a) \tag{2.2.4}$$

This relationship is very important because it allows to relate the undisturbed wind speed far upstream the rotor to the wind speed at the rotor level. In order to do so, the induction factor needs to be determined. As discussed in [3], the induction factor can be estimated starting from the power coefficient, by the relationship:

$$c_p = 4a(1-a)^2 \tag{2.2.5}$$

By recalling the definition of the power coefficient $c_p = \frac{P}{\frac{1}{2}\rho U^3 A_r}$, it can be seen that the induction factor is a function of the rotor area, which, under the assumption of the rotor being an actuator disk, can be calculated as πR^2. Although, this assumption leads to an underestimation of the induction factor, because the real rotor area, being a rotor usually 3-bladed, will be lower that the one estimated assuming an actuator disk. If the area is smaller, the power coefficient will be larger leading to a larger induction factor. Moreover, it can also be seen that the induction factor is a function of the aerodynamic power and of the wind speed cubed. This means, that the induction factor will change according to the considered tip speed ratio. For below rated wind speeds, where the tip speed ratio is kept constant, the aerodynamic power will increase with the cube of the wind speed and consequently the power coefficient will be constant as well as the induction factor. For above rated wind speeds, the aerodynamic power is kept constant while the wind speed keeps increasing, leading to a progressive decrease in the induction factor.

The Blade Element theory provides important expressions for the forces acting on an airfoil. Recalling that Lift is always perpendicular to the relative wind speed as well as Drag is always parallel to it, it is possible to correlate the inflow angle with the relative wind speed as [3]:

$$tan(\phi) = \frac{U_\infty\ (1-a)}{\Omega\ r\ (1+a')} = \frac{1-a}{\lambda_r\ (1+a')}; \qquad V_{rel} = \frac{U_\infty\ (1-a)}{sin(\phi)} \tag{2.2.6}$$

It is worth noticing that, this equation would lead to the determination of the angle attack by using the following relationship: $AoA = \phi - \theta$. Moreover, the expressions for the Lift and Drag forces can be written as [3]:

$$dL = \frac{1}{2}\ C_l\ \rho V_{rel}^2\ c\ dr; \quad dD = \frac{1}{2}\ C_d\ \rho V_{rel}^2\ c\ dr \tag{2.2.7}$$

Lift and Drag are the forces acting on the airfoil reference system, meaning that they are perpendicular and parallel to the AoA. In order to express these forces in the rotor plane reference system (perpendicular and parallel to the rotor plane) the inflow angle can be used. Indeed, the normal (subscript N) and tangential (subscript T) forces acting on the rotor plane can be seen as a combination of Lift and Drag, leading to [3]:

$$dF_N = dL\ cos(\phi) + dD\ sin(\phi) \rightarrow dF_N = B\frac{1}{2}\ \rho\ V_{rel}^2\ c\ dr\ (C_l\ cos(\phi) + C_d\ sin(\phi)) \tag{2.2.8}$$

$$dF_T = dL\ sin(\phi) - dD\ cos(\phi) \rightarrow dF_T = B\frac{1}{2}\ \rho\ V_{rel}^2\ c\ dr\ (C_l\ sin(\phi) - C_d\ cos(\phi)) \tag{2.2.9}$$

Where B is the number of blades, $C_l cos(\phi) + C_l sin(\phi) = C_n$ is the normal force coefficient and $C_l sin(\phi) - C_d cos(\phi) = C_t$ is the tangential force coefficient. C_n and C_t can be also written as:

$$C_n = \frac{F_N}{\frac{1}{2}\rho V_{rel}^2\ c} \qquad C_t = \frac{F_T}{\frac{1}{2}\rho V_{rel}^2\ c} \tag{2.2.10}$$

Where, in this definition, F_N and F_T are the normal and tangential force per unit of length $[\frac{N}{m}]$. The tangential force causes the rotation of the blade, and it is therefore responsible for the Torque generation, which can be expressed as $dQ = B\ r\ dF_T$ [3]:

$$dQ = B\frac{1}{2}\ \rho\ V_{rel}^2\ c\ r\ dr\ (C_l\ sin(\phi) - C_d\ cos(\phi) = 4\ a'(1-a)\rho U_\infty \pi r^3\ \Omega dr \tag{2.2.11}$$

The Thrust force exerted by the blade on the wind can be computed as [3]:

$$dT = \rho U_\infty^2\ 4a(1-a)\ \pi\ r\ dr \tag{2.2.12}$$

This expression is helpful to discuss the trend of the Thrust force with respect of the wind speed. Indeed, for below rated wind speeds, the Thrust force will increase with a quadratic dependence of the wind speed, being the induction factor constant. For above rated wind speeds, the pitching of the blades, to ensure a constant power, will make the induction factor to decrease. The decrease of the induction factor will overcome the increase of the wind speed, making the Thrust force to decrease for above rated wind speeds. Therefore, the maximum Thrust force will be found for the rated wind speed. The Thrust force can be qualitatively related to the deflection and the vibration of the blades and in particular the larger the Thrust the larger the deflection will be as well as the blade vibration. Both these two aspects constitute a perturbation source in terms of angle of attack fluctuations, because of the relative velocity induced by the vibration of the blades (e.g. aerodynamic damping) and this effect is larger for outboard stations. Moreover, if the blades are deflected, the swept area covered by the blades will result to be slightly lower with respect of the situation in which the blades are completely non-deflected; consequently, the error in the estimation of the induction factor for wind speeds close to rated will also be affected by the deflection of the blades.

Summing up, the Blade Element theory provides an expression for the element force acting on the blade element, while, the Momentum theory expresses the Thrust force acting on a thin actuator disk. The Blade Element Momentum theory couples these two aspects by imposing that these two forces have to be equal under the above mentioned assumptions, leading to the relationship [3]:

$$dT = B\ dF_N \tag{2.2.13}$$

As discussed at the beginning of the section, the BEM theory has been derived under several assumptions. In order make the model more representative of what is happening in reality, two main corrections to the model can be adopted, namely: Prandtl's tip loss factor and Glauert correction, which will be discussed in the following sections.

2.2.2 Prandtl's Tip Loss Factor

As introduced in section 2.2.1, some modifications need to be included in the BEM theory, in order to correct the assumptions according to which the theory has been derived. The Prandtl's tip loss factor is used to account for the fact that the rotor is not an annular element, but it is made of a finite number of blades [3]. It can be expressed as:

$$F = \frac{2}{\pi}\ cos^{-1}\ e^{-f} \tag{2.2.14}$$

Where $f = \frac{B(R-r)}{2\ r\ sin(\Phi)}$. The Pradtl's tip loss factor should be used as a multiplication factor for the equations previously derived, for instance, to correct the torque (equation 2.2.11) or the thrust force expression (equation 2.2.12). It is worth noticing that the unit of measure of F is radians, consequently, a conversion factor should be applied if the results is needed in degrees.

2.2.3 Glauert Correction for high values of a

In section 2.2.1, it has been shown that the wind speed at the rotor level can be computed as the average between the far upstream and the far downstream wind speed, with respect of the rotor level. The wind speed far downstream the rotor is strictly related to the developing of the wake behind the rotor. In particular, by increasing the thrust coefficient, the area of the wake will be larger and consequently the velocity far downstream would be lower, since C_t is proportional to the induction factor a; it follows that high C_t are related to high values of a. If the turbulent wake state becomes too large, it can no longer be neglected and it has to be included in the BEM model; the adjective 'too large' is associated to an induction factor higher than 0.4, where the classical BEM model has been proven to be not accurate [3]. The Thrust coefficient can be expressed as:

$$C_t = \frac{dF_N}{\frac{1}{2}\ \rho U_\infty^2\ dA} = \frac{(1-a)^2 \sigma C_n}{sin^2(\Phi)} \tag{2.2.15}$$

Where, for induction factor $a > 0.4$, empirical solutions can be used such as [3]:

$$c_t = \begin{cases} 4a(1-a)F, & \text{if } a \leq \frac{1}{3} \\ 4a(1-\frac{1}{4}[5-3a)a]F, & \text{if } a > \frac{1}{3} \end{cases} \tag{2.2.16}$$

Or, alternatively [3]:

$$c_t = \begin{cases} 4a(1-a)F, & \text{if } a \leq a_c \\ 4[a_c^2 + (1-2a_c)a]F, & \text{if } a > a_c \end{cases} \tag{2.2.17}$$

Where $a_c \approx 0.2$ [3]. Although, if $a > a_c$ the induction factor assumes a different form as [3]:

$$a = \frac{1}{2}\left[2 + K(1-2a_c) - ((K(1-2a_c)+2)^2 + 4(Ka_c^2 - 1))^{\frac{1}{2}}\right] \tag{2.2.18}$$

Where $K = \frac{4Fsin^2(\Phi)}{\sigma\ C_n}$

2.2.4 Atmospheric Turbulence

The concept of turbulence introduced in section 2.1.4 will be extended in this section, which will deal with the atmospheric turbulence. Atmospheric turbulence is strictly related to the concept of Atmospheric Boundary Layer (ABL). In section 2.1.3, the BL has been introduced referring to the length-scale of the considered object exposed to an air flow; the ABL arises when considering the earth scale-length. The atmosphere can be subdivided in layers which present similar properties; the ABL arises in the bottom part of the troposphere which, considering the ground level as reference height, extends itself up to 11 [km]. The nature of the ABL is strictly related to the daily variation of temperature, humidity, wind speeds and pollution, in combination with the terrain surface roughness and the synoptic forcing [15] [16]; indeed, the Earth's surface is exposed to radiative heat by the sun, which for instance would lead the Earth's surface to warm up over days and to cool down over nights. This would generate convective air movement, mainly driven by temperature and pressure gradients, which would modify the characteristics of the ABL.

All the phenomena described above play a role in affecting the characteristics of the ABL, which in turn affects the wind characteristics, making the nature of the ABL hard to predict for practical purposes; for this reason, it is handy to introduce a classification of the wind situation, referring to the turbulence intensity I and the mean value of the wind speed $\overline{U}$, which is usually taken at the hub height and the term average is referred to a 10 minutes time frame [24]. This two aspects are related by the standard deviation σ, as [16]:

$$I = \frac{\sigma}{\overline{U}} \tag{2.2.19}$$

As deeply discussed in [17], [18] and [19], the standard deviation as defined in equation (2.2.19), can be well approximated by a normal distribution. The variability of the standard deviation is mostly attributed to the atmospheric stability conditions and to the variability of the wind speed direction or of the surface roughness. The wind turbine design standards provide a scaling rule to relate the turbulence intensity level to the wind speed. In order to do so, referring to Table 2.1, the wind turbine class and the wind turbine characteristics should be selected. As specified by [24], the wind speed distribution is assumed to follow a Rayleigh distribution, over a 10 minutes period; the wind turbine class should be chosen in such a way for the average annual wind speed, at a given site, to be 20 % of the reference wind speed shown in Table 2.1. In order to differentiate among the different sites where a wind turbine can be placed (namely onshore, near-coastal and offshore), in section 4.5 and 4.6, the wind turbine class I has been associated with an offshore site, as well as wind turbine class II and III with a near-coastal and onshore site, respectively. This has been done to account for the fact that, due the lower presence of obstacles in an offshore site with respect of an onshore site, the average annual wind speed is expected to be larger. The turbulence characteristics are divided in three levels: low, medium and high turbulence, which respectively correspond to the characteristics C, B and A. Once the wind turbine class and the turbulence intensity characteristics have been chosen, the standards provide a scaling rules for the standard deviation of the wind speed as a function of the reference turbulence intensity and the wind speed. Subsequently, the turbulence intensity as a function of the wind speed can be simply derived by applying the definition of turbulence intensity (equation 2.2.19).

Wind Turbine Class	I	II	III
$V_{ref}[\frac{m}{s}]$	50	42.5	37.5
$I_{ref_A}[-]$	0.16	0.16	0.16
$I_{ref_B}[-]$	0.14	0.14	0.14
$I_{ref_C}[-]$	0.12	0.12	0.12

Table 2.1: *I_{ref} classification, where the designated categories A, B and C, stand respectively for, high, medium and low turbulence characteristics. [24]*

For an onshore site, the IEC 61400-1 v3 standards ([24]) should be used. For a normal turbulence model, the standard deviation of the turbulence should be taken as 90 % of the quantile for the given hub height wind speed. In particular, the standard deviation is equal to:

$$\sigma_x = I_{ref}(0.75V_{hub} + b) \tag{2.2.20}$$

where b is 5.6 $\left[\frac{m}{s}\right]$ and I_{ref} is the expected turbulence intensity value at 15 $\left[\frac{m}{s}\right]$. It is worth pointing out that the scaled turbulence intensity is along the longitudinal direction. The normal turbulence model also provides a correlation between the longitudinal standard deviation of wind speed and the lateral (σ_y) and vertical (σ_z) standard deviation of the wind speed. In particular $\sigma_y = 0.8\sigma_x$ and $\sigma_z = 0.6\sigma_x$. In Figure 2.7 the standard deviation and the turbulence intensity scaling with respect of the wind speed are shown for the three different turbulence intensity characteristics A, B and C. From this figure it can be noticed that the variability of the wind velocity magnitude increases with the wind speed itself, while the turbulence intensity follows an hyperbolic relationship, so the larger the wind speed the smaller I. This trend can be explained by thinking in terms of reduced frequency; indeed, being k inversely proportional to the relative wind speed, the larger the wind speed the smaller k will be (see section 2.3). Consequently, larger wind speeds are associated with a lower degree of unsteadiness which results in lower values of turbulence intensity.

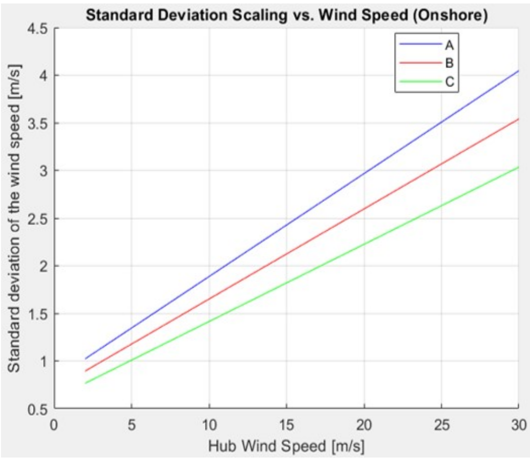

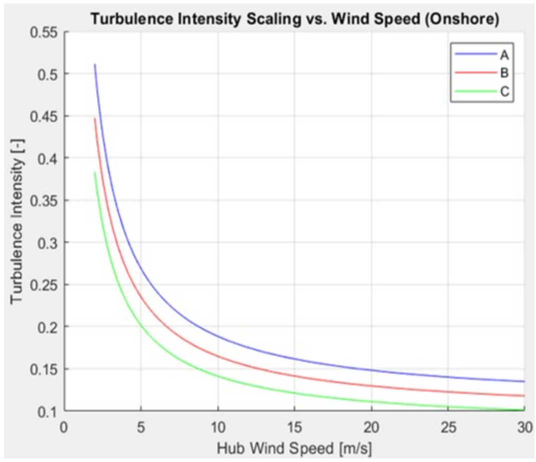

Figure 2.7: *Standard deviation of the wind speed (a) and Turbulence intensity (b) scaling for an Onshore site and for the three turbulence intensity characteristics A, B and C.*

If the turbulence intensity scaling is needed for a near-coastal or offshore site, the same approach can be repeated by referring to the IEC 61400-3 standards [25], which provide a different relationship between the standard deviation of the wind speed and the wind speed itself. In particular the standard deviation of the wind speed along the longitudinal direction can be derived according to:

$$\sigma_x = \frac{V_{hub}}{ln\left(\frac{z_{hub}}{z_0}\right)} + 1.28 \times 1.44 \times I_{15} \tag{2.2.21}$$

Where I_{15} is the value that the turbulence intensity assumes at 15 $\left[\frac{m}{s}\right]$ and it can be derived from Table 2.1. The terrain surface roughness can be estimated by using the Charnock's expression:

$$z_0 = \frac{A_c}{g}\left[\frac{k\ V_{hub}}{ln\left(\frac{z_{hub}}{z_0}\right)}\right] \tag{2.2.22}$$

Where A_c is the Charkock's constant which can be set equal to 0.011 [-] for open sea sites and 0.034 [-] for near-coastal sites. Furthermore, k is the Von Karman constant equal to 0.4 [-], g is the gravity acceleration constant (9.81 $\left[\frac{m}{s^2}\right]$), z_{hub} is the hub height while the z_0 which appears within the expression can be selected as 0.0002 [m] for open sea and 0.005 [m] for near-coastal sites. By using this expression in combination with equation 2.2.19, the standard deviation of the wind speed as well as the turbulence intensity can be plotted as a function of the hub wind speed, as shown in Figure 2.8.

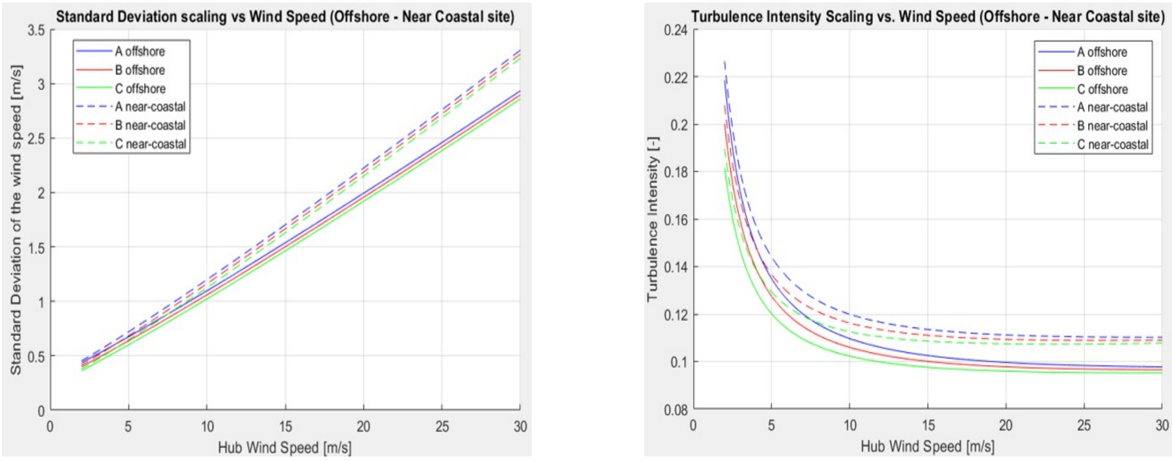

Figure 2.8: *Standard deviation of the wind speed (a) and Turbulence intensity (b) scaling for an Offshore and Near-Coastal site and for the three turbulence intensity characteristics A, B and C.*

2.2.5 Wind Shear

This section will discuss the topic of wind shear. The effect of the Atmospheric Boundary Layer results in a vertical wind velocity distribution, which is referred to as wind shear. Assuming neutral atmospheric conditions as specified in the IEC 61400-1 standards [24], wind shear can be modelled by a logarithmic law, as [4]:

$$U(h) = U_\infty \frac{ln(h) - ln(z_0)}{ln(h_0) - ln(z_0)} \tag{2.2.23}$$

Where h is the height, h_0 is the reference height, conventionally taken as 10m, because it is the height at which wind speed is measured. U_∞ is the far upstream wind speed and z_0 is the surface roughness, for which, typical pre-defined values can be used according to the terrain characteristics, as listed in Table 2.2. For heights above 100m, the logarithmic law has proved to be not accurate, because the influence of the surface roughness becomes negligible. In order to model the wind shear with better accuracy, the power law can be used [4]:

$$U(h) = U(h_0)\left(\frac{h}{h_0}\right)^\alpha \tag{2.2.24}$$

Where h_0 is the reference height (10m) and α is a coefficient which accounts for the characteristics of the surface and it should be assumed equal to 0.2 according to [24]; For a deeper classification, the following values are proposed: over flat land $\alpha = 0.2$, across open sea $\alpha = 0.1$, while for complex terrains $\alpha = 0$ [17]. These values are meant to be as an indication in case of lack of data; indeed, the exponent of the wind shear power law can also be estimated from the surface roughness as [17]:

$$\alpha = \frac{1}{ln\left(\frac{H}{zo}\right)} \tag{2.2.25}$$

Terrain conditions	$z_0[m]$
Open sea	0.0002
Blown sea	0.005
Lawn grass	0.008
Rough pasture	0.01
Fallow field	0.03
Crops	0.05
Few trees	0.1
Many trees, few buildings	0.25

Table 2.2: *Terrain roughness classification [4]*

The wind shear profile is also dependent on the atmospheric stability, indeed, equation (2.2.23) and (2.2.24) are only valid in neutral atmospheric conditions. In order to account for the stable and the unstable atmosphere, the formula must be corrected, as done in [38], by using the Monin-Obukhov Similarity Theory (MOST):

$$U(z) = \frac{u_*}{k}\left[ln\left(\frac{z}{z_0}\right) - \Psi_m(\zeta)\right]; \qquad with \quad \Psi_m(\zeta) = \int_{\frac{z_0}{L}}^{\frac{z}{L}} [1 - \Phi_m(\zeta)]\, d\; ln(\zeta) \tag{2.2.26}$$

Where u_* is the friction velocity, k is the von Karman constant equal to 0.4, L is the Monin-Obukhov length and $\zeta = \frac{z}{L}$ is the stability parameter. Indeed, whether $-2 < \zeta < 0$ the atmospheric condition is considered to be unstable, for $0 < \zeta < 1$ atmospheric condition is stable and for $\zeta = 0$ the atmosphere is in neutral conditions, consequently equation (2.2.26) equals equation (2.2.23), because $\Psi_m(\zeta) = 0$. The expression for the function Φ_m changes in accordance with the atmospheric conditions. In particular [38]:

$$\Phi_m^{unstable} = (1 - \gamma_1\zeta)^{(-\frac{1}{4})}; \qquad \Phi_m^{stable} = 1 + \beta\zeta \tag{2.2.27}$$

The coefficients γ_1 and β can be determined from the Kansas experiment [39], where $\beta = 4.7$ and $\gamma_1 = 15$, or from [40], where $\beta = 5$ and $\gamma_1 = 16$. By using the above mentioned equations, it can be noticed how wind shear results in a steeper profile in unstable condition, with respect of the neutral conditions, while the opposite holds for stable conditions, where the wind shear rises slower than in neutral conditions. Typically, the ABL is stable over nights and since the slope of the shear is lower than for neutral and unstable condition, the rotor disk might experience considerably large velocity gradients, up to 6 $\left[\frac{m}{s}\right]$; on the other hand, the ABL observed in a general day can be assumed to be in neutral conditions and in this case, considering reasonable values as $z_0 \approx 0.01[m]$, $u_* = 0.6\left[\frac{m}{s}\right]$ and D = 100 [m], the variation of the mean axial velocity across the rotor disk are in the order of 2 $\left[\frac{m}{s}\right]$ [26].

2.2.6 Yaw Misalignment, Skewed Wake and Advancing and Retreating Effect

This section will address the topic of yaw misalignment, as well as its effect on the load variation, which can be modelled by the Skewed Wake and the Advancing and Retreating Effect. The importance of including Yaw Misalignment effects is prompted by the evidence that, over a 10 minutes time series, the average yaw misalignment angle is found to be between 2 and 10 ° [37]. Yaw misalignment refers to the condition where the wind velocity direction is not perfectly perpendicular to the wind turbine rotor plane; this difference can be evaluated by defining a yaw misalignment angle β which expresses how much the wind velocity direction differs from the normal (to the rotor plane) direction. In yawed conditions, the inflow is strongly non-axisymmetric and moreover three dimensional effects play an important role, which is why the BEM theory results to be not accurate [13]. Indeed, if $\beta \neq 0$, the wake of a wind turbine experiences a deflection in the downstream wind direction. This deflection can be quantified by defining a wake skew angle χ according to [37]:

$$tan(\chi) = \frac{V_{rel}sin(\beta)}{V_{rel}cos(\beta) - u_i} \tag{2.2.28}$$

Where $V_{rel}cos(\beta)$ is the axial velocity component felt by the rotor, decreased by the induced axial velocity u_i and $V_{rel}sin(\beta)$ is the tangential velocity component at the rotor level. It must be noticed that the tangential component has been assumed unaffected by the induced velocity; this holds true if the yaw angle is small, because the tangential component of the perturbation can be considered to be small with respect of the rotational velocity component. The variation of the induced axial velocity is caused by 3-Dimensional effects, namely the tip trailing vortices along with the root vorticity. The combination of these effects leads to a load imbalance between the upwind and the downwind side of the rotor plane. As can be observed in Figure 2.9, by setting $\beta > 0$, $\psi = 0$ at the 6 o'clock position and a clock-wise rotational speed, the upwind side is defined for $0 < \psi < 180°$ while the downwind side for $180° < \psi < 360°$. It is worth noticing that the opposite would hold for $\beta < 0$. In order to determine the induced velocity distribution as a function of the azimuthal position of the blade, the following empirical model can be used [37]:

$$u_i = u_{i,0}[1 - A_1 cos(\psi - \varphi_1) - A_2 cos(2\psi - \varphi_2)] \tag{2.2.29}$$

Where $u_{i,0}$ is the rotor average induced velocity, while A_1, A_2, φ_1 and φ_2 are, respectively, the amplitudes and the phases of the induced velocity, modelled as a function of the radial position and the yaw angle and derived empirically. Evidences suggest that, if $\beta > 0$, the tip trailing vortices are slightly shifted towards the downwind side of the rotor plane, resulting in a larger induced velocity at $\psi = 270°$ [37], as also depicted in Figure 2.9. Indeed, by looking at equation (2.2.28), it can be seen how the maximum deflection of the wake occurs when the induced velocity is largest, namely at $\psi = 270°$ (3 o'clock position). This can be explained by thinking that the wind wake will propagate in the direction set by the skew angle, resulting in a stronger wake towards the downwind side of the rotor. A larger induced velocity field will make the longitudinal component of the relative wind speed to decrease, resulting in a lower AoA magnitude than for $\psi = 90°$, where the induced velocity is minimum. Besides, it must be pointed out that the reference system (0 azimuth when the blade is pointing down) is different for the one used in section 3.2.2, where the zero azimuth position is considered when the blade is pointing up. Consequently, all the considerations done in this section should be rotated by 180 °, to be consistent.

The Glauert model allows to estimate the average induced velocity of the rotor as [37]:

$$F_{ax} = \rho A_r (V_{rel} - u_{i,0})\ 2\ u_{i,0} \tag{2.2.30}$$

This expression proves that where the induced velocity is higher the axial force will be lower, because the relative velocity will decrease; the direct consequence is that the rotor will feel a load imbalance, with a stronger axial force in the upwind direction and a lower one in the downwind direction, generating a negative yaw restoring moment [37]. In order to assess the effect of a yawed system on the loading, the load variation is modelled through the advancing and retreating effect. In this case, the rotational component will not be constant over a revolution; in particular, at $\psi = 0$ the rotational component will be increased by the additional term $Usin(\beta)$, namely advancing with respect of the in-plane velocity component, while, at $\psi = 180°$, the rotational component will be decreased by the term $-Usin(\beta)$, meaning retreating with respect of the in-plane velocity component. The advancing and retreating blade effect is symmetric around zero azimuth and therefore it will be zero over a revolution, meaning that no restoring yaw moment will occur [37]. By looking at the velocity triangles, in particular, at $\psi = 0$ and at $\psi = 180°$, it can be shown where the AOA and the relative velocity are found to be maximum. In both cases, the longitudinal velocity component, resulting from the yaw misalignment, can be expressed as $Ucos(\beta)$, which assuming no wind shear nor tower shadow does not change between $\psi = 0$ and $\psi = 180°$. The tangential component $Usin(\beta)$, though, will have opposite sign at the two specified azimuthal positions. The reduction of the tangential component at $\psi = 180°$ will make the AoA to increase, reaching its maximum, while, the increase in the tangential component at $\psi = 0$ will make the relative velocity to increase. The loading of a wind turbine depends either on the AoA (related to the Lift and Drag coefficients) and on the relative velocity. As specified in [37], the increase in the relative velocity is the main driver for the load increase and consequently the load will be maximum at $\psi = 0$, assuming positive yaw angle. This can also be seen by looking at equations 2.2.8 and 2.2.13.

Finally, the dependency of the skew wake and the advancing and retreating effect on the tip speed ratio is evaluated. The skew wake effect is larger at high tip speed ratio, for instance, at low wind speeds. This is mainly due to the fact that the induced velocities are, normally, higher at high tip speed ratio (which makes sense since the axial induction factor is larger). Conversely, at high tip speed ratio, the advancing and retreating effect is restrained being the tangential component of the wind speed $Usin(\beta)$ small with respect of the rotational speed (Ωr), because of the low wind speed U. At low tip speed ratio the opposite is true. The advancing and retreating effect is amplified by the large wind speeds while the variation of the induced velocities is limited by the low induction factor, meaning that the skew wake effect is limited as well [37]. By applying a similar reasoning, it can be understood how the advancing and retreating effect is more relevant at inboard stations (low rotational speed component) while the skewed wake effect is dominant for outboard stations (larger induced velocity field).

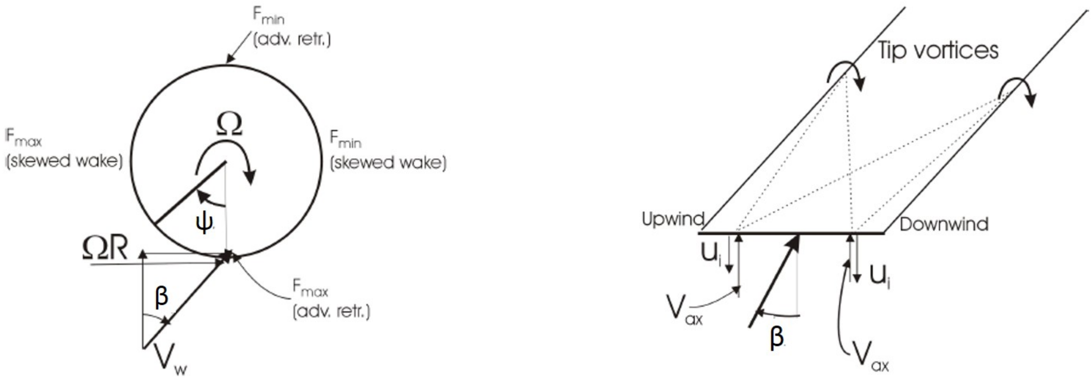

Figure 2.9: *Schematic Representation of the Advancing and Retreating and Skewed Wake effect [37]*

2.3 Unsteady Aerodynamics

This section aims to provide the basics of the unsteady aerodynamics related to HAWT. It is well known that wind turbine are likely to operate in unsteady inflow conditions. In this perspective, it is important to highlight that unsteady effects can also occur in laminar flow conditions and not only when turbulence is present [13]. In order to determine the extent to which a flow can be considered to be unsteady, the reduced frequency has been introduced, as [13]:

$$k = \frac{\omega c}{2V_{rel}} \tag{2.3.1}$$

where ω is the characteristic frequency of the flow, c is the chord and V_{rel} is the relative velocity seen by the airfoil. Since the reduced frequency depends on V_{rel}, each perturbation source that results in a change in the relative velocity would influence the degree of unsteadiness of the flow. In addition, the relative velocity is not the same along the blade span; due to the lower value of the rotational component of the velocity at the blade root cross sections, the resultant V_{rel} will increase moving towards the tip. This suggests that the reduced frequency will be larger at blade root cross sections meaning that those airfoils are more likely to experience more unsteady air flows. As discussed in [60], if $k < 0.05$ the problem can be classified as quasi-steady, meaning that the unsteady effects can be neglected, while, on the other hand, for larger values of reduced frequency the problem is considered to be unsteady. In addition, when $k > 0.2$ the airloads will be dominated by the unsteady effects and consequently the problem will be classified as highly unsteady.

Unsteady effects can be classified into two main families, depending on their time constant τ. Fast phenomena (e.g. unsteady profile aerodynamics) refer to the change in the sectional aerodynamic forces due to time-dependent fluctuations in the AoA. This effect accounts for the changes in circulation caused by the shed vorticity in the immediate near wake and it is associated with the airfoil length scale. The second family of unsteady effects (slow phenomena) includes the contribution of the variation of the trailing vortices over time and it is related to the rotor length scale; this is generally referred to as 'Dynamic Inflow'. The characteristic time constant for the two families can be found by dividing the characteristic length by the relevant relative velocity component, as [22]:

$$\tau_F = \frac{c}{\Omega r}; \qquad \tau_S = \frac{D}{U} \tag{2.3.2}$$

Where the subscripts F and S stand respectively for fast and slow, c is the blade chord, D is the rotor diameter and U is the axial wind speed. For wind turbine with a diameter of the order of 50m, τ_F varies between 0.2s and 0.01s at the blade root and blade tip, respectively, while τ_S is about 5-10s [22] or 1-1.5 rotor revolutions [13]. It is worth noticing that the slow phenomena time constant can be 1 or 2 order of magnitude larger than the fast phenomena τ. If a certain aerodynamic phenomena has a characteristic time constant which is considerably larger than the values presented above, it can be considered as quasi-steady. In addition, the time needed to fully recover the unsteady transient, is generally 4-5 τ; for instance, as far as dynamic inflow is concerned, the transient can last about 5-8 revolutions.

When unsteady effects occur, the relationship between the lift coefficient and the angle of attack deviates from the quasi-steady polar behavior. An example of this variation is provided in Figure 2.10, where the effect of dynamic stall on the C_l is shown. The dynamic lift polar results in a sort of circular loop, where the dynamic angle of attack continuously tries to follow the static angle of attack value, which is also changing in time [3]. The reason for this behavior is explained as follows as in [60] [14]. Initially, as the AoA increases, a reduction of the adverse pressure gradient will delay separation and simultaneously, vorticity starts accumulating in the LE region; these arguments makes the C_l to increase with the AoA beyond the static stall AoA. At a certain point, the vortex disturbance leaves the LE shifting along the chord-wise direction, still providing additional Lift. When the vortex disturbance is shed into the wake, there is a sudden decrease in the Lift, because of massive flow separation. Finally, the flow reattaches to the airfoil, but at a considerably lower AoA than the static stall angle of attack. For stability reasons, it is important that the mean slope of the dynamic lift $\frac{dC_l}{d\alpha}$ is positive for dynamic airfoil data in the post-stall region [3].

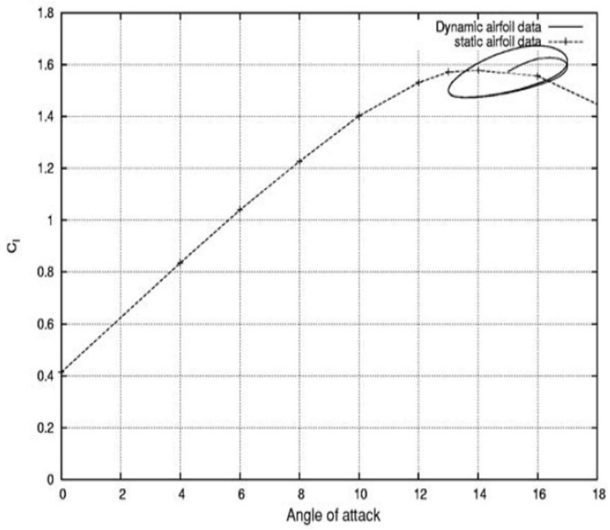

Figure 2.10: *Comparison between a quasi steady Lift polar and a dynamic Lift polar [3]*

2.4 Wind Energy Airfoil Design Requirements

This section addresses the design requirements for wind turbine airfoils. The required airfoil characteristics are generally subdivided in two main categories, namely structural and aerodynamic requirements. In this perspective, the blade are divided in three main regions: blade root, blade mid-span and blade tip, which are usually characterized by a specific thickness-to-chord ratio range. The relevance of the structural requirements for a blade root airfoil is considerably larger than for a blade tip cross section, while the opposite holds for the aerodynamic requirements [28]. Nowadays, wind turbines are becoming larger in size and the current industries trend is to use thicker airfoil section across a relevant part of the blade. A larger thickness implies higher stiffness, which allows the designer to reduce the weight of the blade and consequently fatigue loads and costs might decrease as well [30]. The general airfoil requirements and their relative importance depending on the considered blade section are summarized in Table 2.3

The presented work will optimize airfoils for HAWT according to aerodynamic requirements, consequently the structural requirements will not be discussed in this section. In terms of aerodynamic efficiency, the most important factor which is aimed to be maximized is the Lift-to-Drag ratio, which can either be expressed as $\frac{L}{D}$ or $\frac{C_l}{C_d}$. This major requirement has to be considered along with other relevant requirements that will be itemized below:

- **Geometrical Compatibility**: the first consideration when designing an airfoil is about its geometry and in particular, the location of the maximum thickness is of importance. If the maximum thickness is located forward, aerodynamic instability can be alleviated by decreasing

Design Parameter	Blade Root	Blade Mid-span	Blade Tip
Thickness-to-chord ratio [%]	>27	27-21	21-15
Structural load bearing requirements	High	Med	Low
Geometrical Compatibility	Med	Med	Med
Maximum Lift insensitive to LE roughness	-	-	High
Design Lift close to maximum Lift off-design	-	Low	Med
Maximum C_l and post-stall behavior	-	Low	High
Low Airfoil Noise	-	-	High

Table 2.3: *Wind Turbine Airfoil design requirements, for different blade sections. [29]*

the distance between the aerodynamic center and the center of shear and gravity. On the other hand, this would increase the distance from the TE, increasing the maximum strain. RISØ airfoils have been designed with a maximum thickness location between 27% and 33% of the chord [28].

- **Maximum Lift insensitivity to LE roughness**: Leading Edge contamination (e.g. dust, insects, erosion) can lead the boundary layer to an earlier separation along with a reduction of the maximum Lift coefficient; this issue is amplified in case of thicker airfoils [30]. Moreover, an earlier flow transition will also increase the drag coefficient which would result in a reduction of the Lift-to-Drag ratio [28]. RISØ airfoils minimized the roughness sensitivity by guaranteeing a maximum lift coefficient in natural transition to be roughly the same of the maximum lift coefficient in forced transition [28]. In particular, as used in the RISØ A series wind turbine airfoils, in forced transition, the flow is imposed to transit from laminar to turbulent within 5% and 10% of the chord, on the suction and pressure side respectively [30] [52].

- **Design Lift at off-design conditions**: given the stochastic and turbulent nature of wind, a wind turbine is likely to operate in off-design conditions and the extent of the off-design operations is mostly dependent on the power control method. Generally speaking, it is suggested to choose a design lift coefficient relatively close to the maximum lift coefficient, so that the Lift-to-Drag ratio can be as high as possible for most of the angles of attack below stall, as performed for the RISØ airfoil families [28].

- **Maximum Lift coefficient and post stall behavior**: for root blade cross sections, a high maximum lift coefficient allows a reduction of the blade solidity; although, given the relatively small contribution of the root airfoils to the overall aerodynamic performance, the highest $C_{l,max}$, which still allows to fulfill the structural requirements, should be selected [28]. As far as the tip airfoils are concerned, the argument becomes slightly difficult to define accurately. Several works [41], [42] discussed that, the need for high aerodynamic efficiency (related to AoA_{design}, $C_{l,design}$) and for low fatigue loads (ralated to AoA_{stall}, $C_{l,stall}$) impose that the interval between the AoA_{design} and the AoA_{stall} should be as broad as possible whilst the polar curve should be as smooth as possible over this range.

- **Low airfoil noise**: noise generation is mostly related to the turbulent flow streaming over the TE. The relevant actors in the phenomenon are the airfoil free stream velocity, mainly dependent on the rotor speed, and the shape that the BL assumes at the TE, which is strictly connected to the airfoil shape. As discussed in [28], airfoils can be designed for a minimum boundary layer thickness shape at the TE, although, this should be done as long as no negative effect on the roughness insensitivity are detected.

Chapter 3

Probabilistic Airfoil Design Approach

This chapter discusses how to use the probabilistic approach to describe the effect of non-uniform inflow perturbation sources on the angle of attack. In section 3.1, starting from the simple example of a dice, the fundamental concepts of probability will be presented. Section 3.2 will address how to model the perturbation sources in a probabilistic way. Theory of probability is broadly used in practice and especially in the business sector; for instance, casinos' revenues are based on the Law of Large number, which states that running the same experiment for a large number of times will increase the probability that the final outcome will differ from the expected result by a certain small amount (e.g. 1-2 %) [35]. This means that casinos might register losses over a small number of gambling rounds, but in the long-run, they will earn profit. When flipping a coin, the same concept holds; in this case, the result of the coin tossing could either be head or cross, and the more times the coin is flipped, the larger the probability that the final outcome will be close to 50% is. When it comes to describe wind environmental conditions, the number of possible values that the relevant parameters might assume is not as simple as just head or cross. This chapter can be considered as preparatory to the probabilistic design space mapping that will be carried out in section 3.4. The probabilistic design space mapping will answer to questions such as: how many faces should a dice have in order to represent all the possible values that the turbulence intensity can assume? And what is the probability of a certain combination of parameters to occur? The influence of the different values of the parameters on the angle of attack fluctuations will be evaluated as well.

3.1 Theory of Probability Background

This section will introduce the concept of probability presenting the fundamentals of the Theory of Probability, discussing the most important principles which will be used in this work. Probability can be defined as the science of uncertainty. It gives a set of rules and mathematical expressions to address unknown problems in the most reasonable way, based on limited knowledge [35]. The origin of probability has been linked with observations regarding games of chances; for instance, when rolling a six-faced dice, 6 different outcomes are possible (namely: 1, 2, ... , 6). The collection of the possible outcomes relative to a certain experiment goes by the name of sample space S. In addition, it is possible to define an event as a subset of sample spaces which satisfy a given condition [34]; referring again to the rolling of a six-faced dice, if the probability that an even number comes out is wanted, it is possible to define an event A as a subset of the sample space which contains all the points that verify the conditions for the extracted number to be even. In this example, the sample space and the event would be defined $S = \{1, 2, 3, 4, 5, 6\}$ and $A = \{2, 4, 6\}$. The probability of an event to occur can be computed by dividing the number of elements of an event by the total number of elements of the sample space, as follows [34]:

$$P(A) = \frac{N(A)}{N(S)} \tag{3.1.1}$$

Where N(A) and N(S) stand respectively for number of elements of an event A and of a sample space S. This definition is referred to as uniform probability. Referring again to the dice example, it is clear how the probability of each number to result from the dice rolling is the same and equal to $\frac{1}{6}$; same reasoning applies if the probability of an even number to come out is wanted, in this case it would be $\frac{1}{2}$. However, this formula only applies if each event is assumed to be independent of the others; for instance, how to calculate the probability of a number to be either even and lower than 5?

or how to compute the probability that the result of a rolling will be a 2, given that it is known that extracted number will be even? These problems requires the definition of other types of probability, which will be presented in section 3.1.1.

3.1.1 Marginal, Joint and Conditional Probability

In the previous section, the general definition of probability has been provided. This section will further on discuss this topic by introducing the definition of marginal, joint and conditional probability. Let's assume to carry out a survey where people are divided by gender; the purpose of the survey will be to evaluate how many people will enjoy reading a master thesis on the probabilistic design for HAWT airfoils. The fictitious result of this analysis can be summarized in a Table of Probability, shown in Table 3.1.

-	Yes [%]	No [%]	Tot
Male [%]	12	34	46
Female [%]	16	38	54
Tot	28	72	100

Table 3.1: *Tables of Probabilities example about how many people, divided by gender, would enjoy reading a master thesis about probabilistic design for HAWT airfoils*

The marginal probability refers to the probability of an event to occur without considering outcomes of other experiments; marginal probability is always related to a single experiment, meaning that that event has been considered to be independent on any other. Two events are said to be independent if the multiplication formula applies, namely $P(A \cap B) = P(A)P(B)$, where the symbol $\cap$ stands for 'intersection' [35]. The intersection of two events is given by the values which are present in both sets. If the events do not depend upon each other, the probability of the intersection of the events A and B is simply given by the product of the probability measure of the events A and B. Referring to the example, marginal probability can be visualized in the marginal columns in the table of probabilities. In particular, it relates to questions such as: what is the marginal probability of a person enjoying reading the master thesis? The answer would be 28%; or, what is the marginal probability that a person who joined the survey is male? 46%. It can also be noticed that the sum of the marginal probability in a row, or in a column, equals 1, which is the total probability.

If the outcomes of more experiments need to be considered, for a certain probability calculation, the concept of joint probability is needed; joint probability, given two events, is defined as the probability for both events to occur simultaneously, meaning $P(A \cap B)$. In the previous example, the joint probabilities can be identified in the central part of the tables. For instance, what is the probability of a person not enjoying the thesis and being female ($P(No \cap Female)$)? By looking at the intersection between the 'No' column and the 'Female' row of the table of probabilities, the value is 38%.

Finally the concept of conditional probability can be presented. Conditional probability aims to calculate the probability of a certain event B to occur, when it is already known that another event A has taken place. In the presented example, the conditional probability can be associated with the question: given that a person enjoys reading the thesis, what is the percentage that it is a male?. Conditional probability, in mathematical form, can be expressed as $P(B|A)$, which can be read as probability of B given A has occurred. In this case, the outcomes of A and B are not independent, the probability occurrence of B given A is calculated as the fraction of time in which both events occur, meaning the joint probability $P(A \cap B)$, when subject to the condition that only A takes place P(A), which expresses the marginal probability. In the example, the joint probability of a person enjoying the thesis and being male is 12% while the marginal probability of a person enjoying the thesis is 28%. By diving this two values, the conditional probability will be 43 %. In particular, assuming that A and B depend on each other and under the assumption of $B_1, B_2, ..., B_n$ being a finite family of mutually exclusive and exhaustive events and by letting A be any events, the Bayes' Theorem states that [34]:

$$P(B_k|A) = \frac{P(A \cap B_k)}{P(A)} = \frac{P(B_k)P(A|B_k)}{\sum_{i=1}^{n} P(B_i)P(A|B_i)} \tag{3.1.2}$$

It can be shown why this formula does not apply if A and B are independent. Indeed, $P(A \cap B) =$

$P(A)P(B)$, which would lead to $P(B_k|A) = P(B)$; this means that the occurrence of A has no influence on the occurrence of B and vice versa [34].

3.1.2 Cumulative Distribution Function

The cumulative distribution function (cdf) is strictly related to the concept of probability density function; indeed, it can be considered as the integral of a pdf given the two extremes (under the assumption of continuity). In particular, while the pdf of a random variable X indicates what is the probability of X to be within a certain interval, the cdf expresses what is the probability of a certain variable X to be lower or equal than a given value x. The mathematical formulation is the following [35]; given a random variable X, its cumulative distribution function is the function $F_X : R^1 \rightarrow [0, 1]$ defined by $F_X = P(X \leq x)$.

The cumulative distribution function has relevant properties, which will be summarized below [35]:

- $0 \leq F_X(x) \leq 1$ for all x;
- $F_X(x) \leq F_X(y)$ if $x \leq y$;
- $\lim_{x\rightarrow\infty} = 1$;
- $\lim_{x\rightarrow-\infty} = 0$.

3.1.3 Change of Variable

In section 3.1 the concept of probability density function has been introduced; this section discusses the topic of changes of variable of a probability density function.

The Density function method allows to derive the probability density function of a random variable R_2 given the pdf of another random variable R_1 [34]. Indeed, given a random variable R_1 on a probability space S and a real-valued function g on the reals, the variable R_2 is defined as $R_2 = g(R_1) \rightarrow R_2(s) = g(R_1(s))$, where $s \in S$. The fact that R_2 would still be a random variable is guaranteed by the continuity of g, if R_2 is defined as $g(R_1)$. It is worth pointing out that, in this discussion, R_1 is the input to the system, the g-function represents the system itself while R_2 plays the role of the output of the system. Finally, the explicit formula to obtain the pdf of R_2, in terms of the pdf of R_1 is expressed as [34]:

$$f_2(y) = \sum_{j=1}^{n} f_1(h_j(y))|h_j\,'(y)| \tag{3.1.3}$$

Where $f_1(h_j(y))|h_j\,'(y)| = 0$ if y does not belong to the domain of h_j. It must be point out that this formula is valid for 1-Dimensional change of variable. Similarly, the expression to compute a multi-dimensional change of variable can be written as [35]:

$$f_{Z,W}(z, w) = f_{X,Y}(h(z, w))|J(h^{-1}(z, w))| \tag{3.1.4}$$

Where J is the Jacobian of h. This equation is valid under the assumptions of X and Y to be absolutely continuous and $h_1, h_2 : R^2 \rightarrow R^1$ are differentiable functions. Moreover, it is assumed that if $h_1(x_1, y_1) = h_1(x_2, y_2)$ and $h_2(x_1, y_1) = h_2(x_2, y_2)$ it follows that $x_1 = x_2$ and $y_1 = y_2$ [35].

3.1.4 Probability Density Functions in Wind Applications

This section aims to present the most important probability density functions used in wind turbine applications and it will mainly focus on four distributions, namely: Normal (or Gaussian) distribution, log-normal distribution, Weibull distribution and Gumbel distribution.

The normal distribution is of importance in the discussion because it allows to describe a stochastic process, which can be used to model the atmospheric boundary layer turbulence, according to [32]; indeed, it allows to represent the distribution of the perturbation velocity which results from the atmospheric turbulence. Given a random variable X, which is normally distributed, with mean μ and standard deviation σ (or variance σ^2), the random variable X can be written as X $\approx N(\mu, \sigma^2)$. The probability density function of X is given by [34], where $-\infty < x < \infty$:

$$f(x) = \frac{1}{\sigma\sqrt{2\pi}} e^{[-\frac{1}{2}(\frac{x-\mu}{\sigma})^2]} \tag{3.1.5}$$

This expression can be related to the atmospheric boundary layer turbulence modelling by calling x the perturbation velocity which results from the atmospheric turbulence and by taking the turbulence intensity I as standard deviation, with a mean of zero. Moreover, it has been found that the yaw misalignment probability of occurrence can be approximated to have a normal distribution as well. [20] provides a method to determine the yaw misalignment probability based on LIDAR and SODAR data from the Dutch Onshore wind farm 'Slufterdam-West'. It has been found that the LIDAR method gives a better estimation of the mean yaw misalignment, while the SODAR method, provides a better estimation of the yaw misalignment spread. Since it is wanted to determine what is the probability of yaw misalignment to be between certain values (e.g. between -5 and 5 °), the spread of the yaw misalignment is more important for the present analysis and consequently the SODAR method has been followed. The yaw misalignment is obtained by deducting the direction of the nacelle from the direction of the wind speeds (from SODAR measurements). Appendix D of [20] provides a MATLAB code to simulate the yaw misalignment, which has also been used in this work. The code generates an histogram which has been approximated by a normal distribution and the mean and standard deviation which best match the histogram have been used for the analysis, depicted in Figure 3.1.

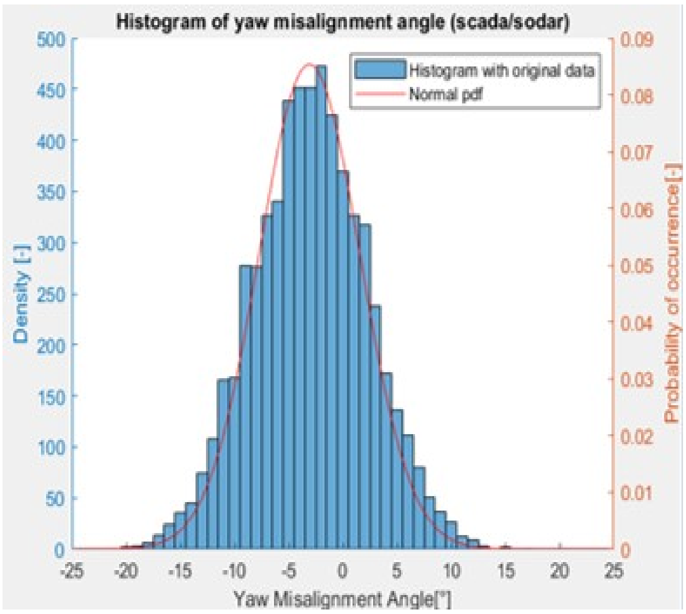

Figure 3.1: *Histogram and Probability of occurrence of Yaw Misalignment based on SODAR data*

While the normal distribution can be used to derive the perturbation velocity given the turbulence intensity, in order to obtain the conditional probability of occurrence of turbulence intensity given the mean value of the wind speed, a log-normal distribution must be used. The function which expresses the log-normal distribution comes from equation 3.1.5 and it can be written as:

$$f(x) = \frac{1}{x\ \sigma\sqrt{2\pi}} e^{\left[-\frac{1}{2}\left(\frac{log(x)-\mu}{\sigma}\right)^2\right]} \tag{3.1.6}$$

[21] provides an empirical approach to determine the two distribution parameters, namely $\hat{a_1}$ and $\hat{a_2}$, which are substituted to μ and σ in the log-normal pdf. These distribution parameters have been obtained by the fit of actual data. In particular, [21] provides the empirical expression for $\hat{a_1}$ and $\hat{a_2}$ based on data from two sites, an offshore (Vindeby) and a near-coastal one (Gedser), while no data have been found in the literature for an onshore site. An example of the probability density distribution of the turbulence intensity given the mean wind speed is provided in Figure 3.2, relative to the Gedser site, while the expressions for the distributions parameters are showed below, both expressed as a

function of the mean wind speed, where the subscript V and G stands respectively for Vindeby and Gedser:

$$\hat{a_{1,V}} = -0.002657U^2 + 0.17916U - 1.8744 \qquad with \;\; U < 33.7 \left[\frac{m}{s}\right] \tag{3.1.7}$$

$$\hat{a_{2,V}} = 29.628e^{-0.10042U-3.9311} \tag{3.1.8}$$

and:

$$\hat{a_{1,G}} = -0.002380U^2 + 0.16283U - 1.793 \qquad with \;\; U < 34.2 \left[\frac{m}{s}\right] \tag{3.1.9}$$

$$\hat{a_{2,G}} = 35.162e^{-0.0727U-4.005} \tag{3.1.10}$$

A final remark should be discussed about the applicability of the turbulence intensity model based on the Gaussian distribution. Indeed, the log-normal approximation of the pdf of the standard deviation has proven to be accurate up to a 2.5 standard deviation from the mean wind speed, as shown in [17]; for larger standard deviation values, the accuracy through which the turbulence intensity I can be approximate by a log-normal distribution decays. In addition, this model can still be considered to be accurate for fatigue analysis, although, problems might arise if the log-normal model is used for extreme wind event calculation [17].

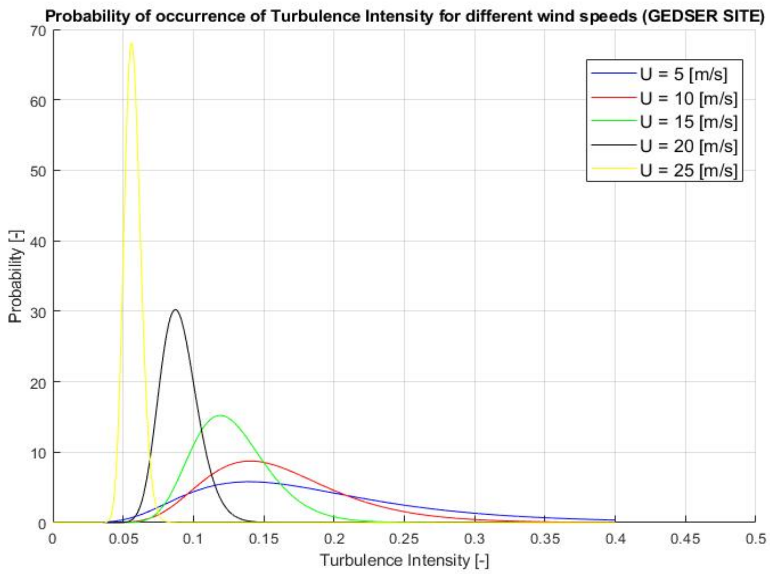

Figure 3.2: *Conditional probability of occurrence of turbulence intensity given the wind speed, for different mean wind speed values*

Another recurring pdf in HAWT application is the Weibull distribution, used to determine the probability distribution of the wind speeds at a given site. The importance of this distribution in practice is mostly linked to the calculation of the Annual Energy Production (AEP) of a wind turbine. Indeed, by knowing what is the probability of a certain wind speed to occur, it is possible to calculate the related generated power; by doing this for all the possible values that the wind speed is expected to assume over a year at a given location, the AEP can be computed. The Weibull pdf and cdf can be respectively written as [3]:

$$f(U) = \frac{k}{A}\left(\frac{U}{A}\right)^{k-1} e^{-\left(\frac{U}{A}\right)^k}; \qquad F(U) = 1 - e^{-\left(\frac{U}{A}\right)^k} \tag{3.1.11}$$

Where k and A are respectively the shape and the scale parameters. As the name suggests, the shape parameter is related to the shape of the distribution itself, meaning that it allows the pdf to approximate as much as possible the histogram which originally contains the wind speed information, before the pdf is calculated. The scale parameter allows to convert the wind speed from the reference height to the hub height, without modifying the shape of the distribution. In order to obtain the Weibull pdf for a real site the procedure is the following: organizing actual wind speed data from the site in an histogram and consequently approximating the shape of the histogram with a Weibull distribution. The scale and the shape parameters which allows for the best match between the two will be used in the analysis; Figure 3.3 gives an example of the Weibull distribution, where the original histogram data are from the wind farm Egmond aan Zee from 04/07/2008 to 03/07/2009.

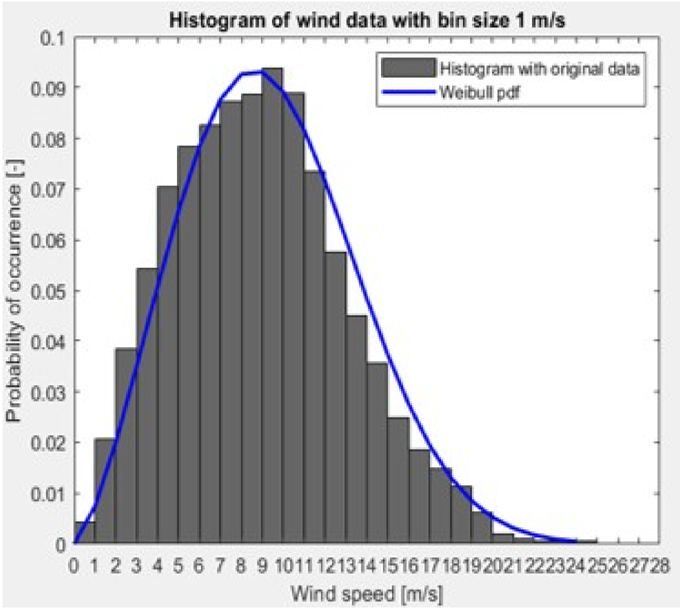

Figure 3.3: *Probability of occurrence of the wind speed and histogram with original data*

Another common pdf in HAWT application is the Gumbel distribution, which is mostly used for extreme wind speed prediction. For instance, when sizing the support structure of wind turbine an extreme value analysis must be performed, to ensure that, over its lifetime, even in case of abnormal conditions, the wind turbine will be able to withstand the extreme loads. Moreover, in order to obtain an acceptable result, the minimum required data length for the analysis is 10 years [24]. The Gumbel cdf and pdf can be expressed as [36]:

$$f(x, \mu, \beta) = \frac{1}{\beta} e^{-\left(z+e^{-z}\right)}; \qquad F(x, \mu, \beta) = e^{-e^{-z}} \tag{3.1.12}$$

Where $z = \frac{x-\mu}{\beta}$, $-\infty < x < \infty$, x is a random variable, μ is the mode value (also referred to as location parameter) and β is the scale parameter. The scale parameter can be estimated from the standard deviation as $\sigma = \frac{\beta\pi}{\sqrt{6}}$, according to [36].

3.2 Influence of Non-Uniform Inflow Conditions on the AOA

In this section, the influence of non uniform inflow condition, namely wind shear (section 3.2.1), yaw misalignment (section 3.2.2) and atmospheric turbulence (section 3.2.3), on the angle of attack is evaluated. The modelling of wind shear and yaw misalignment has been addressed with a deterministic method, while, the atmospheric turbulence is introduced by using a probabilistic approach. The combined effect of the mentioned perturbation sources will be finally addressed in section 3.2.4.

3.2.1 Wind Shear

The reference system used to model wind shear for wind turbine applications is shown in Figure 3.4, where the hub height is considered as reference height. By calculating what wind speed will be experienced by the wind turbine at the hub height, it can be scaled to obtain the velocity profile experienced by the airfoil in the revolution motion. The height can be parametrized as [32]:

$$h = h_0 + r\ cos(\psi) \tag{3.2.1}$$

Where r is the radius of a given blade section and ψ is the azimuth angle, which is used to parametrize the position of the blade in the revolution motion. By substituting this result in equation (2.2.23), wind shear can be modelled as:

$$U(h) = U_\infty \frac{ln(h_0 + r\ cos(\psi)) - ln(z_0)}{ln(h_0) - ln(z_0)} \tag{3.2.2}$$

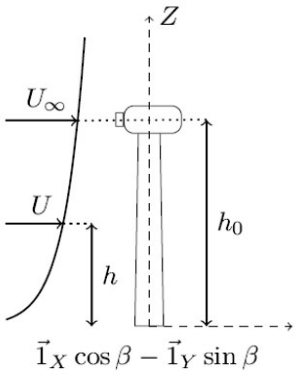

Figure 3.4: *Wind Shear view [32]*

3.2.2 Yaw Misalignment

Yaw Misalignment has been modelled according to the reference system depicted in Figure 3.5. For the sake of simplicity, all the blade sections are assumed to rotate in the same rotor plane; in order for this assumption to be true, the cone angle has been neglected and the stiffness of the blades is assumed to be infinite. Moreover, the far upstream wind speed vector $\overrightarrow{U_\infty}$ is assumed to have only the stream-wise (X) and lateral component (Y), meaning that it is considered 2-dimensional while its magnitude U_∞ varies along with the vertical direction (Z), namely wind shear is included. According to the convention of Figure 3.5a and the above mentioned assumptions, the far upstream wind velocity can be written as $\overrightarrow{U} = U_x \overrightarrow{1}_x + U_y \overrightarrow{1}_y$, where [32]:

$$U_x = U\ cos(\beta) \qquad and \qquad U_y = -U\ sin(\beta) \tag{3.2.3}$$

Where β is the yaw misalignment angle. Besides, the advancing and retreating blade effect (see section 2.2.6) has been used to model the geometric effect of yaw misalignment on the far upstream velocity vector $\overrightarrow{U}$ components. Given the previous assumptions, the wind speed experienced by a blade section (subscript r) can be expressed as [32]:

$$U_{r,x} = U_x[1 - \overline{a} - Ksin(\psi)] \qquad and \qquad U_{r,y} = U_y \tag{3.2.4}$$

Where $\overline{a}$ is the azimuthally and radially averaged axial induction factor, corrected by a parameter K$sin(\psi)$, which provides the axial induction factor at each given blade section and azimuthal position; this term allows to include the skewed wake effect in the model. In particular, K can be expressed as [32]:

$$K = \frac{15\pi}{32}\frac{r}{R}tan\left(\frac{\beta(0.6\overline{a} + 1)}{2}\right) \tag{3.2.5}$$

As can be observed, K is a function of the tangent of the yaw angle; this means that if β is small, the contribution of K is almost negligible. For simplicity, the lateral wind speed component does not include the skewed wake effect, assuming a small yaw angle, because the tangential component of the perturbation is small with respect of the rotational speed. By looking at Figure 3.1 it can be seen how the probability of large yaw misalignment angles to occur in practice is rather small, which justifies this hypothesis. In order to relate the effect of yaw misalignment to the fluctuations of the angle of attack, the velocity components obtained in equation (3.2.4) must be expressed according to the reference frame of the airfoil. By recalling that all the blade sections are assumed to rotate in the same plane and referring to Figures 3.5a and 3.6, the wind velocity components in the direction normal ($\perp$) and tangent ($\|$) to the plane of rotation can be written as [32]:

$$U_{r,\perp} = U_{r,x} \qquad and \qquad U_{r,\|} = U_{r,y}cos(\psi) \tag{3.2.6}$$

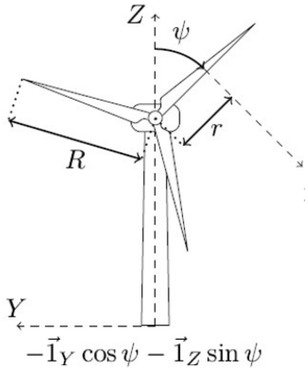

(a) *View from upstream [32]*

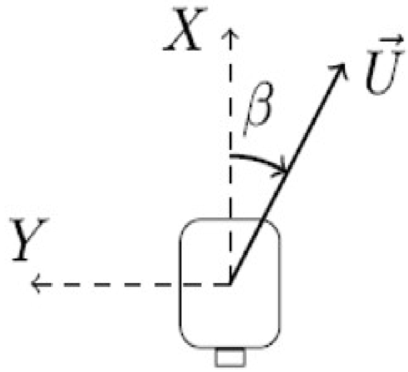

(b) *View from above [32]*

Figure 3.5: *Reference system used to model yaw misalignment*

3.2.3 Atmospheric Turbulence

The influence of the atmospheric turbulence is modelled by defining a relative perturbation δ, dependent on the turbulence intensity I. This relative perturbation is introduced in the longitudinal component of the wind speed and it influences its magnitude. The contribution of the turbulence perturbation in the tangential direction has been neglected. This is reasonable, since the rotational component is large, a small perturbation in the tangential direction will not generate a relevant angular variation (which becomes more and more true moving towards outboard stations) and besides, the tangential component of the turbulence intensity is smaller with respect of the longitudinal component [32]. This two arguments justify the non dependency of the tangential wind velocity component on the relative perturbation caused by turbulence intensity. Finally, by defining the turbulent wind velocity vector $\overrightarrow{V}$, its normal and tangential component, respectively, can be written as [32]:

$$V_{r,\perp} = U_{r,\perp}(1+\delta) \qquad and \qquad V_{r,\|} = U_{r,\|} \tag{3.2.7}$$

Where $U_{r,\perp}\ \delta$ is the instantaneous fluctuation of the longitudinal component of the relative velocity at a given blade section.

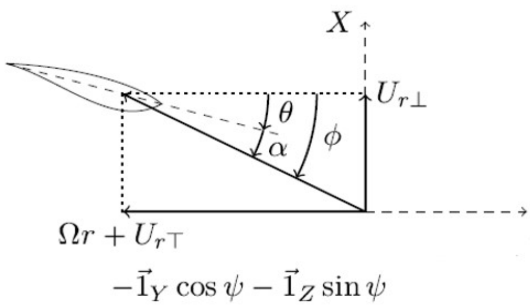

Figure 3.6: *View of a blade section, where the subscript T in the figure stands for $\|$ in the text [32]*

3.2.4 Combination of Perturbation Sources

In this section the relative contribution of each perturbation source will be combined in order to derive the final expression which relates the influence of wind shear, yaw misalignment and atmospheric turbulence with the AoA fluctuations, as performed in [32]. From Figure 3.6 it is possible to define the inflow angle as:

$$tan(\phi) = \frac{V_{r,\perp}}{\Omega r + V_{r,\parallel}} = (1+\delta)tan(\phi_0) \tag{3.2.8}$$

Where ϕ_0 is the non-perturbed local inflow angle expressed as:

$$\phi_0 = atan\left(\frac{cos\beta(1-\overline{a}-Ksin\psi)}{\lambda_r - sin\beta cos\psi}\right) \tag{3.2.9}$$

Where K is defined as in equation (3.2.5) and the wind shear effect is hidden in the local tip speed ratio definition, which can be written as:

$$\lambda_r = \frac{\Omega r}{U} = \frac{\Omega r}{U_\infty}\frac{ln(h_0)-ln(z_0)}{ln(h_0+rcos\psi)-ln(z_0)} \tag{3.2.10}$$

By recalling the definition of the inflow angle $\phi = \theta + AoA$, the angle of attack will be:

$$AoA = \phi - \theta = atan[(1+\delta)tan(\phi_0)] - \theta \tag{3.2.11}$$

The angle of attack fluctuations can be written as the difference between the non-perturbed local angle of attack and the perturbed local angle of attack, as follows:

$$AoA_\delta = AoA - AoA_0 = atan[(1+\delta)tan(\phi_0)] - \phi_0 \tag{3.2.12}$$

However, this expression holds only if the pitch angle does not change during the perturbation; this is assumed to be true considering the time-scale of turbulence to be much smaller than the time the pitch control needs to adjust the pitch angle to the fast changes in the inflow conditions.

As discussed in section 3.1.4, the relative velocity perturbation can be described by a normal (or Gaussian) probability density function. Where the the mean $\mu = 0$ and the standard deviation $\sigma = I$, resulting in:

$$p(\delta) = \frac{1}{\sqrt{2\pi}I}e^{-\frac{1}{2}\left(\frac{\delta}{I}\right)^2} \tag{3.2.13}$$

Once that the probability of occurrence of the relative perturbation δ has been found, the probability density function for the AoA fluctuations can be derived by using the density function method (see section 3.1.3). The first step is writing δ as a function of the AoA fluctuations AoA_δ, using equation 3.2.12:

$$\delta = \frac{tan(\phi_0 + AoA_\delta) - tan(\phi_0)}{tan(\phi_0)} \tag{3.2.14}$$

Subsequently, by applying equation (3.1.3), the pdf that describes the AoA fluctuations can be computed by:

$$q(AoA_\delta|\psi) = \left|\frac{d\delta}{dAoA_\delta}\right| p(\delta) = \left|\frac{1+tan^2(\phi_0+AoA_\delta)}{tan(\phi_0)}\right| p\left(\frac{tan(\phi_0+AoA_\delta)-tan(\phi_0)}{tan(\phi_0)}\right) \tag{3.2.15}$$

And finally

$$q(AoA_\delta|\psi) = \frac{1}{\sqrt{2\pi}I\,|tan(\phi_0)|}\left|1+tan^2(\phi_0+AoA_\delta)\right| e^{-\frac{1}{2}\left(\frac{tan(\phi_0+AoA_\delta)-tan(\phi_0)}{I|tan(\phi_0)|}\right)^2} \tag{3.2.16}$$

In order to linear map the probability function from the domain of δ to the domain of α_δ, the Jacobian of the function must be differentiable at each point of the domain, which is the necessary condition for the Talylor's approximation to apply [33]. Consequently, in order for the tangent function to be considered monotone and continuously differentiable, the necessary assumption performed in [32] is that $\phi_0 + AoA_\delta = atan[(1+\delta)tan(\phi_0)] \quad \in \ ]-\frac{\pi}{2}, \frac{\pi}{2}[$.

Equation (3.2.16) appears rather complicated and it is a function of several parameters, in particular: turbulence intensity, surface roughness and yaw angle to describe the relative influence of the perturbation sources, the local tip speed ratio to account for the specific wind turbine operating conditions, while azimuth angle and local radius are used to adjust the effect of the perturbation sources to the given blade section and to the given position within the rotation motion. By assuming a constant rotational speed and by recalling that all the blade sections are rotating in the same rotor plane, it can be conclude that a given blade section will experience a given azimuthal position periodically. Consequently, the marginal probability of the AoA fluctuations can be computed by integrating equation (3.2.16) over an entire revolution, in order to include all the possible values for ψ.

3.3 Preliminary Analysis of the model: Limit Cases Analysis

In the previous section, the expression which allow to describe the probability of the angle of attack fluctuations has been derived. In particular, referring to equation 3.2.16 it is possible to highlight five parameters which will influence the probability of AoA fluctuations, namely wind perturbation parameters: I (turbulence intensity), z_0 (terrain roughness), β (yaw misalignment angle) and wind turbine operational parameters: TSR (tip speed ratio) and $\frac{r}{R}$ (radial position). According to the values that each of these parameters assume, the resultant pdf will be different. This section aims to evaluate how the angle of attack fluctuations would change if the relevant parameters highlighted above vary. The section is organized in the following way: firstly, the single contribution of each independent source on the AoA fluctuation will be studied; consequently, the combined case (C) will be evaluated. Initially, two limit cases will be presented: considering low values for each source (denoted by the letter L) and assuming high values for each source (denoted by the letter H); then, the different combinations of the above mentioned parameters will be analyzed to discuss intermediate cases as well in section 3.4. In addition, as presented in section 2.4, blade root sections have a small contribution to the aerodynamic performance of the airfoil, because they must satisfy structural requirements; for this reason, the analysis is limited to blade sections with $\frac{r}{R} \geq 0.2$.

The procedure through which the results are obtained is expressed as follows. The first step is calculating the AoA fluctuations as a function of the azimuth angle ψ. This can be performed by combining equation (3.2.9), (3.2.10) and (3.2.12). The relative perturbation δ is estimated using equation (3.2.13) with the proper value of the turbulence intensity I. Finally, the combined probability density function is obtained by equation (3.2.16). In order to present a comprehensive result, after evaluating the AoA fluctuations for each azimuthal position, the difference between the maximum angle of attack magnitude and the minimum angle of attack magnitude, namely the range of AoA fluctuations, will be plotted as a function of the radial position, as:

$$\Delta AoA = AoA(\psi_{max}) - AoA(\psi_{min}) \tag{3.3.1}$$

Where ψ_{max} and ψ_{min} are the azimuth angles at which the maximum and minimum value of the magnitude of the AoA is reached. It is worth noting that, the azimuth angle at which the maximum and minimum AoA magnitude is detected, varies case by case. The values used for the analysis are shown below; in addition, $U_\infty = 11.4\ \frac{m}{s}$, a = 0.25 [-], $\Omega = 1.27\ \frac{rad}{s}$, R = 63m and the hub height h_0 = 90m according to the 5MW NREL wind turbine.

Case	Terrain Roughness ($z_0[m]$)	Yaw Angle ($\beta[°]$)	Turbulence Intensity (I [-])	$\frac{r}{R}[-]$
WS (L)	0.0002	0	0	0.2-1
WS (H)	0.2	0	0	0.2-1
YM (L)	0	5	0	0.2-1
YM (H)	0	25	0	0.2-1
TI (L)	0	0	0.05	0.2-1
TI (H)	0	0	0.3	0.2-1
C (L)	0.0002	5	0.05	0.2-1
C (H)	0.2	25	0.3	0.2-1

Table 3.2: *Simulation Matrix explaining the cases used for the model preliminary analysis*

3.3.1 Influence of Wind Shear, Yaw Misalignment and Atmospheric Turbulence

This section will discuss the influence of each independent source on the AoA, in order to identify what are the most relevant effects in terms of range of AoA fluctuations. Figure 3.7a and b represent the fluctuations of the AoA for the L and H case, when only WS is considered. In particular, the left-hand figure shows, for each radial position, how the AoA varies along the azimuthal position. It can be noticed how the maximum and the minimum AoA can be identified for $\psi = 0$ and $\psi = 180°$; this is correct because these two azimuth angles correspond to the highest and the lowest point of the rotor, where the maximum and minimum (respectively) wind speed magnitude is detected. Besides, the fluctuations are not symmetric between the upper and the lower half-plane of the rotor (respectively, $-90° < \psi < 90°$ and $90° < \psi < 270°$); this evidence is justified by the fact that, the shear gradient experienced by the bottom half of the rotor is larger than the one experienced by the top half of the rotor plane. Finally, it can be observed that all the lines intersect the axis y=0 at $\psi = 90°$ and $\psi = 270°$, which is correct because they represent the wind speed at the hub height, which is used as a reference wind speed, and consequently no AoA fluctuations can be detected. The right-hand figure shows the range of the AoA fluctuations as a function of the radial position and it represents the maximum fluctuation that the AoA experiences over a revolution. For the WS case, the definition of range of AoA fluctuations is:

$$\Delta AoA = AoA(\psi = 0) - AoA(\psi = 180°) \tag{3.3.2}$$

This holds for all the radial positions, as can be observed in Figure 3.7a. It can be noticed that the range of AoA fluctuations increases along with the radial position. For blade root sections, the small rotational component of the relative velocity should, in principle, result in larger AoA fluctuations than for blade tip sections; although, the effect of wind shear on the axial velocity component is larger for blade tip sections than for blade root sections, because of the larger wind speed difference between the highest and the lowest point reached by the airfoil. Figure 3.7b shows that the perturbation of the axial velocity component is dominant with respect of the rotational component variation along the span, resulting in a slight increase of the range of AoA fluctuations moving towards the tip of the blade. Besides, it is possible to notice that despite the large difference between the low and high value of terrain roughness used to plot the two curves (three order of magnitude), the resulting angle of attack fluctuations are comparable in magnitude (difference lower than 1 [°]). Consequently it is possible to state that the value of terrain roughness has a restrained impact on the angle of attack fluctuations and this argument will be later used is section 3.4.

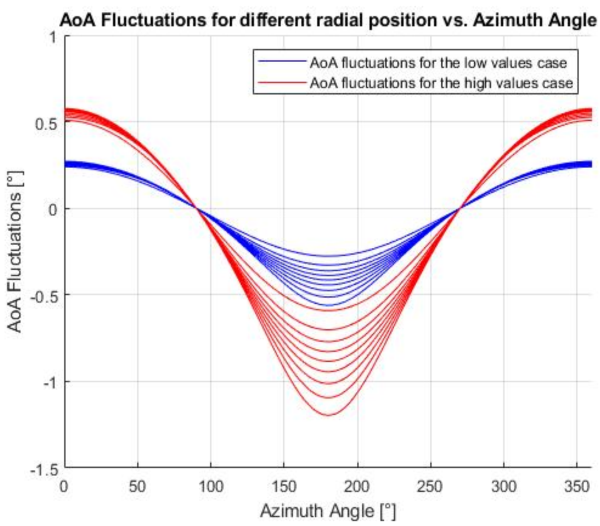

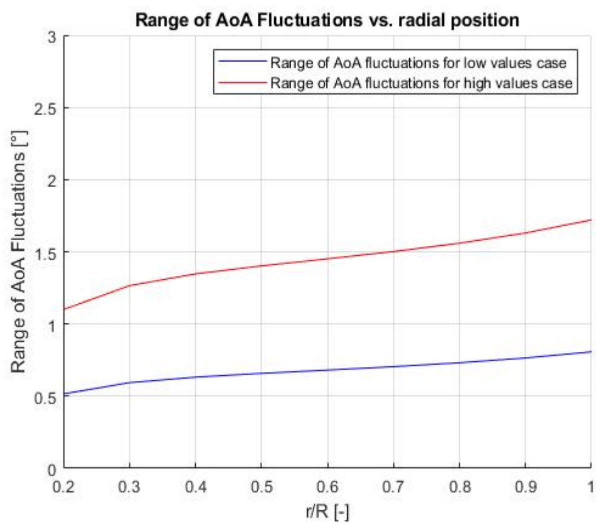

Figure 3.7: *(a) AoA Fluctuations vs ψ (b) Range of AoA Fluctuations vs radial position*

As discussed in section 2.2.6, yaw misalignment has been modelled according to the Advancing and Retreating and the Skewed Wake effect; the former effect is maximum between 0 and 180° while the latter, is maximum between 90° and 270°. Consequently, the combined contribution of these two effects is expected to be maximum and minimum (in terms of angle of attack fluctuations) between 270° and 0 and between 90° and 180°, respectively. In order to observe which of the two effects is more relevant according to the considered radial position, the azimuth angles at which the maximum and minimum magnitude of the angle of attack is reached are plotted for different blade sections, as shown in Figure

3.8b. In this figure it can be seen how, for blade root sections, the Advancing and Retreating effect has a larger influence on the AoA fluctuations, while the Skewed Wake effect becomes more and more dominant moving towards blade tip sections. This can be explained by comparing the velocity triangles for a blade root and a blade tip section; starting from the Advancing and Retreating blade effect, since no wind shear is considered in this case, the axial velocity distribution will be constant over the height, with a longitudinal component resulting from the yawed inflow ($Ucos(\beta)$). The tangential component $Usin(\beta)$ will be summed to the rotational component which is lower for a blade root section than for a tip blade section, resulting in larger AoA fluctuations for blade section with small $\frac{r}{R}$. On the other hand, by looking at equation (3.2.5), which corrects the axial induction factor distribution according to the radial position, it can be seen that the parameter K is proportional to $\frac{r}{R}$, meaning that the skewed wake effect is larger for blade tip sections. In addition, it can also be observed that the trend of the azimuth angle at which the maximum and minimum magnitude of the angle of attack is detected is non-symmetric between the left and right side of the rotor. As discussed in section 2.2.6, the fact that the wind velocity direction is yawed by an angle beta, implies that the downwind side of the rotor will experience stronger induced velocities which makes the Skewed Wake effect to be stronger for the right-hand side of the rotor, assuming a positive β.

Figure 3.8 summarizes the information about the range of AoA fluctuations experienced over a revolution; in this case the definition of maximum AoA fluctuations is the following:

$$\Delta AoA = AoA(\psi_{max}) - AoA(\psi_{min}) \tag{3.3.3}$$

Where ψ_{max} and ψ_{min} refers to Figure 3.8b. Moreover, it can be observed that the range of AoA fluctuations decreases monotonically along with the radial position. This can be again attributed to the fact that the rotational velocity component increases monotonically moving towards the blade tip, making the AoA progressively less sensible to fluctuate.

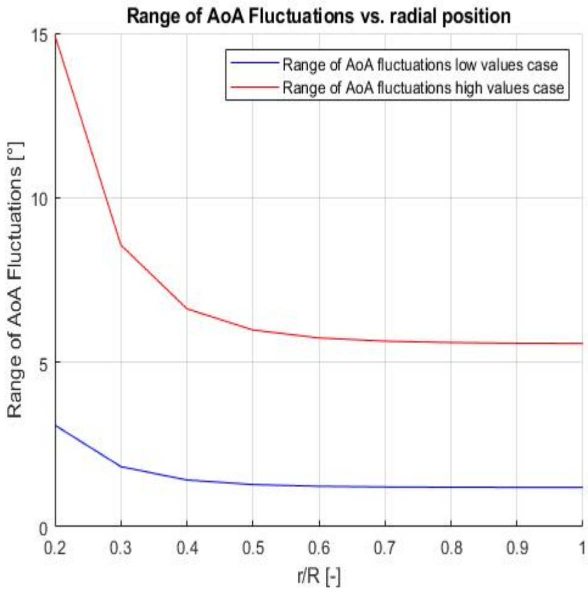

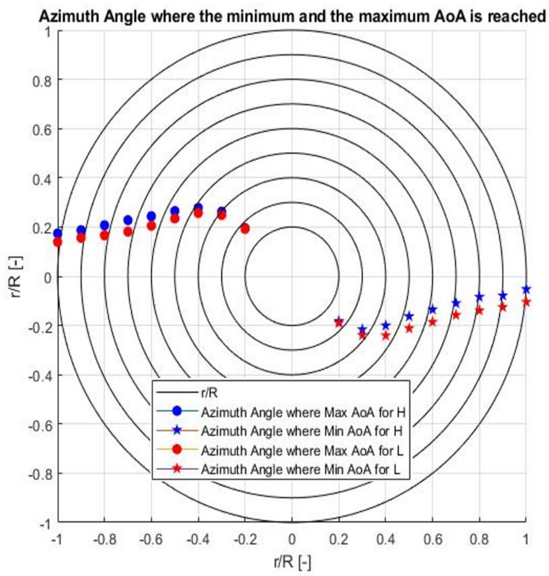

Figure 3.8: *(a) Range of AoA Fluctuations vs radial position (b) Schematic representation of the azimuth angles where the maximum and minimum AoA is detected, according to the radial position. The reference system is* $\psi = 0$ *at 12 o'clock position, moving in the clock-wise direction*

While the WS and YM effect can be addressed in a deterministic way, turbulence intensity is impossible to predict in advance, and consequently a probabilistic approach is needed. As discussed in section 2.2.4, turbulence intensity can be well approximated by a Normal (or Gaussian) probability density function, as depicted in Figure 3.9a, where the probability of a certain perturbation velocity to occur can be found. By recalling the 3-σ rule, it is possible to state that 68.27% of the data fall between the range [μ -σ, $\mu + \sigma$], which is the one shown in Figure 3.9a. As discussed for the YM case, the monotonic descending trend is justified by the smaller rotational velocity component for a blade root section with respect to the blade tip section.

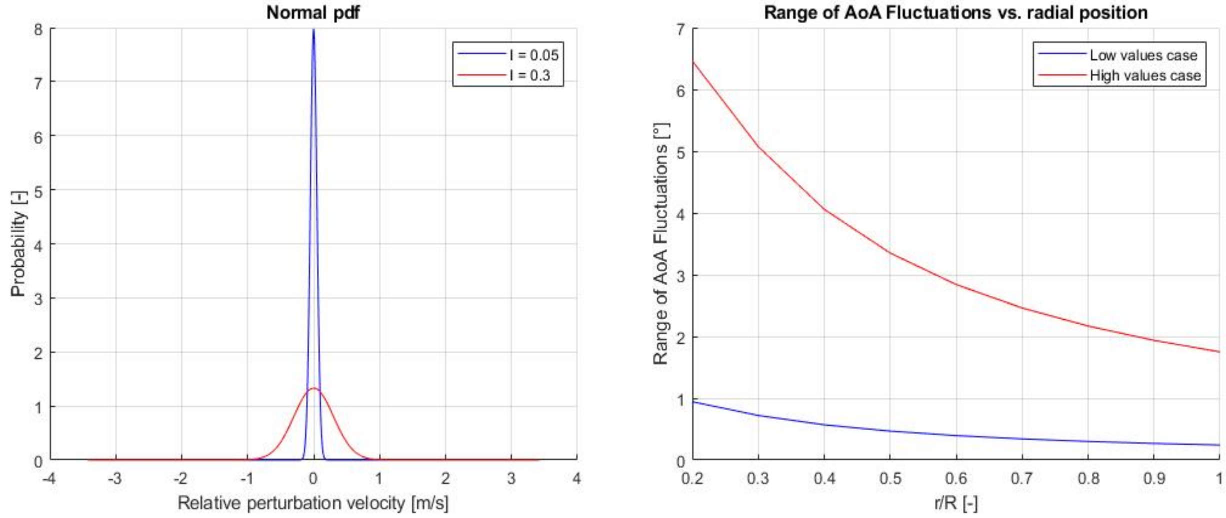

Figure 3.9: *(a) Normal pdf for the perturbation velocity δ (b) Range of AoA Fluctuations vs radial position*

3.3.2 Influence of the Combined Effect

In this section, the combined effect of the three perturbation sources discussed in section 3.3.1 will be evaluated. Figure 3.10a shows the range of angle of attack fluctuations as a function of the radial position; this range of AoA fluctuations has been obtained by taking the standard deviation of the combined probability density function (where an example of it is provided in Figure 3.10b). In contrast with the normal probability density function used for the perturbation velocity, the total pdf is not perfectly symmetric with respect of the mean, mainly because wind shear is not symmetric. In particular, it can be observed how the probability of $AoA < AoA_{design}$ to occur is slightly larger than the probability of $AoA > AoA_{design}$ to take place. This is correct, because, as can be observed in Figure 3.7a, the gradient $\frac{\partial U}{\partial y}$ is larger for the bottom half of the rotor, than for the upper half of the rotor, consequently it follows that $AoA(\psi = 90°) - AoA(\psi = 180°) > AoA(\psi = 90°) - AoA(\psi = 0)$. This said, the shape of the total pdf is very similar to a Gaussian distribution and consequently the 3-σ rule can still be used. The quasi-Gaussian shape of the combined probability density function suggests that turbulence intensity is the most relevant phenomenon in terms of AoA fluctuations, which is confirmed by the monotonically descending trend of the range of AoA fluctuations versus the span. This latter evidence confirms the fact that wind shear (whose trend is slightly ascending) plays a negligible role when all the effects are combined together.

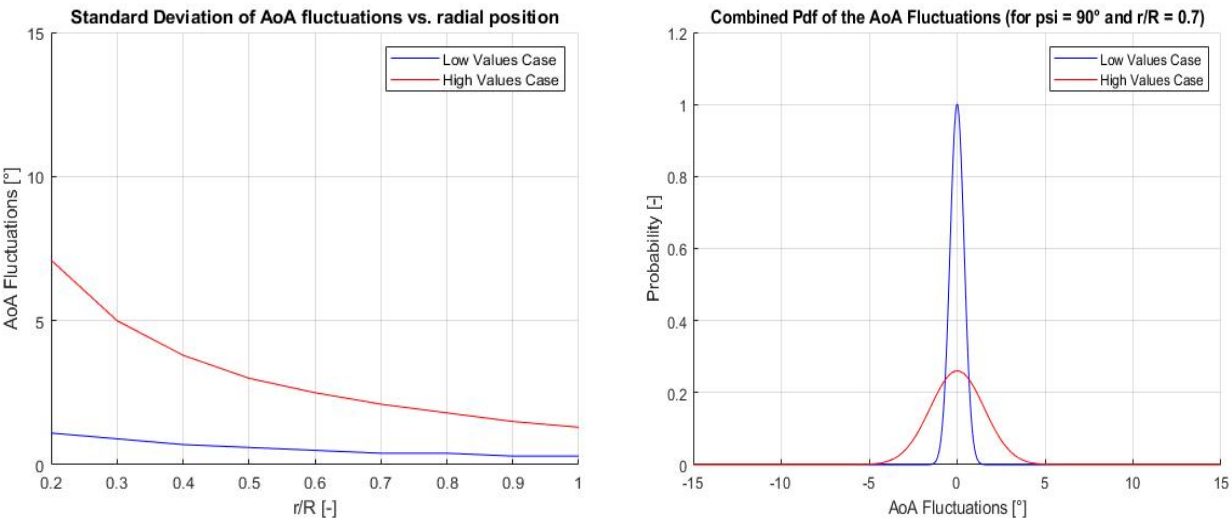

Figure 3.10: *(a) Range of AoA Fluctuations vs radial position (b) Example of the total probability density function, calculated at $\frac{r}{R} = 0.7$ and $\psi = 90°$*

3.4 Probabilistic Design Space Mapping

One of the main goals of this work is to determine the operational range in which the angle of attack is expected to fluctuate over the wind turbine's lifetime, in order to design airfoils whose performance will be optimized based on this AoA range. In the previous sections, it has been seen that the probability of angle of attack fluctuations can be considered to be dependent on five different parameters and the impact of large variations of these values has been tested. The aim of the probabilistic design space mapping is to evaluate which values of each parameter are relevant for HAWT airfoil applications and to study how the angle of attack fluctuations change when different combinations of these parameters are considered. Finally, it is also wanted to estimated how much each combination of the five parameters is likely to occur in practice. This is done in order to derive an 'operational' probability density function which is obtained as a weighted sum of the different AoA pdfs (one for each considered combination) and their weight depends on their probability of occurrence. The methodology which has been used to select the cases will be explained as follows:

- As already discussed, the chosen $\frac{r}{R}$ range is from 20 to 100 %, because structural requirements demand for airfoils with a cylindrical-like shape to withstand the loads for span fractions lower than 0.2, having really low contribution to the Lift generation and consequently to the aerodynamic performance.
- In order to cover the possible values that the TSR and β might assume, while keeping the number of variables as low as possible, three values have been considered, namely: 7, 5 and 3 and 0, 10 and 20°, respectively. The selected values for the TSR are typical of HAWT, while, the values for the yaw angle are based on Figure 3.1.
- The terrain roughness is site specific and several values can be chosen; although, recalling Figure 3.7b, the influence of the chosen values of the terrain roughness has a small impact in terms of resultant AoA fluctuations. Indeed, as it can be seen in the figure a difference of three order of magnitude in the terrain roughness results in slightly different (lower than 1 °) AoA fluctuations. For this reason, it has been chosen to consider three different sites, namely Onshore, Near-Coastal and Offshore and a fixed value of z_0 will be assigned to each of the site: 0.1, 0.005 and 0.0002 [m], respectively. These values have been obtained from the reference values expressed in Table 2.2.
- Finally, when considering turbulence intensity, it should be point out that it is either site specific and depending on the mean wind speed, and consequently on the TSR. In order to decide what values should be used for the analysis, the scaling rules prescribed by the IEC-61400 standards have been followed and a schematic representation can be observed in Figure 3.11a, 3.11b and 3.12, which show the turbulence intensity and the TSR vs. the wind speed for the three different sites, Offshore, Near-Coastal and Onshore. From these graphs, the turbulence intensity values associated with each TSR range (e.g. between 6 and 7) can be derived for each case.

A summary of all the analyzed cases can be found in Table 3.3. 18 cases have been studied for the Offshore and Near-Coastal sites while 33 for the Onshore one; the reason for this is that, as it can be seen by comparing Figure 3.11 and 3.12, the range of possible values of turbulence intensity is larger for an Onshore location, and consequently more values of I should be considered.

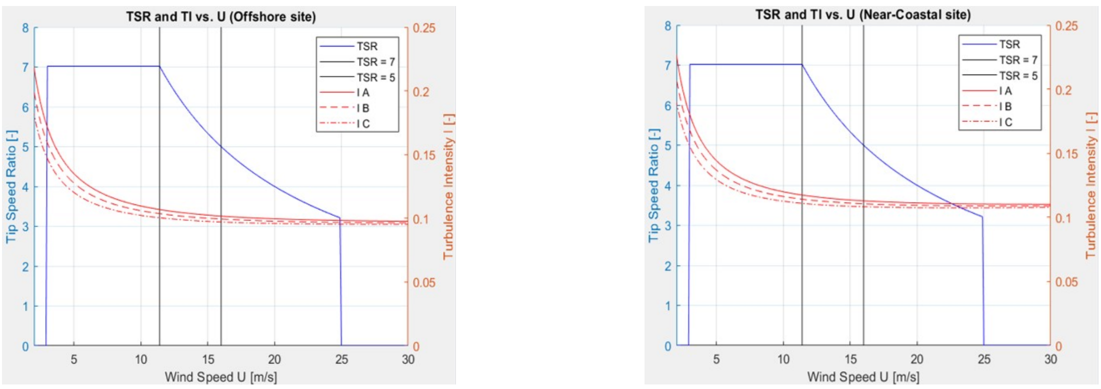

Figure 3.11: *Tip Speed Ratio and Turbulence Intensity vs. Wind Speed for an Offshore (a) and a Near-Coastal (b) site.*

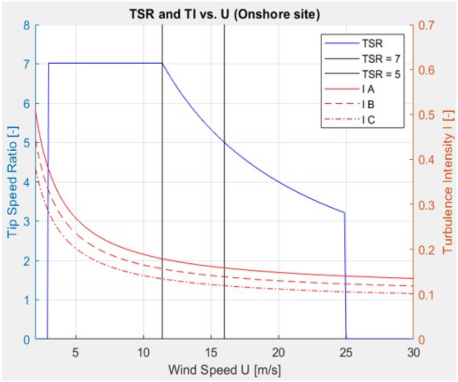

Figure 3.12: *Tip Speed Ratio and Turbulence Intensity vs. Wind Speed for an Onshore site.*

Once the pdf of the angle of attack fluctuations has been computed for each case, a set of weighting coefficients can be derived and normalized for their total sum to be 1. Consequently, the probability of angle of attack to occur for each case is multiplied by the correspondent weighting coefficient. Finally, by summing up the resultant values, the final probability density function which weights the contribution of each case based on their probability of occurrence can be obtained, as shown below:

$$\sum_{i=1}^{n_{cases}} p(\alpha)_{case_i} \times w_{case_i} \tag{3.4.1}$$

Where $p(\alpha)_{case}$ is the probability of occurrence of the AoA (at a given blade section) for each case and w_{case} is the weighting coefficient assigned to each case. The procedure through which the weighting coefficient for each case is calculated is explained as follows. Since the probabilistic design space mapping has been carried out by differentiating from three different site conditions (Onshore, Near-Coastal and Offshore) and a fixed value of terrain roughness has been used for each site, the probability of terrain roughness to be the selected value is 100 % for each site and a similar reasoning goes for the considered blade fraction $\frac{r}{R}$. A different approach should be performed when considering the probability of occurrence of TSR, turbulence intensity and yaw misalignment. The tip speed ratio and the turbulence intensity are not independent of each other, because they both depend on the mean wind speed. Consequently, the joint probability must be calculated. As discussed in section 3.1.1, the joint probability of TSR and TI to occur simultaneously can be obtained by multiplying the conditional probability of turbulence intensity given the mean wind speed by the probability of occurrence of the mean wind speed itself (see also section 3.1.4). Once the joint probability of TSR and I to occur simultaneously has been computed, the final probability is given by multiplying it by the probability of occurrence of yaw misalignment, which has been considered to be independent of the mean wind speed.

$$w_{case} = p(\beta) \times \sum_{i=U_1}^{U_2} [\; p(I|U_i) \times p(U_i) \;] \tag{3.4.2}$$

Where U_1 and U_2 are the lower and upper wind speed limit for the considered TSR. This procedure has been performed for the Offshore and Onshore scenarios, while the results for the Near-Coastal site will not be shown as they can considered to be in between the Onshore and the Offshore sites. An example of the final probability density function for the both the onshore and the offshore installation sites is presented in Figure 3.13, assuming an optimal angle of attack of 5 ° and a span fraction of 50%. As expected, the larger average turbulence values for the onshore scenario will make the expected fluctuations of the AoA to be larger than for the Offshore scenario.

Figures 3.14a and 3.14b show a comparison between the average AoA fluctuations for each case and the probability of occurrence of each case, for an offshore and an onshore site respectively. The term average is referred to a [0 360°[azimuthal average of the angle of attack fluctuations which has been subsequently averaged over the blade span. Referring to the legend, 'total' shows an average of the angle of attack fluctuations over the span-fraction range [0.2 1], 'inboard' over [0.2 0.4] and 'outboard' over]0.4 1]. It can be clearly see how an increase in the turbulence intensity values results in an increase in the angle of attack fluctuations and besides, fluctuations are always larger for inboards than for outboard stations. No larger variations in the AoA fluctuations are detected when increasing the

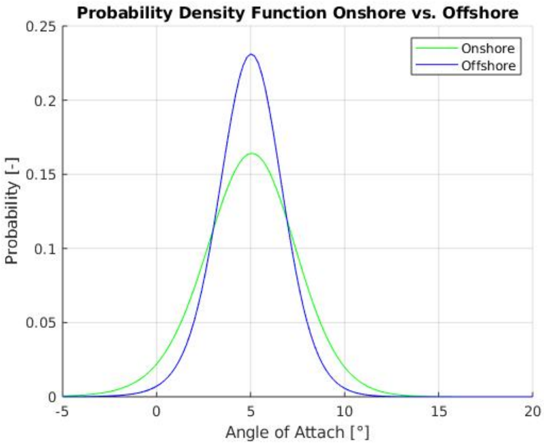

Figure 3.13: *Probability density function for the Onshore and the Offshore scenario assuming an optimal AoA of 5° and a blade section at 50% of the span*

yaw angle or decreasing the TSR, stressing out that turbulence plays the major role when all effects are combined. Finally, it can be again showed that on average, an Onshore site presents a larger average angle of attack fluctuations than an Offshore site.

As far as the probability of occurrence of each case is concerned, the first clear trend can be observed in terms of yaw misalignment angle, indeed, the probability of occurrence decreases when the yaw misalignment increases, reaching values roughly equal to zero for large β (e.g. 20 °). It can also be noted that the largest probability of occurrence, for both offshore and onshore, is found for $4 < TSR < 6$ and low values of turbulence intensity. This evidence might appear surprising, because the probability of occurrence of low TSR is lower than large TSR (according to the Weibull pdf); however, this fact can be explained by looking at the conditional probability of turbulence intensity to occur given the wind speed (Figure 3.2). It can be seen that the mean and standard deviation of the probability density function decreases as the wind speed increases. Consequently the joint probability of occurrence of a low turbulence intensity and moderate TSR is large and it explains the peaks in the graph. Moreover, for the onshore scenario, the probability of occurrence of cases with low values of turbulence intensity is larger than for cases with large I (e.g. from case 1 to 5). The conditional probability for I to occur given U is based on a near-coastal site (because no data could be found for an onshore site) where lower values of I are expected. Consequently, it can be concluded that the choice of using a conditional probability based on near-coastal site has negatively influenced the weight of each Onshore case.

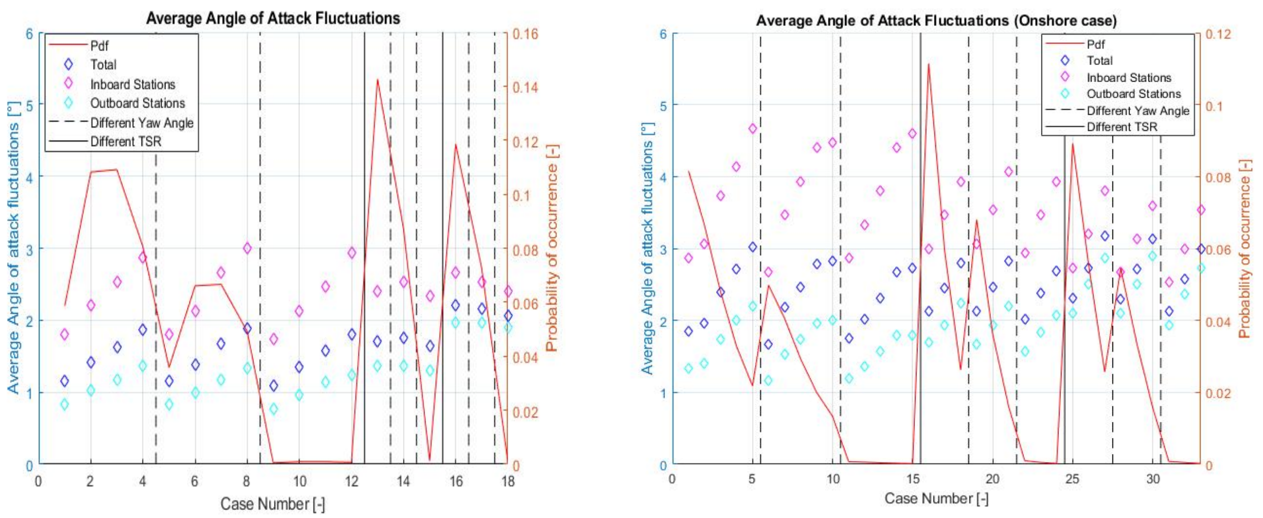

Figure 3.14: *Average angle of attack fluctuations versus probability of occurrence of each case for an (a) offshore and (b) onshore site.*

-	Onshore	Near-Coastal	Offshore
Case n°	TSR [-], I [-], β[°]	TSR [-], I [-], β[°]	TSR [-], I [-], β[°]
1	7, 0.150, 0	7, 0.12, 0	7, 0.10, 0
2	7, 0.175, 0	7, 0.14, 0	7, 0.12, 0
3	7, 0.200, 0	7, 0.16, 0	7, 0.14, 0
4	7, 0.225, 0	7, 0.18, 0	7, 0.16, 0
5	7, 0.250, 0	7, 0.12, 10	7, 0.10, 10
6	7, 0.150, 10	7, 0.14, 10	7, 0.12, 10
7	7, 0.175, 10	7, 0.16, 10	7, 0.14, 10
8	7, 0.200, 10	7, 0.18, 10	7, 0.16, 10
9	7, 0.225, 10	7, 0.12, 20	7, 0.10, 20
10	7, 0.250, 10	7, 0.14, 20	7, 0.12, 20
11	7, 0.150, 20	7, 0.16, 20	7, 0.14, 20
12	7, 0.175, 20	7, 0.18, 20	7, 0.16, 20
13	7, 0.200, 20	5, 0.12, 0	5, 0.10, 0
14	7, 0.225, 20	5, 0.12, 10	5, 0.10, 10
15	7, 0.250, 20	5, 0.12, 20	5, 0.10, 20
16	5, 0.120, 0	3, 0.12, 0	3, 0.10, 0
17	5, 0.140, 0	3, 0.12, 10	3, 0.10, 10
18	5, 0.160, 0	3, 0.12, 20	3, 0.10, 20
19	5, 0.120, 10	-	-
20	5, 0.140, 10	-	-
21	5, 0.160, 10	-	-
22	5, 0.120, 20	-	-
23	5, 0.140, 20	-	-
24	5, 0.160, 20	-	-
25	3, 0.100, 0	-	-
26	3, 0.120, 0	-	-
27	3, 0.140, 0	-	-
28	3, 0.120, 10	-	-
29	3, 0.140, 10	-	-
30	3, 0.160, 10	-	-
31	3, 0.120, 20	-	-
32	3, 0.140, 20	-	-
33	3, 0.160, 20	-	-

Table 3.3: *Summary of the values used for the analysis for each simulated case, recalling that the* $\frac{r}{R}$ *ranges from 0.2 to 1 [-] and the terrain roughness values are 0.1, 0.005 and 0.0002 [m] for Onshore, Near-Coastal and Offshore, respectively*

Chapter 4

Verification Approach through Aeroelastic Simulation

This chapter aims to verify the presented model using an aeroelastic simulator, which will be discussed in section 4.1. It should be pointed out that in this work, the term verification will be used with the same meaning of validation. Since, as it has been seen in the probabilistic design space mapping it is wanted to evaluated the probabilistic approach predictions for different wind conditions, it is hard to find real data which allows a one-to-one comparison between the selected values for the analysis and the values from real data. For this reason, it has been decided to use FAST a 'validation' tool.

The verification procedure is organized as follows: first the model of each perturbation source will be verified singularly for wind speeds ranging from 5 to 17 $[\frac{m}{s}]$ in steps of 4 $[\frac{m}{s}]$; the simulations will be run for low and high values, similarly to section 3.3. This is done in order to have a comprehensive view of how well the model is able to estimate the fluctuations of the angle of attack for what are considered large and low values of the considered atmospheric non uniform parameters. This will be shown in section 4.3, 4.4 and 4.5. Subsequently, the model which combines the effect of all the three perturbation sources will be tested and results will be shown in section 4.6.

4.1 Verification Tool: FAST

This section aims to introduce the FAST code used to perform the verification of the proposed method; more detailed information can be found in [43]. The Fatigue, Aerodynamics, Structure and Turbulence (FAST) code is an aeroelastic simulator able to either predict the extreme or the fatigue load for a three-bladed (or two-bladed) HAWT; FAST has been acknowledged to be suitable for calculation of onshore wind turbine loads for design and certification according to the Germanischer Lloyid WindEnergie [44]. The code includes an aeroacustic noise prediction algorithm, as well as lateral offset and skew angle of the rotor shaft, rotor-furling, tail-furling, tail inertia and aerodynamics, yaw control and high-speed shaft (HSS) brake control.

FAST models a three-bladed HAWT with 24 Degrees of Freedom (DoFs). The translational (namely: surge, sway and heave) and rotational (namely: roll, pitch and yaw) motion of the support platform, with respect of the inertia frame, constitute the first six DoFs. Four DoFs describe the tower motion, in particular two for the longitudinal modes and two for the lateral modes. In order to include the variable rotor speed shaft and the drive-shaft flexibility, the generator azimuth angle and the compliance of the drive train (between the generator and the hub/rotor) are also considered as DoFs. Three DoFs describe the flapwise tip motion of the blade while three DoFs provide the tip displacement for each blade for the second flapwise mode and other three the tip displacement for the first edgewise mode. Finally, rotor-furl and tail-furl are the last two DoFs.

FAST uses two different flapwise mode and an edgewise mode to describe the motion of the flexible blades. Besides, the blade is twisted, meaning that the blade tip will not deflect in one single plane, but the total displacement will be given by the sum of the contribution of the deflection in the in-plane and in the out-of-plane direction.

As discussed in [45], the models used to represent the effect of the dynamic phenomena, namely:

dynamic stall and dynamic inflow, refers to the works of Beddoes-Leishman [46] and Pitt-Peters [48], respectively; these models will be addressed in section 4.1.1. Moreover, the stuctural behavior of the wind turbine blades is modelled according to the Euler-Bernoulli beam as in [50], which will be discussed in section 4.1.2.

4.1.1 Aerodynamic Modelling

This section will describe how the dynamic stall and the dynamic inflow processes have been modelled in FAST. The BEM theory is a static model, which assumes that the aerodynamic forces on each blade are balanced at any time by the structural forces and that the acceleration of the flow, subsequent to a variation in the loading, is instantaneous [48]. The BEM model assumes that the induced velocity distribution is uniform over the wind turbine rotor; in order to account for the variation of the induced velocity across the rotor, the dynamic inflow model is necessary. The first version of the model has been proposed by Pitt and Peters [49], where the velocity distribution variation over the rotor has been modelled according to three terms, which respectively represent the mean value of the induced velocity, the side-to-side variation of the induced velocity (subscript s) and the top-to-bottom variation of the induced velocity distribution (subscript c). Consequently, the induced velocity can be described by the following expression [48]:

$$\omega(r,\psi) = \lambda_0 + \lambda_s \frac{r}{R} sin(\psi) + \lambda_c \frac{r}{R} cos(\psi) \tag{4.1.1}$$

Where the reference system used in this expression is $\psi = 0$ at the six o'clock position, meaning blade pointing down. From this expression it can be noticed that, whether the distribution parameters λ_s and λ_c are 0, the induced velocity is uniformly distributed across the wind turbine rotor. The governing equations relate the induced velocity distribution parameters to the variation of the aerodynamic loads, using a linear relationship in the matrix form [48]. One of the main problem of this model, addressed by Suzuki and Hansen in [48], is that the aerodynamic loads have peaks at the blades, because it is where the aerodynamic forces are exerted. Moreover, the Pitt and Peters model refers to the 1P loads, which are not the only frequencies important in nowadays wind turbine rotor, which are usually three-bladed; in three-bladed rotor wind turbines, the 3P loads are crucial and they must be accounted for in the model. Consequently, higher order of the governing functions are needed in order to more accurately represent 0P, 1P, 2P and 3P loads; however, for a three-bladed wind turbine, the 2P loads contribution is rather small and can be neglected [48]. The generalized dynamic wake model with higher order functions has been derived assuming that the pressure distribution across the rotor plane satisfy the Laplace equation. The variation of the pressure distribution has been modelled by using infinite series of Legendre functions along the radial direction while infinite series of trigonometric functions to express the pressure distribution variation as a function of the azimuthal position. The superscript m denotes the period of the loading the rotor is subject to, meaning that $m = 1$ is related to the 1P load period and n is the current sample. The trigonometric functions are represented by the inflow expansion coefficients α_n^m and β_n^m, related respectively to the $cos(m\psi)$ and $sin(m\psi)$, which indicates the m-P azimuthal induced velocity distribution and the n^{th} radial distribution mode. The expression for the generalized dynamic wake model, which can be considered to be equivalent of equation 4.1.1 can be found in [48] as well as a more detailed definition of the Legendre and trigonometric functions used in the model. The governing equations can now be written as in [48], under the assumptions that the sinus and cosinus terms are independent:

$$[M] \begin{bmatrix} \cdot \\ \cdot \\ \cdot \\ \{\alpha_n^m\} \\ \cdot \\ \cdot \\ \cdot \end{bmatrix}^* + [V]\,[L^c]^{-1} \begin{bmatrix} \cdot \\ \cdot \\ \cdot \\ \{\alpha_n^m\} \\ \cdot \\ \cdot \\ \cdot \end{bmatrix} = \frac{1}{2} \begin{bmatrix} \cdot \\ \cdot \\ \cdot \\ \{\tau_n^{mc}\} \\ \cdot \\ \cdot \\ \cdot \end{bmatrix} \tag{4.1.2}$$

$$[M] \begin{bmatrix} \cdot \\ \cdot \\ \cdot \\ \{\beta_n^m\} \\ \cdot \\ \cdot \\ \cdot \end{bmatrix}^* + [V]\,[L^s]^{-1} \begin{bmatrix} \cdot \\ \cdot \\ \cdot \\ \{\beta_n^m\} \\ \cdot \\ \cdot \\ \cdot \end{bmatrix} = \frac{1}{2} \begin{bmatrix} \cdot \\ \cdot \\ \cdot \\ \{\tau_n^{ms}\} \\ \cdot \\ \cdot \\ \cdot \end{bmatrix} \tag{4.1.3}$$

Where [M] is the apparent mass matrix, [V] is the flow parameters matrix, [L] is the inflow gain matrix, [ ]* indicates the first derivative with respect to the non-dimensional time and τ_n^{ms} is the pressure coefficient [48].

As already discussed in section 2.3, if the design AoA is substantially exceeded, the airfoil experiences dynamic stall; in order for the dynamic stall process to be accurately modelled, important characteristics should be highlighted. The model must be able to describe the attached flow behavior as well as the leading and trailing edge separation. The attached flow behavior representation has been addressed by using the superposition principle on the circulatory and non-circulatory indicial aerodynamic responses, relating the variation in the normal force to a step change in the AoA. In particular, the non-circulatory part refers to the static situation, which is adjusted by the circulatory contribution, used to represent the dynamic nature of the phenomenon. It follows that [46]:

$$C_N^P = C_{N_n}^C + C_{N_n}^l \tag{4.1.4}$$

The circulatory normal forces include deficiency functions, which tells by how much the unsteady aerodynamics effects make the AoA be different from the quasi-steady case and it contains information about the history of the AoA. Hence, it basically tells how much the AoA is varying according to the distance covered by the semi-chord due to unsteady aerodynamics effects. The deficiency function of the non-circulatory normal forces accounts for the concentration of wake pressure disturbances, as well as the history of the AoA.

After the vortex disturbance builds up in the LE region, the following step in the dynamic stall process is the LE separation, and it is crucial to determine where the separation point would occur. Since the normal force C_N and the LE pressure depend on each other, it is possible to derive a critical value that represents the critical pressure at which leading edge separation starts taking place, and it corresponds to the $C_N(static)$. In unsteady condition, there is a time delay between the load $C_N(t)$ and the response of the LE pressure; this means that if the AoA increases, since the LE pressure response is not instantaneous, the critical pressure point would be reached for higher values of the AoA, with respect of what could have been obtained for the quasi-steady case. The larger the AoA at which the critical pressure point is reached the larger the time delay between excitation and response. As performed for the attached behavior case, the time delay can be introduced by using a deficiency function, in such a way that the normal aerodynamic force can be written as:

$$C_N' = C_{N,n} - D_{p,n} \tag{4.1.5}$$

This can be done under the assumptions that all the properties which apply to C_N are also valid for C_N'. Having defined dynamic normal aerodynamic force, it can be stated that LE separation will occur when $C_N' > C_N(static)$. The LE separation is also related to the level of turbulence in the flow, which can be accounted for by using the reduced frequency; the more turbulent the flow is the later the LE separation would occur, shifting to higher values of AoA with respect to the quasi-steady case and consequently increasing the time delay [46].

When the vortex disturbance reaches the TE region it is shed into the wake and for this reason it is fundamental for the model to be representative of the TE separation as well. It is important to highlight that, when TE separation occurs, the relationship that expresses the force and moment response are no longer linear. The normal aerodynamic force, which includes the effects of compressibility, can be expressed as follows [46]:

$$C_N = C_{N_\alpha}\left(\frac{1+\sqrt{f}}{2}\right)^2 \alpha \tag{4.1.6}$$

Where the term C_{N_α} represents the slope of the force curve at a specific Mach number and f is the TE separation point. In unsteady conditions, the TE edge separation point location will differ from the steady one, because of a time-lag between the variation in the airfoil pressure distribution and the boundary layer response. First of all, the effective angle of attack can be defined as [46]:

$$\alpha_f(t) = \frac{C_N'(t)}{C_{N_\alpha}(Ma)} \tag{4.1.7}$$

The effective AoA is used to determine, in first instance, the effective separation point f', which corresponds to α_f and this can be obtained by plotting the static separation point f as a function of the AoA. Subsequently, the time delay of the response is included, again, using a deficiency function;

by doing this, the unsteady separation point at the TE (f") can be derived and fed into the expression for the aerodynamic forces, resulting in [46]:

$$C_N^f = C_{N_\alpha}(Ma)\left(\frac{1+\sqrt{f_n''}}{2}\right)^2 \alpha_{E_n} + C'_{N_m} \tag{4.1.8}$$

Finally the dynamic stall model can be described. Recalling the stall mechanism discussed in section 2.3, it has been observed that, substantial variation in the pressure and force distribution across the airfoil occurs only when the vortices separate. In particular, the contribution to the Lift of the vortices can be modelled by an accumulation of circulation in the proximity of the airfoil. In particular, by computing the difference between the unsteady linear and non-linear circulatory Lift, also known as Kirchhoff approximation as in [46]:

$$C_{v_n} = C_{N_n}^C(1-K_{N_n}); \qquad where \quad K_{N_n} = \frac{1}{4}(1+\sqrt{f_n''})^2 \tag{4.1.9}$$

it is possible to derive the total accumulated vortex Lift $C_{N_n}^v$, which is assumed to exponentially decrease over time and it is also a function of the previous increment (e.g. value at n-1 if the current sample is n), as [46]:

$$C_{N_n}^v = C_{N_{n-1}}^v e^{\left(\frac{\Delta S}{T_v}\right)} + (C_{v_n} - C_{v_{n-1}})e^{\left(\frac{\Delta S}{2T_v}\right)} \tag{4.1.10}$$

It must be pointed out that, for the special case where the rate of change of the vortex Lift approaches zero, it follows that the rate of accumulation coincides with the rate of dissipation; namely, it reduces to the static non-linear behavior. In addition, since the role of the vortices in the circulation accumulation depends on the position of the vortex over the airfoil chord, it is possible to use a non-dimensional parameter (T_V, expressed in semi-chords) which is considered to be 0 at the separation point and equal to a certain value (T_{vl}) at the TE; the non-dimensional parameter should be computed empirically by actual data. The total normal force coefficient in stall condition $C_N(t)$ is expressed as:

$$C_N(t) = C_N^f(t) + C_N^v(t) \tag{4.1.11}$$

Finally, in order to account for the secondary increment in the vortex Lift, which mainly arises at high incidence range, the non-dimensional parameter T_{vl} is substituted by T_{st}; This can be explained by the fact that the vortex shedding frequency can be approximated by the Strouhal number (St), roughly equal to 0.19. The expression for T_{st} is given in [46]:

$$T_{st} = \frac{2(1-f'')}{St} \tag{4.1.12}$$

4.1.2 Structural Modelling

This section will describe the Euler-Bernoulli beam model, used to calculate the stresses, the internal moments or the deformation a beam can be subject to. Since the wind turbine blades can be assumed to be cantilever flexible beams, under the assumption that the length of the object is significantly larger than the cross-sectional area, the Euler-Bernoulli model can be applied. The model is mainly based on three assumptions which will be listed below, according to [50]:

- The cross-sections of the object are always assumed to be normal to the neutral axis, either after deformation has occurred;
- Deformations are assumed to be small;
- The beam is considered to be linear, elastic and isotropic and besides, Poisson's ratio is neglected.

The first assumption helps understanding how the beam would look like after the deformation, indeed, it is known that each cross-section will stay perpendicular to the neutral axis. The reference system is X_1 along the neutral axis, X_2 along the height of the beam and X_3 along the width of the beam. After the deformation, the neutral axis will no longer coincide with the X_1 axis, and the distance between these two lines is the displacement y, which is a function of X_1. After the deformation, the neutral axis will have a certain slope, which can be associated to an angle θ. It is possible to define a vector which represents the beam before (X) and after (x) the deformation, as:

$$X = \begin{bmatrix} X_1^P \\ X_2^P \\ X_3^P \end{bmatrix}; \qquad x = \begin{bmatrix} X_1^P - X_2^P sin(\theta) \\ y + X_2^P cos(\theta) \\ X_3^P \end{bmatrix} \tag{4.1.13}$$

Consequently, the position of the displacement can be found by the difference between the vectors after and before deformation has occurred, resulting in:

$$\delta = x - X = \begin{bmatrix} -X_2^P sin(\theta) \\ y + X_2^P (cos(\theta) - 1) \\ 0 \end{bmatrix} \tag{4.1.14}$$

In order to eliminate the dependency on the trigonometric functions, the second assumptions is useful; indeed, by assuming small deformation, the vector δ will result in:

$$\delta = \begin{bmatrix} -X_2 \frac{dy}{dX_1} \\ y \\ 0 \end{bmatrix} \quad \rightarrow \quad \nabla\delta = \begin{bmatrix} -X_2 \frac{d^2y}{dX_1^2} & -\frac{dy}{dX_1} & 0 \\ \frac{dy}{dX_1} & 0 & 0 \\ 0 & 0 & 0 \end{bmatrix} \tag{4.1.15}$$

By recalling the definition of the strain matrix $\epsilon = \nabla\delta + \nabla\delta^T$, it follows that:

$$\epsilon = \begin{bmatrix} -X_2 \frac{d^2y}{dX_1^2} & 0 & 0 \\ 0 & 0 & 0 \\ 0 & 0 & 0 \end{bmatrix} \tag{4.1.16}$$

It can be noticed how the only non-zero term is ϵ_{11}, which is linearly dependent of X_2. By using the third assumption it is possible to relate the strain to the stress, by the relationship $\sigma = E\epsilon$, it follows that $\sigma_{11} = -EX_2 \frac{d^2y}{dX_1^2}$, where E is the modulus of Young. From this result, it can be said that the upper part of the beam would experience a compression, while, on the other hand, there will be tension on the bottom. For structural analysis purposes, it is convenient to express the stresses on the beam in terms of internal forces acting on the cross sectional area of the beam. The moment is defined as [50]:

$$M = EI \frac{d^2y}{dX_1^2} \tag{4.1.17}$$

Where I is the moment of inertia of the cross sectional area, defined as $I = -\frac{MX_2}{\sigma}$. The equilibrium equations can be found by assuming a distributed load (q) acting on the top surface of the beam, and subsequently isolating an infinitesimal cross section of the beam in order to study the forces and moments it is subject to. It can be found that:

$$q = \frac{dV}{dX_1}; \qquad V = \frac{dM}{dX_1} \tag{4.1.18}$$

Where V is the shear force. By combining equation (4.1.17) and (4.1.18), the solution for the displacement of a static Euler-Bernoulli Beam can be found as [50]:

$$EI \frac{d^4y}{dX_1^4} = q(x) \tag{4.1.19}$$

It can be seen that the distributed load is only dependent of the displacement. In particular, given the fourth order of the derivative, in order to solve the problem, four boundary conditions must be applied.

The static Euler Bernoulli Beam theory can be expanded into a dynamic beam equation by including the time dependent inertial forces and by considering a load which also varies in time. The inertial forces can be expressed as $\overline{m}\frac{\partial^2 y}{\partial t^2}$ and consequently, the dynamic Euler-Bernoulli Beam expression becomes [59]:

$$EI \frac{\partial^4 y}{X_1^2} + \overline{m} \frac{\partial^2 y}{\partial t^2} = q(x, t) \tag{4.1.20}$$

where $\overline{m}$ is the mass per unit of length.

4.2 Validation Set-Up

In order to show a better comparison between the results from the analytical model and the results of the numerical model, the pre-cone and tilt angle have been set to zero in FAST, following the analytical model's assumptions. In addition, all the simulations have been run according to the following settings: the BEM theory has been used as a Wake/Induction model, the Beddoes-Leishman (with the Minemma/Pierce variant) as blade airfoil aerodynamics model and the Pitt-Peters model as skewed-wake correction model. The tower shadow effect has been excluded from the analysis, while Prandtl's tip and hub losses, tangential induction calculations have been included, as well as drag term in the tangential and axial induction calculations. Finally, the Kaimal turbulence model has been used.

4.3 Wind Shear Verification

The default script for running the simulation in sheared conditions is conceived for the power law; by simply substituting the term 'PLexp' with 'Z0' in the 'InflowWind.m' file, the logarithmic law can be used as model to simulate the wind shear. In addition, the simulation has been run with steady uniform wind as wind type, to not include the effect of turbulence.

The results of the validation will be presented in two different forms: the left-hand figure will show the standard deviation of the AoA fluctuations while, in the right-hand figure, the range of angle of attack fluctuations over a revolution (whose definition has been given in section 3.3.1) will be illustrated. Consequently, the left-hand graph will provide the information of the AoA fluctuations which occur for about 68% of the time, while the right-hand graph expresses the maximum difference, in AoA, experienced over a revolution.

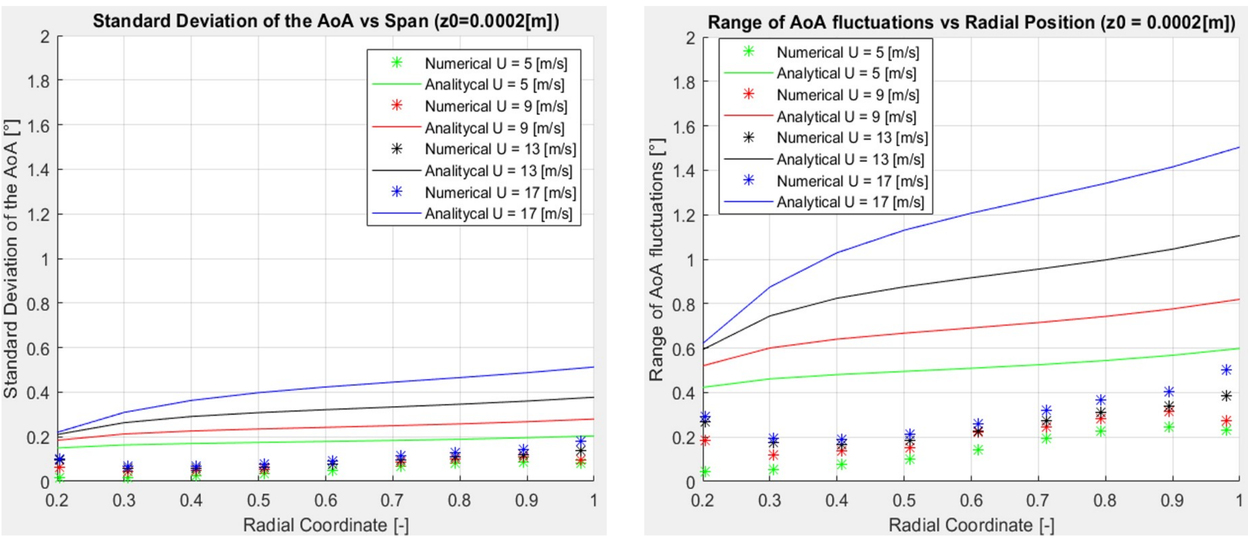

Figure 4.1: *(a) Standard Deviation of the AoA fluctuations vs. span (b) Range of AoA fluctuations vs. span, for* $z_0 = 0.0002[m]$*, comparison between analytical (solid lines) and numerical (stars) results.*

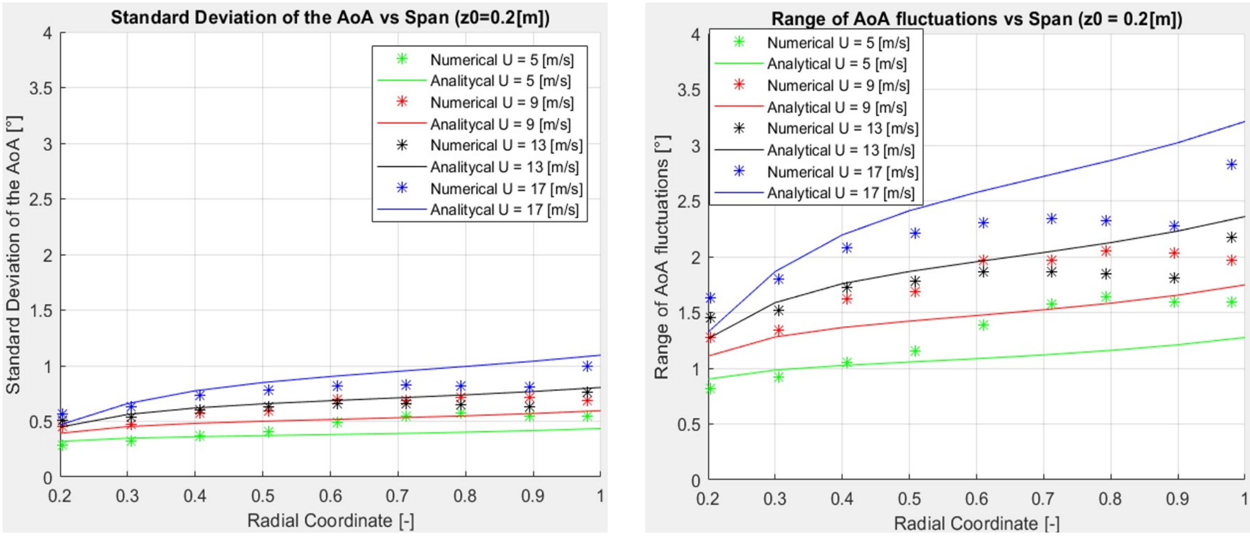

Figure 4.2: *(a) Standard Deviation of the AoA fluctuations vs. span (b) Range of AoA fluctuations vs. span, for* $z_0 = 0.2[m]$*, comparison between analytical (solid lines) and numerical (stars) results.*

By looking at Figure 4.1 it can be observed how the model is able to follow the trend of the AoA fluctuations, either with respect of the span, because both analytical and numerical results show an increasing trend moving from inboard towards outboard stations, and with respect of the wind speed. The magnitude of the numerical and analytical results is comparable and it can be observed how the model slightly overestimates the AoA fluctuations. Similar findings can be noticed in Figure 4.2, where the terrain roughness value has been increased to $z_0 = 0.2[m]$. In this case, the model proves to be more accurate than for the previous case, resulting in a better match in terms of magnitude, between analytical and numerical results.

The analytical model requires the axial induction factor as input for the calculation of the AoA fluctuations. The axial induction factor has been estimated starting from the power curve definition and by using the expression which relates the power coefficient with the induction factor, meaning $c_p = 4a(1-a)^2$. By comparing the estimated a with the axial induction factor which results from the time series of the simulation, it has been noticed that the analytical axial induction factor results in a lower value than the numerical one. A smaller induction factor will make the longitudinal component of the relative wind speed to be larger than in the numerical case. A larger longitudinal component, while keeping the tangential component fixed, will result in larger AoA fluctuations. For this reason, the influence of the choice of the induction factor on the AoA fluctuations has been tested, by using the numerical induction factor (from FAST), rather the the analytical one, in the analytical model. These outputs are shown in Figure 4.3. It can be noticed that, for $z_0 = 0.0002[m]$, where the model always overestimates the AoA fluctuations, the use of the numerical induction factor will lead to a better match of the results. Though, for $z_0 = 0.2[m]$, the choice of the numerical a proves to be beneficial only for above rated wind speeds, while the results get worst for below rated wind speeds. By considering that the influence of the axial induction factor is small and that the use of the numerical induction factor does not always improve the match between the analytical model results and the simulation results, it can be concluded that the estimation of a as discussed above is sufficiently good for the AoA fluctuations estimation. Finally, the role of the unsteady effects when only wind shear is considered is negligible, which justifies the assumption of steady aerodynamics done in the model (not shown here). The small mismatch between numerical and analytical results can therefore be attributed to the fact that the model neglects the structural response of the blades, which is taken into account in the FAST simulation.

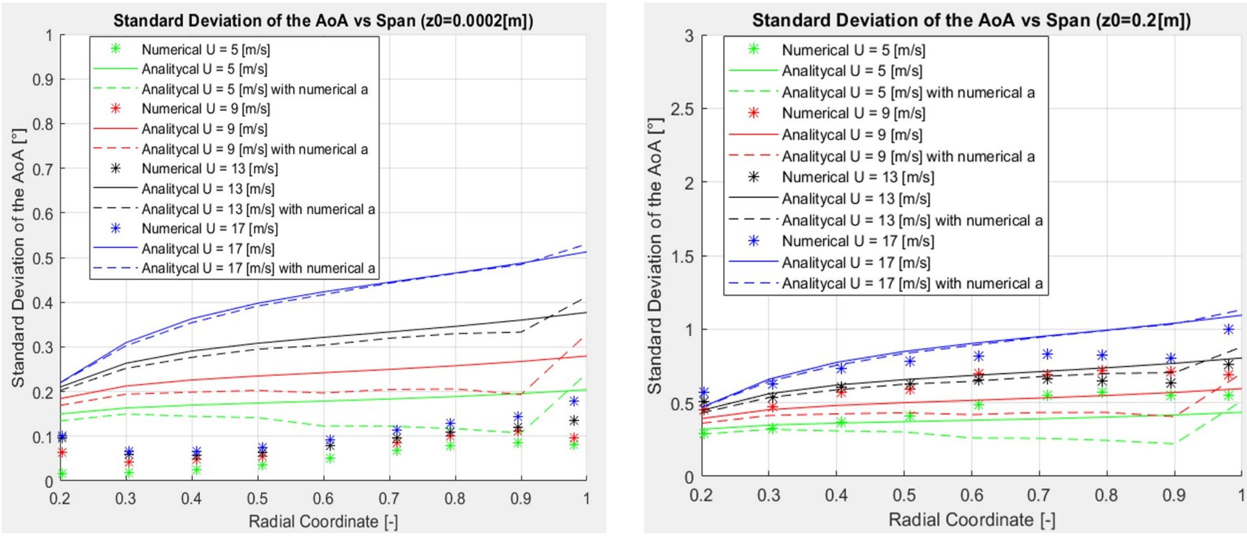

Figure 4.3: *(a) Standard Deviation of the AoA fluctuations vs. span (b) Range of AoA fluctuations vs. span, for $z_0 = 0.2[m]$, comparison between analytical (solid lines), numerical (stars) and analytical with numerical a (dashed lines) results.*

4.4 Yaw Misalignment Verification

In order to simulate yawed conditions, two options are possible in FAST, both generating the same outputs. The first option is changing the parameter 'PropagationDir' in the 'InflowWind.m' file, the second would be to set the 'YawDOF = FALSE' and changing the parameter 'NacYaw' in the 'ElastoDyn.m' file. It must be pointed out that in order to obtain the same results, if 'PropagationDir' is set as positive, then 'NacYaw' should be chosen with opposite sign and viceversa. As performed for wind shear, the simulation has been run in uniform steady wind conditions.

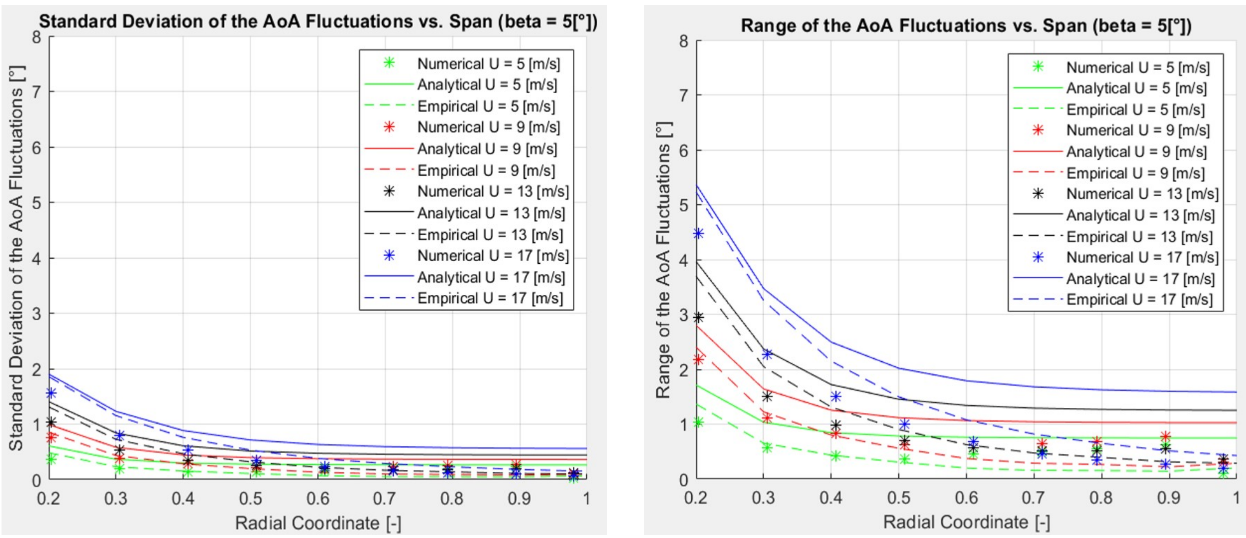

Figure 4.4: *(a) Standard Deviation of the AoA fluctuations vs. span (b) Range of AoA fluctuations vs. span, for $\beta = 5[°]$, comparison between analytical (solid lines), empirical (dashed lines) and numerical (stars) results.*

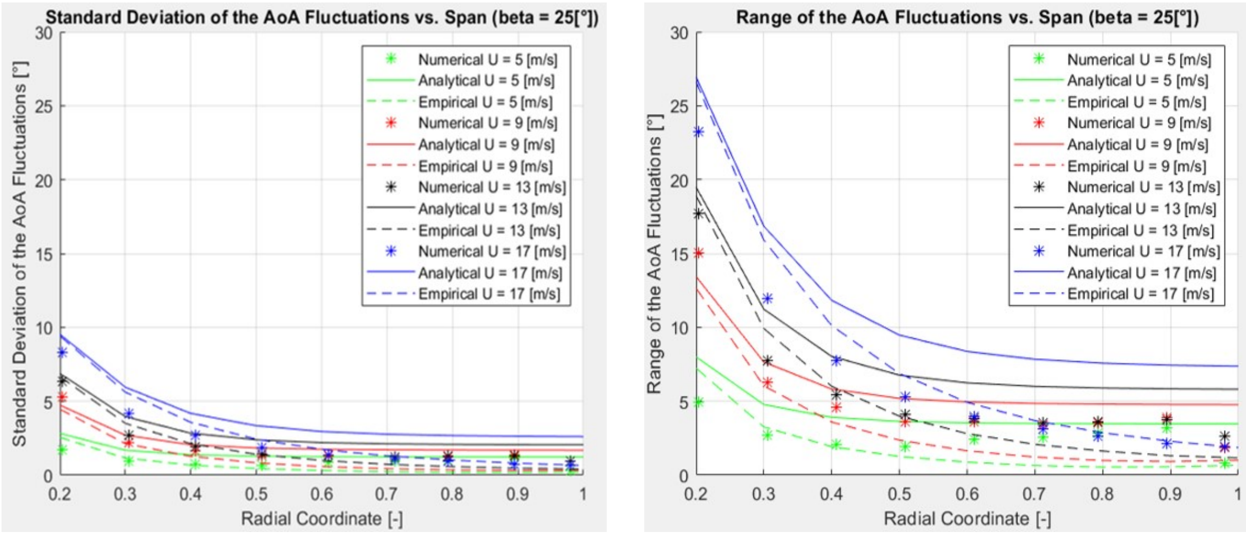

Figure 4.5: *(a) Standard Deviation of the AoA fluctuations vs. span (b) Range of AoA fluctuations vs. span, for* $\beta = 25[°]$*, comparison between analytical (solid lines), empirical (dashed lines) and numerical (stars) results.*

Figures 4.4 and 4.5 show the angle of attack fluctuations for two different values of the yaw angle β, respectively equal to 5 and 25 [°]; The left-hand figures represent the standard deviation of the AoA fluctuations, while the right-hand figures contain the information about the maximum range of AoA fluctuations experienced over a revolution. Moreover, the two different models presented in section 2.2.6 (empirical, eq. 2.2.29) and in section 3.2.2 (analytical) will be tested and compared. It can be noticed that the both the analytical and the empirical model follow the descending trend of the simulation results across the blade span, with a comparable magnitude. Although, it can be observed that for above rated wind speeds, towards the outboard stations, the analytical model deviates from the numerical results, which are best captured by the empirical model. As deeply discussed, the tip region of the blade is dominated by the skewed wake effect, meaning that the modelling of the axial induction factor becomes crucial. This can be observed in Figure 4.6, which shows the comparison among the analytical axial induction factor, the axial induction factor derived by using the empirical model and the numerical one, for an outboard stations at 80[%] of span, for (a) U = 5 and (b) 17 $[\frac{m}{s}]$ and in Figure 4.7, which shows the AoA which results from each of these axial induction factors. It is clear that, for U = 5 $[\frac{m}{s}]$ the analytical a best approximates the numerical axial induction factor, while the empirical model proves to be more accurate for U = 17 $[\frac{m}{s}]$. This argument can be used to justify the mismatch between the analytical and numerical model. Moreover, by comparing Figure 4.7a and b, it can be seen that at high TSR (e.g. low wind speed) the influence of the Skewed Wake effect on the induction factor is much larger than at low TSR (e.g. large wind speed), mainly because of the lower induction factor which occurs for large wind speeds.

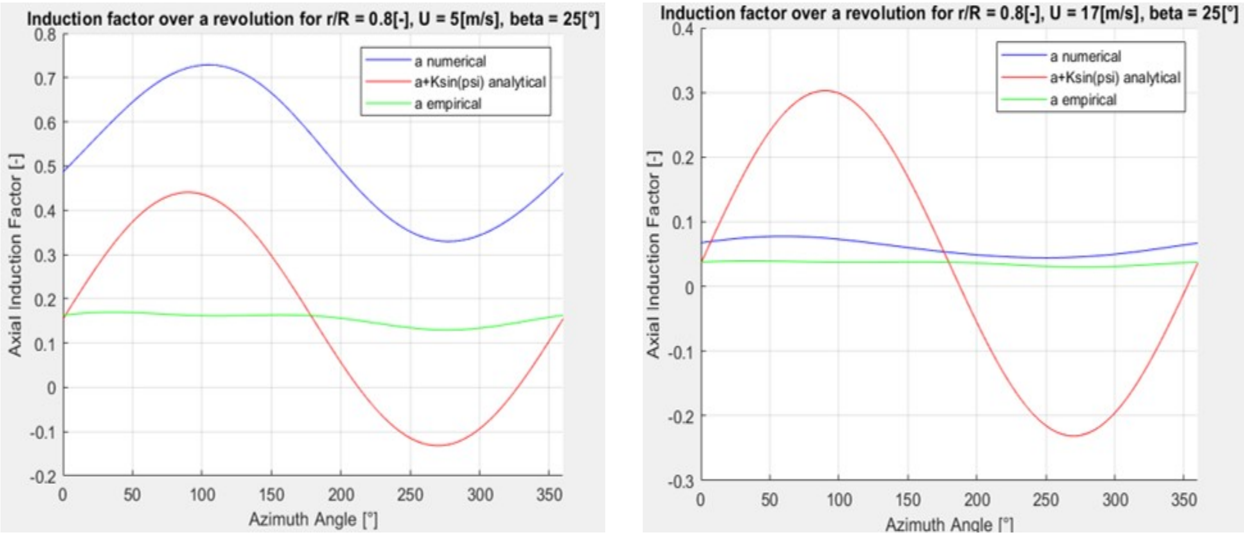

Figure 4.6: *Axial induction factor over a revolution for an outboard station of 80% of span for (a) U = 5* $[\frac{m}{s}]$ *(b) U = 17* $[\frac{m}{s}]$*, comparison between analytical (red line), empirical (green line) and numerical (blue line) results.*

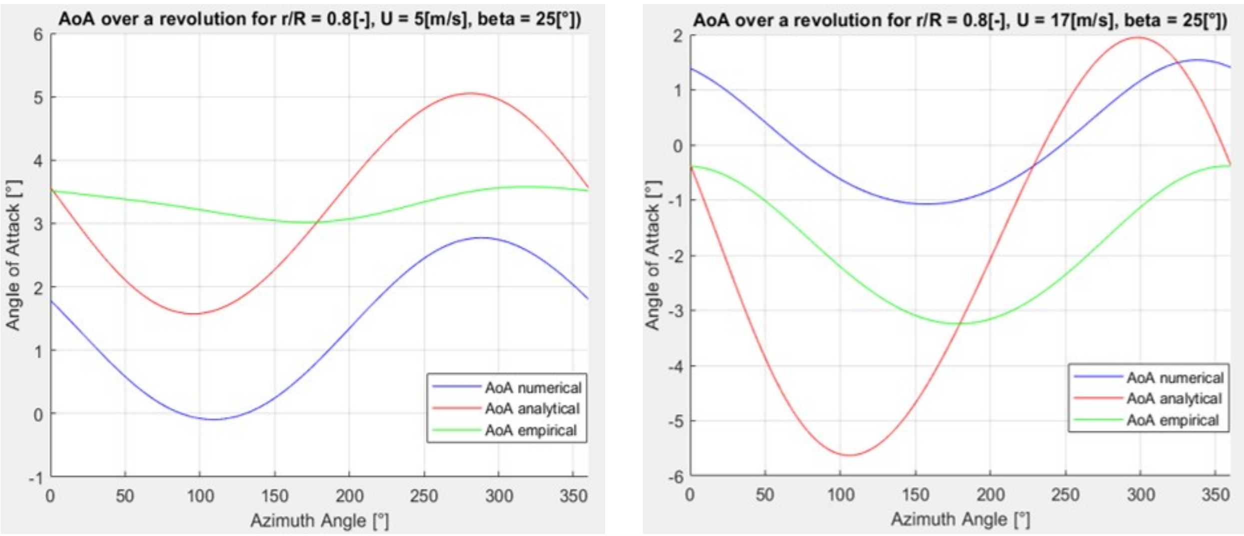

Figure 4.7: *Angle of Attack over a revolution for an outboard station of 80% of span for (a) U = 5* $[\frac{m}{s}]$ *(b) U = 17* $[\frac{m}{s}]$*, comparison between analytical (red line), empirical (green line) and numerical (blue line) results.*

Moreover, the influence of the unsteady effects on the results has been evaluated as well, by comparing the steady lift coefficient with the unsteady one, as can be seen in Figure 4.8. By using the AoA resulting from the time series of the simulation as input in the quasi-steady Lift polar curve, the steady C_l can be obtained. The unsteady C_l comes straightforward from the outputs of the simulations. The larger the difference between the steady and the unsteady Lift coefficient, the larger the impact of the unsteady effects is. As discussed in section 2.3, the unsteady effects play a major role towards inboard stations and this can be explained by thinking in terms of reduced frequency; indeed, the reduced frequency is inversely proportional to the relative velocity seen by the airfoil and consequently the lower the relative velocity the larger the unsteady effects. Inboards stations have a low rotational speed which makes the relative wind speed to be low, which makes the unsteady effects to be large. By applying the same reasoning, the unsteady effects should be larger for a 5 $\left[\frac{m}{s}\right]$ wind speed than for $U = 17\left[\frac{m}{s}\right]$; although, the reduced frequency is also proportional to the frequency of excitation, which, for angle of attack fluctuations is the rotational speed. The larger rotational speed for $U = 17\left[\frac{m}{s}\right]$ might explain the larger contribution of the unsteady aerodynamics effects for above rated wind speeds as well as the effect of dynamic stall.

Figures 4.9 and 4.10 show the steady and unsteady C_l for two values of wind speed (U = 5 (a)

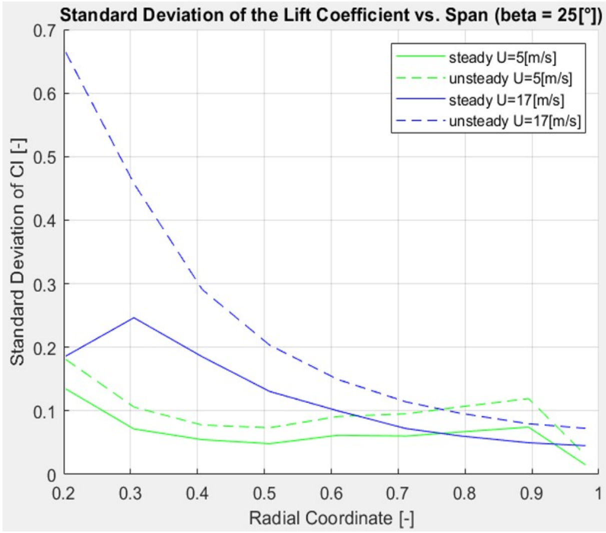

Figure 4.8: *Standard deviation of the Lift coefficient vs. span for a yaw angle $\beta = 25[°]$, comparison between steady and unsteady C_l, for U = 5 and 17 $[\frac{m}{s}]$.*

and 17 $[\frac{m}{s}]$ (b)) for an inboard and an outboard station, respectively. By comparing the trend of C_l between the inboard and the outboard station, it can be shown that the advancing and retreating blade effect is dominant for inboard stations (maximum and minimum value around $\psi = 0$ and $\psi = 180[°]$), while the skewed wake effects dominates for outboard stations (maximum and minimum value around $\psi = 90[°]$ and $\psi = 270[°]$). It can also be noticed that the unsteady C_l is slightly shifted on the right, with respect of the steady C_l. By recalling the discussion done in chapter 2.3 about the time constant, it can be understood how this shift represents the delay in the response. By looking at Figure 4.9b it can also be observed what happens in case of dynamic stall; indeed, for $\psi \approx 30[°]$ and $\psi \approx 320[°]$, when the stall AoA is exceeded, the steady Lift coefficient decreases, while the unsteady Lift coefficient keeps increasing.

This discussion proves that the unsteady effects play a non negligible role and they are more relevant towards inboard stations; this argument can partially explain the mismatch between the analytical and numerical results, recalling that the analytical model lays on the assumption of steady aerodynamics. Again, the fact that the model does not include the structural response of the blades can contribute to the mismatch between analytical and numerical results.

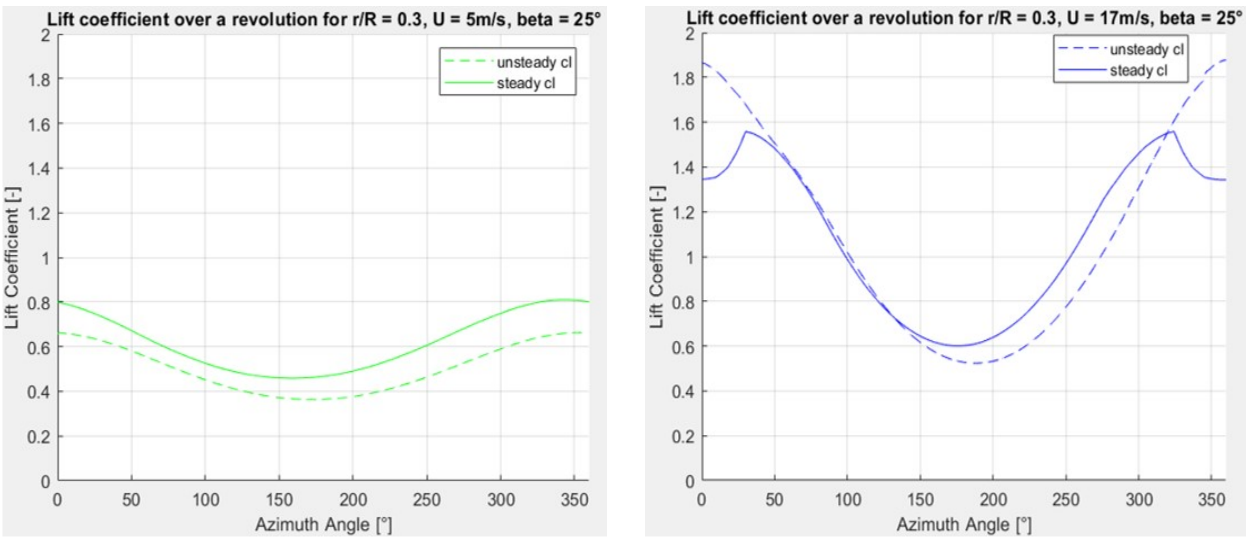

Figure 4.9: *Comparison between the steady and the unsteady Lift coefficient over a revolution for an inboard station of 30[%] of span, for (a) U=5$[\frac{m}{s}]$ and (b) U=17$[\frac{m}{s}]$.*

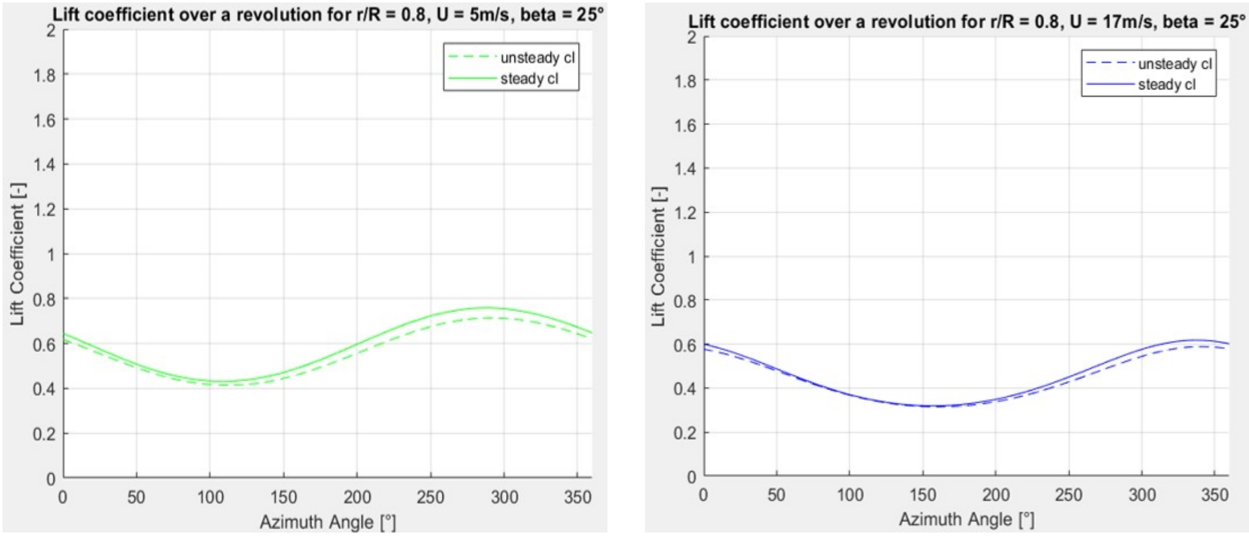

Figure 4.10: *Comparison between the steady and the unsteady Lift coefficient over a revolution for an outboard station of 80[%] of span, for (a) U=5[$\frac{m}{s}$] and (b) U=17[$\frac{m}{s}$].*

4.5 Atmospheric Turbulence Verification

Atmospheric turbulence can be simulated in FAST by setting the wind turbine class and the turbulence intensity characteristics, as discussed in section 2.2.4. This would mean that, following the scaling rules defined by the standards, it is not possible to relate each wind speed to each turbulence intensity value. It has been chosen to verify the model for two different conditions, namely Onshore and Offshore, to which different scaling rules are associated. Nevertheless, in order to evaluate how the analytical model performs according to different wind speeds, it would be ideal to use the same values of I, in order for the results to be only dependent on the wind speed. This can be done by setting the parameter 'IECturbc', in the 'InflowWind.m' file equal to the desired value of turbulence intensity.

Since atmospheric turbulence is a fast unsteady phenomenon, the instantaneous values of the wind speed could be either considerably larger or smaller than the average value. For this reason, it makes no sense to present the results in terms of maximum range over a revolution, because the local maximum (or minimum) would not be a trustworthy result, and consequently only the standard deviation of the AoA fluctuations will be discussed in this section. Figure 4.11 illustrates the standard deviation of the AoA fluctuations across the span, using the Offshore scaling rules for the turbulence intensity calculation (a) and the Onshore scaling rules (b). The analytical results show a clear descending trend across the span, while, the same does not always hold true for the simulation results; in particular, for $U = 13[\frac{m}{s}]$, the AoA fluctuations increase moving from inboard to outboard stations, while they decrease in all the other cases. This can be explained by thinking that this value of the wind speed is close to rated ($U = 11.4[\frac{m}{s}]$) and therefore the Thrust force will be around its maximum value. This means that the wind turbine blades will experience their maximum deflection and they will be more prone to vibration. Of course, both of these effects become more relevant at outboard stations and the increase in the AoA fluctuations around the tip region could be justified.

This graph does not perfectly allow to compare the results for different wind speeds, because the correspondent value of turbulence intensity will change as well, accordingly. In order to overcome this problem, Figure 4.12a aims to test the model when the value of turbulence intensity is arbitrarily set, meaning that, in this case, the scaling rules for the determination of I according to the wind speed (as prescribed by the IEC 61400 standards) have not been followed. The analytical results respect the trend of the AoA fluctuations either with respect of the wind speed U and with respect of the span fairly well. The larger mismatch is observed for the case where $U = 17[\frac{m}{s}]$ and I = 0.25[-]. Besides, it can be noticed how, for a blade span between 20 and 30 %, the steepness of the analytical and numerical curves consistently differ. In particular, for U = 5 $\left[\frac{m}{s}\right]$ the analytical curve is steeper than the numerical, while the opposite is true for U = 17 $\left[\frac{m}{s}\right]$. This difference can be partially justified by the choice of the induction factor used in the analytical model; indeed, by studying the derivative of the analytical pdf for AoA fluctuations with respect of the induction factor between 20 and 30 %

of span, it can be seen how the steepness of the analytical curve tend to adjust themselves to the numerical one, as can be observed in Table 4.1. The expression of the derivative follows:

$$\frac{dAoA_{\delta}}{da} = \frac{U(1-a)\Omega}{(\Omega r)^2 + (U(1-a))^2} \left[\frac{(1+\delta)\left(1 + tan^2\left(atan\left(\frac{U(1-a)}{\Omega r}\right)\right)\right)}{1 + \left((1+\delta)\left(\frac{U(1-a)}{\Omega r}\right)\right)^2} - 1 \right] \tag{4.5.1}$$

Case	Derivative (analytical a)	Derivative (numerical a)
U = 5 $\left[\frac{m}{s}\right]$, I = 0.10 [-]	-0.0749	-0.0724
U = 5 $\left[\frac{m}{s}\right]$, I = 0.25 [-]	-0.1904	-0.1855
U = 17 $\left[\frac{m}{s}\right]$, I = 0.10 [-]	-0.0239	-0.0381
U = 17 $\left[\frac{m}{s}\right]$, I = 0.25 [-]	-0.0352	-0.0723

Table 4.1: *Derivative of the AoA fluctuations between 20 and 30 % of span, using the analytical vaue of a and the numerical value of a.*

Figure 4.12b investigates how much the assumptions the model lays on influence the results; for this reason, three simulations have been run with different settings. In order to evaluate the influence of the hypothesis of infinite stiffness of the blades, the 'YawDOF' as well as the 'FlapDOF1', 'FlapDOF2' and the 'EdgeDOF' have been set to FALSE, meaning that the blade cannot move neither in the in-plane or in the out-of-plane direction. The hypothesis of negligible effect of the lateral and vertical turbulence has also been checked, by imposing the standard deviations of the wind speed along the lateral and vertical direction (namely, 'sigma2' and 'sigma3'), to be 0. Finally, the influence of the Prandtl's tip losses has been tested, by disabling the tip losses flag in the script. The results show that each of this hypothesis has an impact on the results. In particular, it can be observed that for wind speeds close to rated (black stars in the figure) the angle of attack fluctuations increases moving towards outboards stations. Although, when the blade are assumed to have infinite stiffness (dashed black line in the figure) the increasing trend is smoothed down, and this evidence should enhance that for wind speeds where the Thrust force is about maximum, the vibration and deflection of the blades play an important role in the blade-tip region. Nevertheless, the larger influence on the AoA fluctuations for outboard stations seems to be caused by the turbulence in the lateral and vertical direction (black diamond in the figure).

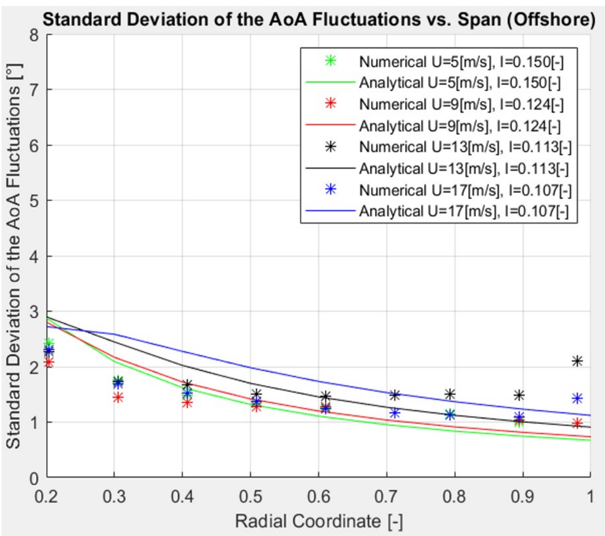

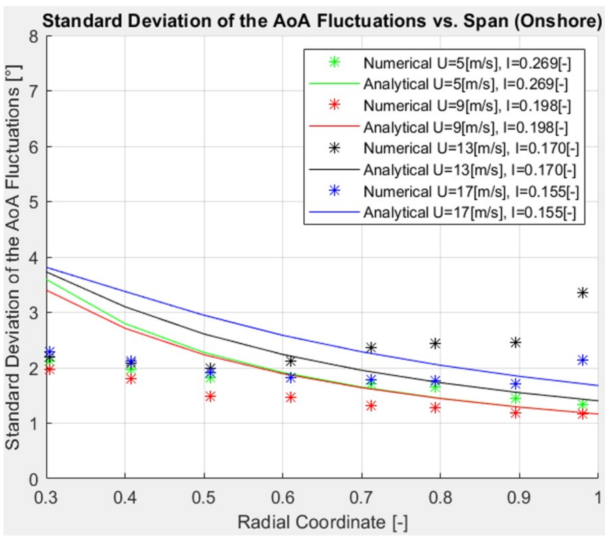

Figure 4.11: *Standard deviation of the Angle of Attack vs. span for (a) Offshore case (b) Onshore case.*

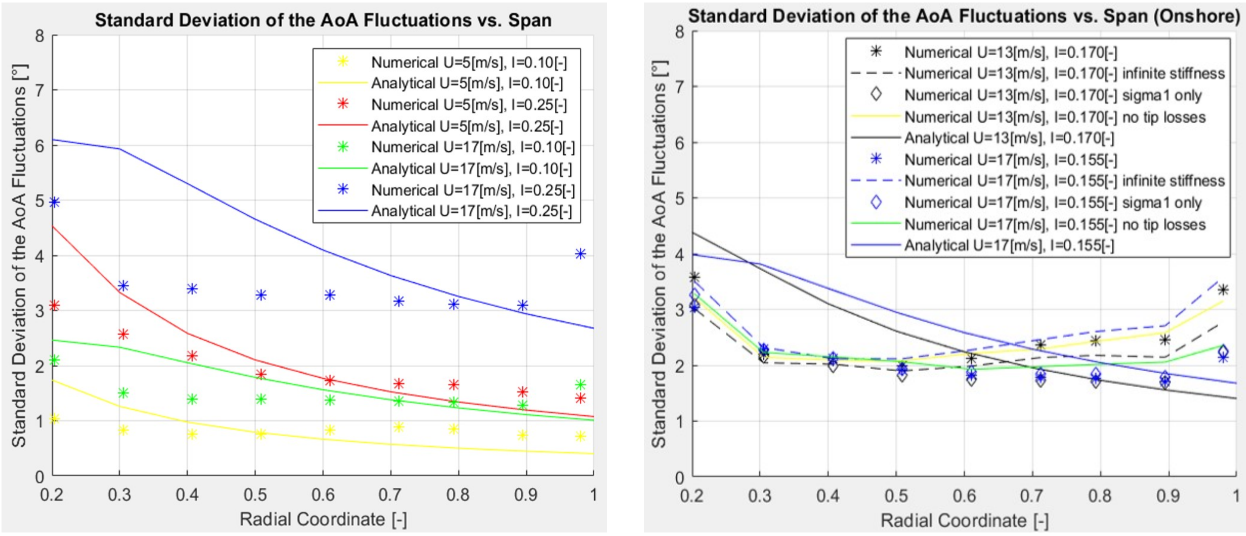

Figure 4.12: *Standard deviation of the Angle of Attack vs. span when turbulence intensity is arbitrarily set (a) Standard deviation of the AoA vs. span when the simulation settings have been changed to check the hypothesis used in the model (b).*

Another possible reason for the difference between analytical and numerical results can be attributed to the influence of the unsteady effects, as can be seen in Figure 4.13, where the standard deviation of the steady and unsteady Lift coefficient versus span is plotted and in Figure 4.14, where steady and unsteady C_l for $U = 5[\frac{m}{s}]$ is plotted over a revolution, for an inboard (a) and an outboard (b) station. The large value of turbulence intensity (I = 0.269 [-]) justifies the large fluctuations of the unsteady C_l; given the delay between excitation and response, the steady lift coefficient is not able to follow the fluctuations of the unsteady C_l and it results in a smoother curve. It can also be noticed that the fluctuations of the unsteady C_l are smaller for the outboard stations, which can be explained by thinking in terms of reduced frequency, as discussed in section 2.3.

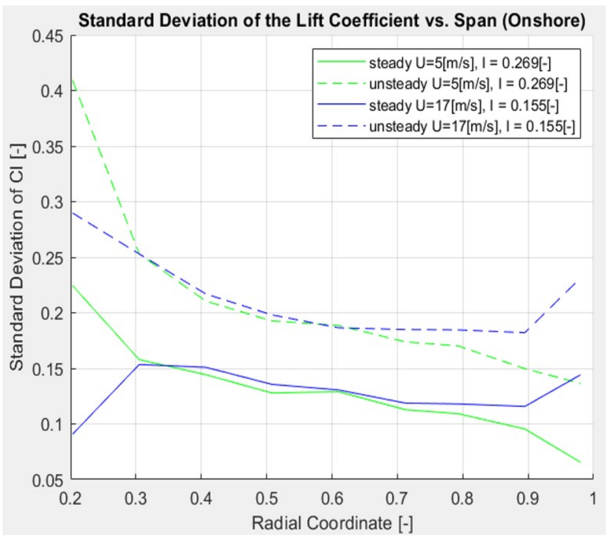

Figure 4.13: *Standard deviation of the Lift coefficient vs. span for the Onshore case, comparison between steady and unsteady C_l, for U = 5 and 17 $[\frac{m}{s}]$.*

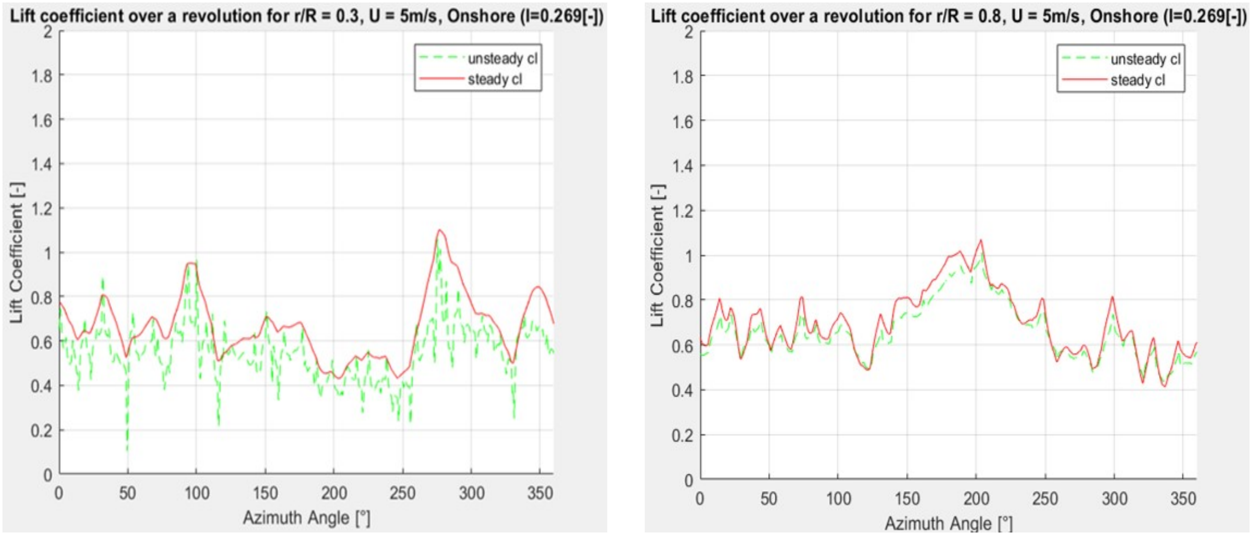

Figure 4.14: *Steady and unsteady Lift coefficient over a revolution, for* $U = 5[\frac{m}{s}]$*, for (a) inboard station at 30* [%] *of span (b) outboard station at 80* [%] *of span.*

4.6 Combined Perturbation Sources Verification

In the previous sections, the model used to represent each single perturbation source has been verified. This section aims to verify the combined effect of the three perturbation sources. In order to do so, several cases have been considered (for an Onshore, Near-Coastal and Offshore site) and a summary can be found in Table 3.3, in section 3.4. Figure 4.15, 4.16 and 4.17 show the analytical and numerical standard deviation of the AoA as a function of the blade span and, for each site, a 'good' and a 'bad' agreement between the two will be shown (more cases can be found in APPENDIX A).

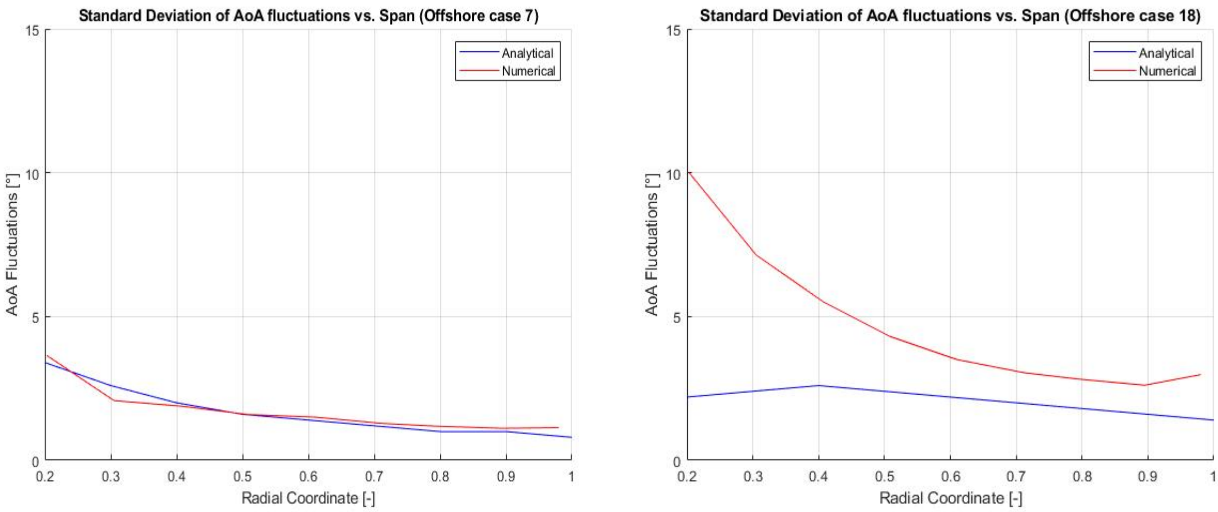

Figure 4.15: *Standard deviation of the AoA fluctuations for the Offshore site case 7 (TSR=7[-], I=0.14[-], β=10[°] and z_0=0.0002[m]) (a) and for the Offshore site case 18 (TSR=3[-], I=0.10[-], β=20[°] and z_0=0.0002[m])(b)*

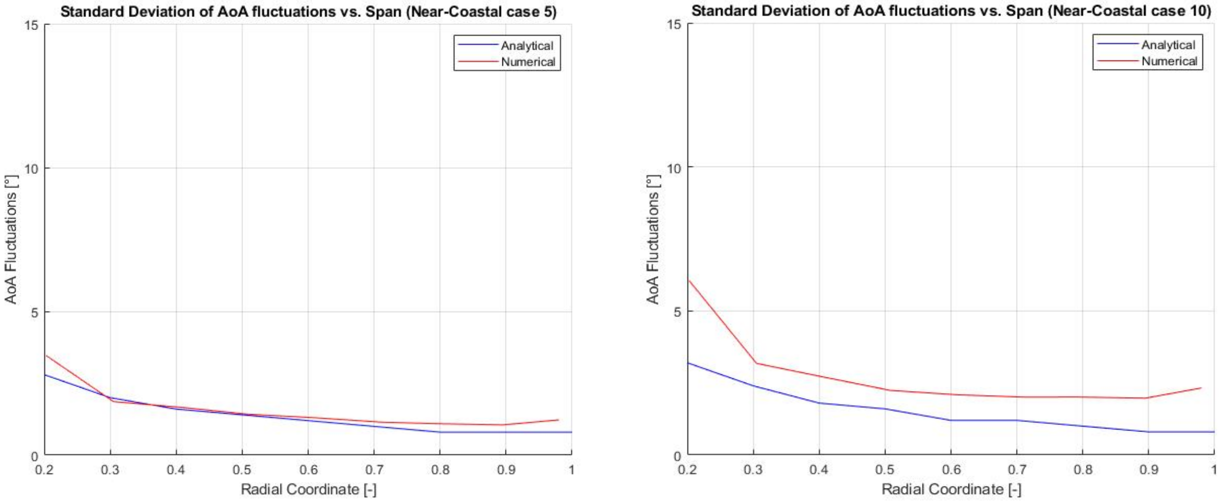

Figure 4.16: *Standard deviation of the AoA fluctuations for the Near-Coastal site case 5 (TSR=7[-], I=0.12[-], β=10[°] and z_0=0.005[m]) (a) and for the Near-Coastal site case 10 (TSR=7[-], I=0.14[-], β=20[°] and z_0=0.005[m])(b)*

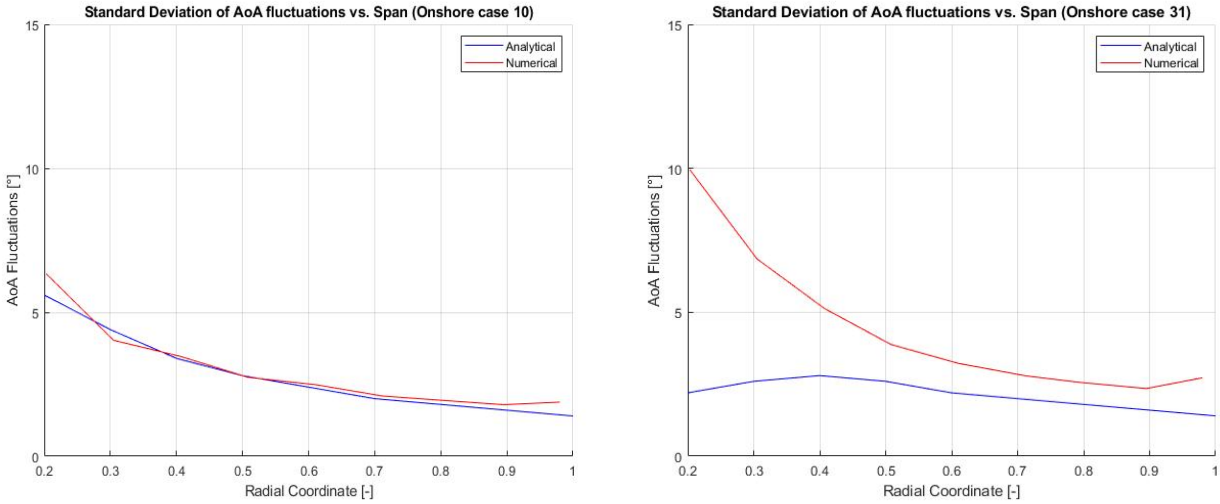

Figure 4.17: *Standard deviation of the AoA fluctuations for the Onshore site case 10 (TSR=7[-], I=0.25[-], β=10[°] and z_0=0.1[m]) (a) and for the Onshore site case 31 (TSR=3[-], I=0.12[-], β=20[°] and z_0=0.1[m])(b)*

Generally speaking, the analytical model is able to reproduce the trend of the angle of attack fluctuations with a comparable magnitude and most of the difference between the analytical and numerical results can be found for inboard stations. It can also be noticed that the three shown 'bad results' correspond to cases with a large yaw misalignment angle (20 °). Figures 4.19a, 4.19b and 4.20 summarize the results of all the simulated cases and they show the 'smeared' difference between the analytical and numerical results, which is subsequently averaged over the span; in particular (referring to the legend) 'total' refers to an average of the smeared difference between analytical and numerical results over the entire blade span, 'inboard' over a blade span from 20 to 40 % and 'outboard' over a blade span from 40 to 100 %. The term 'smeared' means that firstly the average over a revolution of the standard deviation of the AoA has been computed and subsequently the difference between the numerical and analytical results has been taken. This is different from presenting the 'resolved' results, which compute the difference between the standard deviation of the AoA between the analytical and numerical results at each azimuthal position over a revolution and subsequently taking the [0 360°[average value of the difference. The 'resolved' results would therefore yield a more accurate result, though, this advantage comes at the price of computational time. A sensitivity analysis has been performed to evaluate the difference between the 'smeared' and 'resolved' results, for case 31 of the

Onshore site; this can be observed in Figure 4.18.

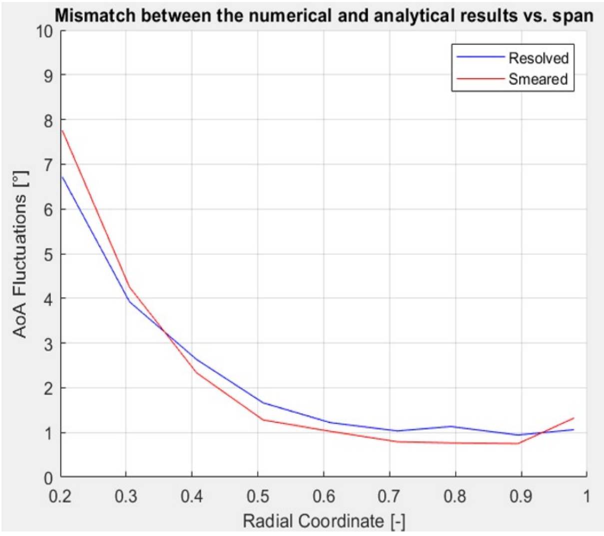

Figure 4.18: *Comparison between the smeared and resolved difference between the analytical and numerical AoA fluctuations, for case 31 of an Onshore site.*

It can be seen that the difference between the 'smeared' and 'resolved' results is almost negligible and consequently it is acceptable to show the 'smeared' results. Moreover, this evidence enhances the fact that turbulence intensity plays the major role in terms of resultant AoA fluctuations. Indeed, both wind shear and yaw misalignment effects vary along with the azimuth angle, while turbulence intensity has been kept constant with respect of ψ. Consequently, the fact that the difference is small over a revolution suggests that the dominant effect is the one that does not change with the azimuth angle, namely turbulence intensity.

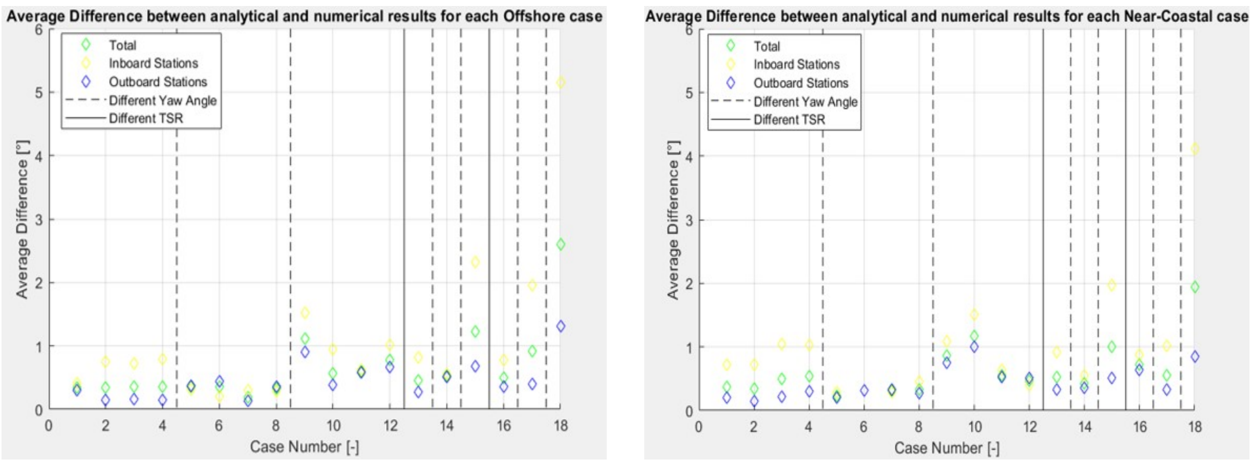

Figure 4.19: *Overview of the 'smeared' difference between the numerical and analytical results for each case of an Offshore (a) and a Near-Coastal (b) site. The dashed black line are used to separate the cases with different yaw angle, while the solid black lines to differentiate from cases with different TSR.*

From Figures 4.19a, 4.19b and 4.20 it can be seen that overall, the model performs well considering that most of the difference between numerical and analytical results is below 1 °. Again, it can be observed that predictions for outboard stations are more accurate than for inboard stations and that the worst results are often associated with cases with large yaw misalignment angle.

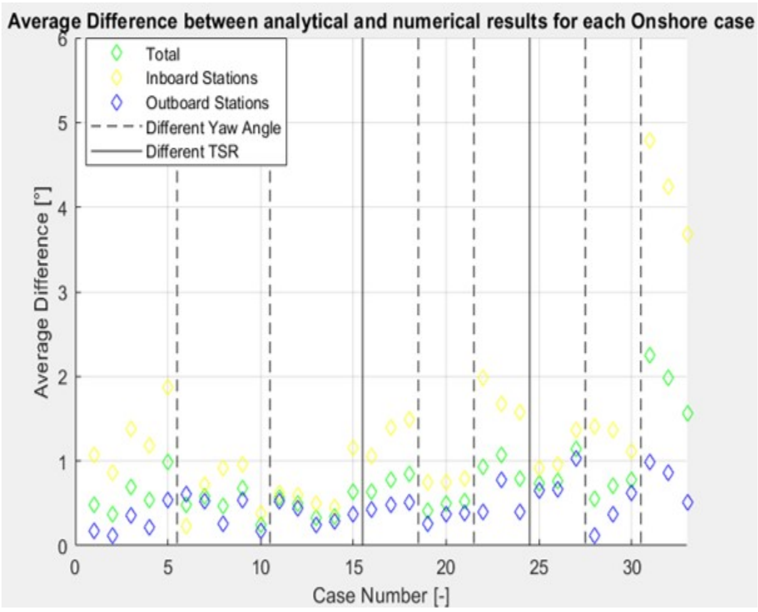

Figure 4.20: *Overview of the 'smeared' difference between the numerical and analytical results for each case of an Onshore site. The dashed black line are used to separate the cases with different yaw angle, while the solid black lines to differentiate from cases with different TSR.*

4.7 Probability of occurrence of Stall

This section will present a method to estimate the probability of occurrence of stall as well as its verification. The verification has been carried out using airfoils of the NREL 5MW wind turbine, summarized in Table 4.2. The stall probability can be forecasted by calculating the fraction of the probability density function for the AoA fluctuations where the angle of attack is larger than the stall angle and dividing it by the total probability of occurrence of the AoA fluctuations, as follows:

Airfoil	Span-wise range [-]	AoA_{opt} [°]	AoA_{stall} [°]
DU99-W-350	0.2-0.29	8	11.5
DU97-W2-300	0.3-0.39	7.5	9
DU91-W2-350	0.4-0.49	5	8.5
DU93-W-210	0.5-0.64	3.5	8
NACA 64-618	0.65-1	5	9

Table 4.2: *Summary of the airfoils used in the NREL 5MW turbine for each considered span-wise fraction.*

$$p(\alpha > \alpha_{stall}) = \frac{\int_{\alpha_{stall}}^{\alpha_{opt}+3\sigma_\alpha} p(\alpha)\, d\alpha}{\int_{\alpha_{opt}-3\sigma_\alpha}^{\alpha_{opt}+3\sigma_\alpha} p(\alpha)\, d\alpha} \tag{4.7.1}$$

It should be pointed out that the pdf for AoA fluctuations is not perfectly Gaussian, but it is similar enough to state that the sigma rule can still be applied and consequently $3 * \sigma_\alpha$ allows to consider about 99.7% of the data. The analytical expression for probability of stall estimation has been tested with FAST for the two cases ('good' and 'bad' agreement shown in section 4.6) presented for the Onshore and Offshore scenario, as it can be seen in Figures 4.21a and b. For a blade root section at about 20% of the span, the analytical estimation of the stall probability is very different from the numerical one, probably due to the strong influence of the unsteady effects which are not accounted in the analytical model. However, from 30% of span on, the analytical expression manages to reproduce the trend of the numerical model with a comparable magnitude and trend. The red curve shows a better match than the blue curve and this could be due to the fact that the blue curves are cases with large yaw misalignment angles where the analytical model has proved to be less accurate. In particular, an underestimation of the operational AoA range leads to an underestimation of the stall probability of occurrence.

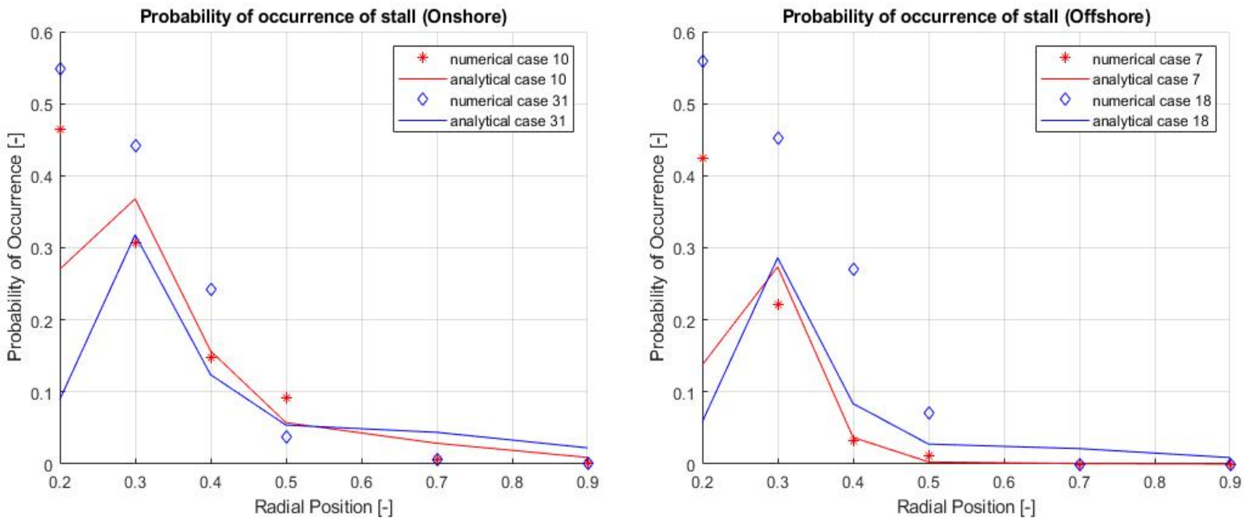

Figure 4.21: *Probability of occurrence of stall vs. span, comparison between numerical and analytical results for the Onshore (a) and Offshore (b) scenarios*

Chapter 5

Optimization Framework

In this chapter the framework of the multi-objective optimization tool used for the airfoil design and optimization (Optiflow) will be discussed. In particular, the three main components will be highlighted, namely:

- The parametrization technique used to represent the airfoil geometry;
- The genetic algorithm key-points and its architecture;
- The tool used for the aerodynamic characteristics computation (RFOIL)
- The Cost Function which is used to assign a score to each airfoil candidate.

Each of these components will be discussed in a different section.

5.1 CST Parametrization

The Class function Shape function Transformation technique (CST) allows a mathematical representation of a typical airfoil geometry. A detailed explanation about the method can be found in [51]. The airfoil shape can be parametrized as:

$$\zeta(\psi) = \sqrt{\psi}(1-\psi)\sum_{i=0}^{N} A_i \psi^i + \psi\zeta_t \tag{5.1.1}$$

Where $\psi = \frac{x}{c}$, $\zeta = \frac{z}{c}$ and $\zeta_t = \frac{\Delta z_{TE}}{c}$ and c is the chord. The meaning of the terms that constitute the equation will be analyzed below.

The Class Function defines the basic airfoil shape, and it is expressed as:

$$C(\psi)^{N_1}_{N_2} = \psi^{N_1}(1-\psi)^{N_2} \tag{5.1.2}$$

In order to obtain a round nose airfoil, the necessary condition is $N_1 = 0.5$, while a sharp trailing edge can be obtained by imposing $N_2 = 1$. It is clear that by setting N_1 and N_2 as done, the class function becomes $\sqrt{\psi}(1-\psi)$. However, N_1 and N_2 can be varied in order to parametrize different airfoil shapes.

The Shape function is needed to properly modify the airfoil geometry in order to match design goals or to respect constraints. It can be described as:

$$S(\psi) = \frac{\zeta(\psi) - \psi\xi_t}{\sqrt{\psi}(1-\psi)} = S\left(\frac{x}{c}\right) = \sum_{i=0}^{N} A_i \left[\frac{x}{c}\right]^i \tag{5.1.3}$$

Where the second equivalence is derived using equation (5.1.1).

The shape function can be represented by the unit shape function, defined as $S(\psi) = 1$. The unit shape function can be seen as a summation of various order Bernstein Polynomials, according to the partition of unit:

$$\sum_{r=0}^{n} S_{r,n}(x) = 1 \quad for \quad 0 \leq x \leq 1 \tag{5.1.4}$$

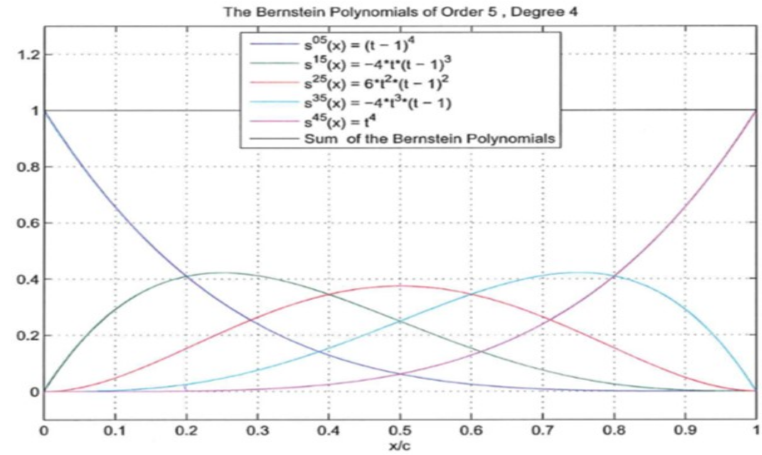

Figure 5.1: *Representation of the Bernstein polynomials of order 5 degree 4 [52]*

A graphic representation of the Bernstein polynomials is shown in Figure 5.1. The general Bernstein Polynomials can be written as:

$$S_{r,n}(x) = K_{r,n} x^r (1-x)^{n-r} \tag{5.1.5}$$

Where r ranges between 0 and n (order of the Bernstein Polynomials), while the binomial coefficient $K_{r,n}$ is defined as:

$$K_{r,n} \equiv \binom{n}{r} \equiv \frac{n!}{r!(n-r)!} \tag{5.1.6}$$

The values that the shape function assumes at the edges (first and last term), meaning $\frac{x}{c} = 0$ and $\frac{x}{c} = 1$ are of relevant importance. In particular, $S(0) = \sqrt{\frac{2R_{LE}}{c}}$, so it relates the shape function with the radius of the leading edge R_{LE}. On the other hand, $S(1) = tan(\beta) + \frac{\Delta z_{TE}}{c}$, where β is the boat-tail angle and the term Δz_{TE} allows to control the trailing edge. All the polynomials in between have no effect on the leading edge radius and on the boat-tail angle.

The shape function that represents the upper surface of the airfoil is not the same that represents the lower surface. Indeed, the overall shape function for the upper and the lower airfoil surface are, respectively:

$$S_U(\psi) = \sum_{i=1}^{n} A_{U,i}\ S_i(\psi) \tag{5.1.7}$$

$$S_L(\psi) = \sum_{i=1}^{n} A_{L,i}\ S_i(\psi) \tag{5.1.8}$$

Where the coefficients A_U and A_L can be determined, for instance, as variables in a numerical design optimization problem, $S_i = K_i \psi^i (1-\psi)^{n-1}$ and K_i is defined as in equation (5.1.6). Finally, the shape of the upper and the lower surface of the airfoil can be parametrized as follows:

$$\zeta_{upper} = C_{N_2}^{N_1}(\psi)\ S_U(\psi) + \psi \Delta\xi_U \tag{5.1.9}$$

$$\zeta_{lower} = C_{N_2}^{N_1}(\psi)\ S_L(\psi) + \psi \Delta\xi_L \tag{5.1.10}$$

This method owns some relevant properties:

- the whole design space of airfoil can be described by this technique;

- the unit shape function is sufficient to describe each airfoil in the design space;
- every airfoil in the design space can be derived from any other airfoil in the design space.

5.2 Genetic Algorithm

This section will discuss the genetic algorithm, which is used in Optiflow to solve the numerical multi-objective optimization. The term 'genetic' refers to the Darwin's theory of evolution, which basically states that if changes in the characteristic properties of a certain individual result in an improvement of his performance, a natural selection process will lead these new individuals to outlive the others, becoming the first individuals of a new generation. Consequently, the genetic algorithm will start from a set of commonly used airfoils (namely individuals), defined as pool, and it will progressively combine them together, in order to generate a new generation of airfoils. The number of individuals which will be generated for each generation (population size) is an input to the optimization and it has to be selected by the user as well as the number of generations. A large population size and a large number of generations would be ideal because it increases the chances of reaching the optimal solution, but it comes at the expenses of computational time, consequently a trade-off between these two aspects should be found. Each of the new individual will be tested and a score will be assigned to it, based on the value of the cost function. The optimizer will therefore re-combine the airfoils with the best score, in order to give birth to a new generation. This process will be iterated until the final solution is reached, meaning that the number of generations is exceeded. If only the airfoil shapes with the best score would be recombined together, it is possible that the optimization process will lead to a non-optimal solution or an algorithm stall. In order to solve this problem, the genetic algorithm presented in [52] uses the NSGA II algorithm, which has the main feature of the distance covering strategy. This strategy mainly aims to avoid to get stuck in a local minimum, meaning that the crossover (the genetic operator that handles the recombination process) will keep airfoil's shapes with features which are different from the ones in the Pareto Front. This is done to provide diversity no matter how good or bad those performance are, increasing the chances of further improvements of the new generation with respect of the previous. The main convergence criteria used in the algorithm is based on the distance from the Pareto front. This is enhanced by setting a Pareto fraction, which tells which individuals should be kept in the Pareto front. If the Pareto fraction is large, the Pareto front will be more populated but it has the downside of a larger probability of reaching a non-optimal solution.

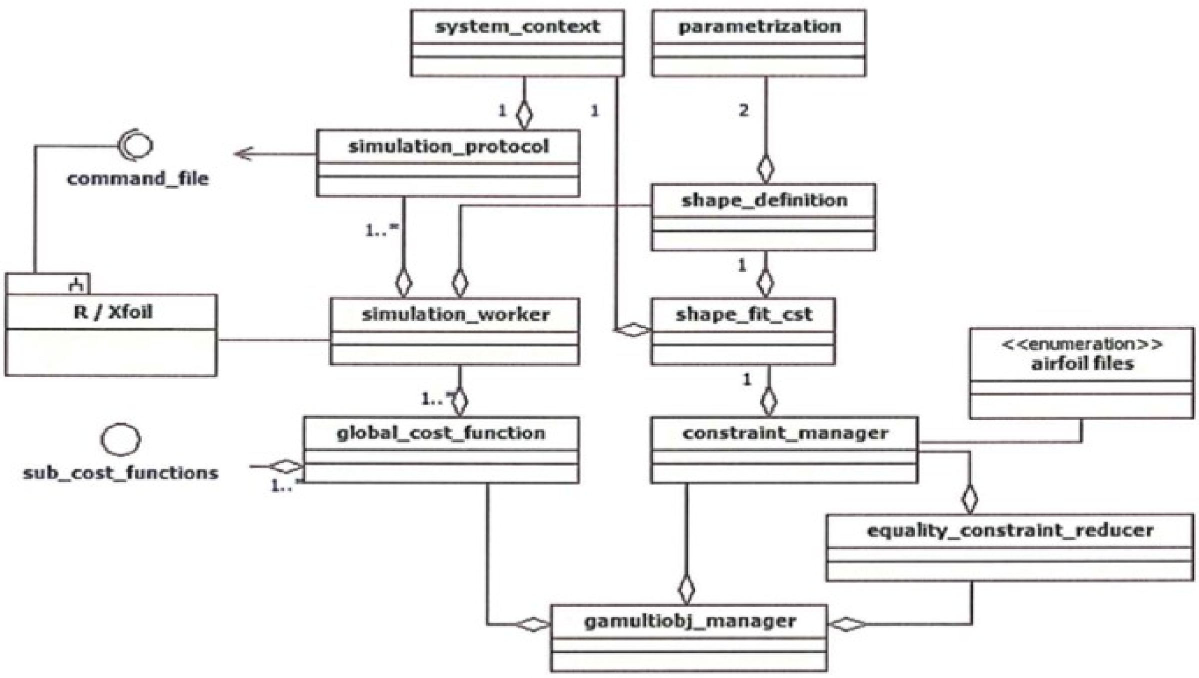

Figure 5.2: *Flow chart to schematize the architecture of the genetic algorithm [52]*

The architecture of the genetic algorithm is schematized in Figure 5.2. The system context is mainly responsible for the interactions with the operating system and the hardware and its main task is to manage paths, permissions and temporary folders. The simulation protocol provides the set up and the instructions to the simulation worker, which allows to execute RFOIL, from which the aerodynamic properties of the airfoil candidate can be obtained. The airfoil shape is generated by the shape definition object, which uses one parametrization object for the upper airfoil surface and one for the lower surface. Each parametrization object provides the mathematical expressions used for the airfoil description and fitting. Once the aerodynamic properties of the airfoil are calculated, the global cost function computes the value of the total cost function, which, being a multi-optimization problem, should be formed by at least two single-objective cost functions. The relationship between the single-objective cost functions and the simulation worker are given by a connectivity matrix, which tells what protocol should be followed by each cost function. The constraint manager defines the constraints the optimization is subject to. As discussed in [53], there are different ways to deal with constraints, which can be narrowed down to two main types, namely soft and hard constraints. The soft constraint type is addressed by including a penalization factor; this means that whether a certain airfoil candidate exceeds a constraints, this individual will not be completely excluded from the Pareto Front, but the value of the cost function will be penalized. While proceeding towards large number of generations, the penalized candidates will progressively be excluded from the Pareto front, because better candidates will be generated, so that the optimal solution will respect the constraints while keeping a broader variety of airfoil in the recombination process. On the other hand, the hard constraints are set in such a way that, if the airfoil candidate will not respect the constraints, the individual will be excluded from the optimization. This gives the certainty of having feasible solutions, but comes at the price of a lower variety of different airfoil shapes which might lead to a non-optimal solution. Finally, the game multi-objective manager ensures the correct set up and execution of the optimization algorithm.

5.3 RFOIL

This section will briefly introduce the tool which is used in Optiflow to calculate the aerodynamic characteristics of each airfoil candidate, namely: RFOIL. RFOIL has been developed by the TU Delft Wind Energy research group and it can be considered an implementation of XFOIL. One of the main features of RFOIL is that it includes the rotational effects, which are particularly relevant at inboard stations, and they are not accounted for in XFOIL. However, the rotational effects have not been included in the aerodynamic polar calculation in this work and consequently they will not be discussed in details. Moreover, since the latest RFOIL version has been used, which includes the learned boundary layer closure relationship from the airfoil polars;for this reason, a comparison with previous (original) RFOIL version will be shown in this section.

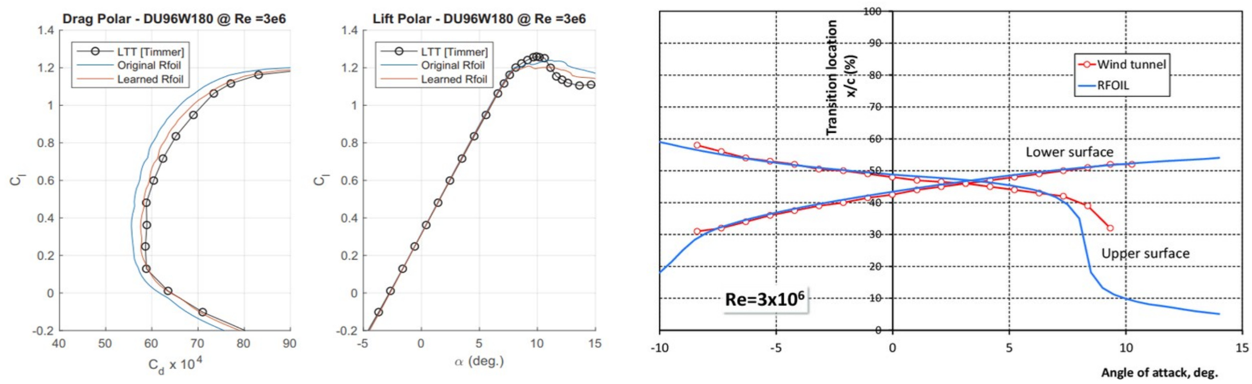

Figure 5.3: *(a) Comparison between Drag and Lift polar (RFOIL predictions) with LTT measurements (b) Comparison between transition point on the upper and lower surface (RFOIL prediction) vs. Wind tunnel results [57]*

The main aim of this section is to evaluate how accurately RFOIL can predict the aerodynamic characteristics to justify its usage in the airfoil design process. This can be observed in Figure 5.3 which respectively show the lift polar, the C_l vs C_d and the transition point comparison between a Low Turbulence wind Tunnel test (LTT) and the RFOIL predictions. The Lift polars show a very good agreement in the linear region, while, the RFOIL predictions start deviating from the wind tunnel results, when $\alpha > \alpha_{stall}$. The accuracy of the Drag polar is lower than for the Lift polar and it has been found that RFOIL tends to underestimate Drag and this issues is more relevant for airfoils which experience a turbulent flow over a large chord portion, mainly because the main source of inaccuracy has been linked with issues in the turbulent closure [57]. As for the transition point location estimation, very good results are obtained for the lower surface transition point, while a slightly larger error can be detected for the transition point location on the upper surface, which becomes more relevant as the AoA increases. These results prompt the validity of the program for aerodynamic characteristics calculation.

5.4 Cost Function

This section will provide possible expressions for the cost functions which can be used in Optiflow. First, the definition of the cost function which has been employed to carry out the most of the analysis will be presented in section 5.4.1 while, in section 5.4.3, the definition of alternative cost functions, to account for different wind energy airfoil requirements will be discussed. The geometrical and aerodynamic constraints imposed in the simulations will be presented in section 5.4.2.

5.4.1 Cost Function Definition

This section will define the cost functions which have been mostly used for designing and optimizing airfoils in this work. As discussed in section 2.4, several requirements are important for wind energy airfoils, among which, maximizing the Lift over Drag ratio is the most relevant, because it ensures the maximum aerodynamic efficiency. The optimization set up is defined as a minimization procedure and consequently the cost function must be expressed as a quantity that is wanted to minimize. Besides, being Optiflow a multi-objective optimizer, at least two cost functions should be specified for each optimization.

This work has focused on the study of the probabilistic approach and consequently it is wanted to evaluate what is the impact of including the probabilistic design (also referred to as '**robust design**' in this work) in the airfoil optimization process. In order to do so, it has been decided to associate the Cost Function 1 (CF1) to the 'one point design', meaning maximizing the $\frac{C_l}{C_d}$ at the optimal angle of attack, while the Cost Function 2 (CF2) is related to the 'robust design', which uses the probability of the angle of attack fluctuations discussed in this work and aims to maximize the Lift over Drag ratio across the estimated operational angle of attack range. Besides, it can be argued that, in order for the optimization to be most effective, the two cost-functions should be in contrast with each other. If the two cost functions present similar outputs, it is possible that Pareto front would be condensed into small CFs intervals, namely, the variability of the airfoil geometry along the Pareto front would be small, resulting in an almost 'single airfoil shape', rather than in an airfoil family.

In order to stress the difference between the two cost functions, the CF1 will evaluate the aerodynamic characteristics of the airfoil candidate in the clean configuration, while, the CF2 in the rough configuration. The expression for the two CFs is provided as follows:

$$CF1_{LD_{clean}} = -\left.\frac{C_l(\alpha_{opt})}{C_d(\alpha_{opt})}\right|_{clean} \tag{5.4.1}$$

$$CF2_{LD_{rough}} = -\int_{\alpha_{opt}-\sigma_{alpha}}^{\alpha_{opt}+\sigma_{alpha}} \left.\frac{C_l(\alpha)}{C_d(\alpha)}\right|_{rough} \times p(\alpha)\, d\alpha \tag{5.4.2}$$

Where σ_{alpha} is the standard deviation of the angle of attack fluctuations obtained from $p(\alpha)$, which is the probability density function which results from the output of the probabilistic design space mapping carried out in section 3.4.

5.4.2 Geometric and Aerodynamic Constraints

In this section, the geometric and aerodynamic constraints which have been used in the optimization will be described. It must be pointed out that Optiflow is not a tool specifically tailored for wind energy airfoils, but it has the potential to be adopted for every airfoil application. Consequently, it is necessary to specify a set of constraints to guide the optimizer into finding airfoils which are both feasible in terms of aerodynamic and manifactural constraints for wind airfoil applications.

The aerodynamic constraints have been mainly set to exclude ultra-high performance. These kind of constraints are treated as hard constraints, meaning that whether this constraint is exceeded, the airfoil candidate will receive a score of 0 and consequently it will be excluded a priori from the Pareto front. It has been chosen to follow the Optiflow default settings for such a constraint and in particular:

$$\frac{L}{D}(\alpha_{opt})\bigg|_{clean} < 300 \quad ; \quad \frac{L}{D}(\alpha_{opt})\bigg|_{rough} < 160 \tag{5.4.3}$$

During the several tests necessary to define the optimization set up, it has been noticed that the optimal angle of attack, for some airfoils in the Pareto front, was negative. Usually the optimal angle of attack is positive and it might be negative for very outboard stations, which have not been considered in the analysis. Consequently, it has also been decided to exclude ultra-low performance by setting the conditions for the minimum value of the angle of attack and of the Lift coefficient at the optimal angle of attack (the influence of imposing this constraint is shown in APPENDIX B.1.2), as follows:

$$\alpha_{opt} > 0 \quad ; \quad C_l(\alpha_{opt}) > 0.6 \tag{5.4.4}$$

The geometric constraints have been treated as a mix of hard and soft constraints. In order for the airfoil to be feasible from the manifactural point of view, a minimum TE thickness should be enforced. This soft constraint has been set by reducing the value of the cost function by a penalization factor (pf). The airfoil candidate will be therefore penalized based on the thickness exceedance, which tells by how much the minimum thickness of the airfoil candidate is lower than the reference value, in particular at $\frac{x}{c} = 75\%$ and $\frac{x}{c} = 90\%$. The reference minimum thickness values have been taken from the DU airfoils used in NREL 5 MW machine and decreased by a factor of 0.7. The expression for the penalization factor is:

$$pf_{minthickness} = (1 - pf_{75})^2 \times (1 - pf_{90})^2 \tag{5.4.5}$$

where pf_{75} and pf_{90} are respectively the thickness exceedance at $\frac{x}{c} = 75\%$ and $\frac{x}{c} = 90\%$.

Moreover, the results of the optimizations showed a change in the upper surface concavity, moving from a concave down shape in the LE region to a concave up shape in the TE region. Airfoils with such a feature might be desirable for actuation purposes [54], but they have the drawback to increase the adverse pressure gradient which might result in an earlier flow separation and decreased aerodynamic performance. For this reason, it has been decided to set a hard constraint on the shape of the upper surface, allowing a concave down shape only (the influence of such a constraint is shown in APPENDIX B.1.1). This condition has been set by imposing:

$$\frac{\partial^2 t}{\partial x^2} < 0 \tag{5.4.6}$$

5.4.3 Alternative Cost Functions

This section will describe alternative cost functions which can be used for wind energy airfoils design and optimization. First of all, an alternative formulation of the cost function presented in section 5.4.1 will be discussed.

In section 5.4.1, the CF1 was only evaluating the aerodynamic characteristics of the airfoil candidate in the clean configuration, while the CF2 in the rough configuration only. Now, it is wanted to see if there are any advantages in expressing each one of these cost functions as a trade-off between the values of the CF in the clean and in the rough configuration. In particular, the trade-off is accounted for by introducing a mingle factor (MF). Consequently, in this case the CF1 and CF2 will still be associated to a 'one point' and a 'robust' design, respectively, but the formulation of the cost functions becomes:

$$CF1_{LD} = -\left[(1-MF)\frac{C_l(\alpha_{opt})}{C_d(\alpha_{opt})}\bigg|_{clean} + MF\frac{C_l(\alpha_{opt})}{C_d(\alpha_{opt})}\bigg|_{rough}\right] \tag{5.4.7}$$

$$CF2_{LD} = -\left[(1-MF)\int_{\alpha_{opt}-\sigma_{alpha}}^{\alpha_{opt}+\sigma_{alpha}} \frac{C_l(\alpha)}{C_d(\alpha)}\bigg|_{clean} \times p(\alpha)\,d\alpha + MF\int_{\alpha_{opt}-\sigma_{alpha}}^{\alpha_{opt}+\sigma_{alpha}} \frac{C_l(\alpha)}{C_d(\alpha)}\bigg|_{rough} \times p(\alpha)\,d\alpha\right] \tag{5.4.8}$$

Where MF is the mingle factor which is set to 0.5, σ_{alpha} is the standard deviation of the angle of attack fluctuations obtained from $p(\alpha)$, which is the probability of the angle of attack fluctuations.

Other wind energy airfoil requirements which could be implemented are, for instance, maximum optimal C_l, a relatively broad interval between the optimal angle of attack and the stall angle of attack, to ensure that the off-design conditions are sufficiently far from the design conditions and roughness insensitivity. The term 'relatively broad' might appear controversial. This is not a quantity which can be maximized, because the stall angle of attack can be increased up to a certain point due to physical constraints, meaning that if this distance is wanted to be maximum, the optimizer will push the optimal angle of attack towards low values of angle of attack, resulting in considerable lower Lift coefficient design values, which is not desired. This task is partially and intrinsically included in the $CF2_{LD}$. Assuming that the stall angle will fall within the estimated angle of attack range, the Lift coefficient will decrease, making the value of CF2 smaller with respect of an airfoil candidate which presents a stall angle of attack outside the estimated range of angle of attack. Nevertheless, a possible expression for such a cost function would be [54]:

$$CF1_{stall} = \frac{\alpha_{stall} - \alpha_{opt}}{C_l(\alpha_{stall}) - C_l(\alpha_{opt})} \tag{5.4.9}$$

$$CF2_{stall} = \frac{\alpha_{stall} - \alpha_{opt}}{\int_{\alpha_{opt}-\sigma_{alpha}}^{\alpha_{opt}+\sigma_{alpha}} [C_l(\alpha_{stall}) - C_l(\alpha_{opt})] \times p(\alpha)\, d\alpha} \tag{5.4.10}$$

The roughness insensitivity goal can be achieved, for instance, by imposing that the difference between the C_l at the optimal angle of attack in the clean configuration and the C_l at the optimal angle of attack in the rough configuration to be minimized as in [54]:

$$CF1_{sens} = \left| C_l(\alpha_{opt})|_{clean} - C_l(\alpha_{opt})|_{rough} \right| \tag{5.4.11}$$

$$CF2_{sens} = \left| \int_{\alpha_{opt}-\sigma_{alpha}}^{\alpha_{opt}+\sigma_{alpha}} [C_l(\alpha)|_{clean} - C_l(\alpha)|_{rough}] \times p(\alpha)\, d\alpha \right| \tag{5.4.12}$$

Similarly to what has been done for $CF1_{LD}$ and $CF2_{LD}$, the cost function which accounts for maximizing the optimal C_l can be written as [54]:

$$CF1_{C_l} = -\left[(1 - MF)\; C_l(\alpha_{opt}) \Big|_{clean} + MF\; C_l(\alpha_{opt}) \Big|_{rough} \right] \tag{5.4.13}$$

$$CF2_{C_l} = -\left[(1 - MF) \int_{\alpha_{opt}-\sigma_{alpha}}^{\alpha_{opt}+\sigma_{alpha}} C_l(\alpha) \Big|_{clean} \times p(\alpha)\, d\alpha + MF \int_{\alpha_{opt}-\sigma_{alpha}}^{\alpha_{opt}+\sigma_{alpha}} C_l(\alpha) \Big|_{rough} \times p(\alpha)\, d\alpha \right] \tag{5.4.14}$$

Although, it can be argued that a larger optimal C_l might lead to larger loads (and load variations) that the wind turbine has to withstand. A 'load-oriented' cost function could be implemented to limit the lift coefficient values in the estimated angle of attack range, resulting in a fairly flat shape. This strategy would alleviate the sensitivity of the Lift coefficient to changes in AoA, resulting in advantages in terms of reduced fatigue damages and more constant load. The fluctuations in the load constitutes a considerable issue in terms of electrical requirements such as frequency and voltage stability, requiring the usage of controllers, to smooth down the electrical load variation and yielding a constant output [56]. The cost function to account for such a requirement can be expressed as:

$$CF_{load} = \left| C_l(\alpha_{opt} + \sigma_{alpha}) - C_l(\alpha_{opt} - \sigma_{alpha}) \right| + \left| C_l(\alpha_{opt}) - C_l(\alpha_{opt} - \sigma_{alpha}) \right| \tag{5.4.15}$$

It should be pointed out that while this latter cost function formulation proved to be effective for a 24 % thick airfoil, the results for the 35% thick airfoil (see APPENDIX B.2.2) suggest that this CF formulation should be improved.

Chapter 6

Results and Discussion

This chapter will discuss the results from the airfoil genetic multi-objective optimization. It has been chosen to limit the airfoil optimization to three different relative thickness values: a 24 $\%\frac{t}{c}$, a 35 $\%\frac{t}{c}$ and an 18 $\%\frac{t}{c}$. In particular, a deeper analysis will be carried out for the 24 % thick airfoil. The reason for this is explained as follows. The contribution to the aerodynamic performance of the wind turbine blade sections increases moving from inboard to outboard stations. On the other hand, the range of expected angle of attack fluctuations will have an opposite trend, decreasing moving from inboard to outboard stations. Since the main CF1 and CF2 are associated to a 'one point design' and to a 'robust design', a blade section which presents relatively large angle of attack fluctuations must be chosen to stress the difference between the two CFs. A 24 % airfoil is detected for about 50 % of the span (for the NREL 5MW wind turbine) and therefore this airfoil will have a good trade-off between the relative importance of that blade section to the overall aerodynamic performance of the blade while keeping a sufficiently large AoA fluctuations range. In addition, it can also be argued that the current trend in wind turbine design is moving towards the use of thicker and thicker airfoils for outboard stations, mainly because the increase in the wind turbine size implies an increase in the aerodynamic loads and larger structural bearing capability is required [55]. The results for the other airfoil thicknesses are shown for completeness of the analysis. Besides, a comparison between the results of the Optiflow simulation for a 24 % thick airfoil and a DU 91 W2-250 airfoil will be performed in section 6.4.

6.1 Optimization set-up

This section will briefly summarize the set-up of the optimization. 50 generations have been considered, where each generation will count a population of 150 individuals. As discussed in section 5.2 the main convergence criteria is based on the distance from the Pareto Front which is accounted for by imposing a Pareto fraction of 60 %. In addition, Optiflow uses the CST parametrization described in section 5.1, which requires the order of the Bernstein polynomials which will be used to parametrize the airfoil geometry. The order of the polynomials has been set to 8, either for the upper and the lower airfoil surface.

The polar curves have been calculated by using RFOIL and assuming a Reynold's number of 9×10^6, which is typical for large horizontal axis wind turbines [54]. RFOIL predicts transition based on the e^n method discussed in section 2.1.4 and the critical amplification factor n has been set to 9. The clean configuration has been evaluated without setting any constraints on the transition point, while, the rough configuration has been evaluated by forcing transition on the upper and lower surface at $\frac{x}{c} = 0.05$ $\frac{x}{c} = 0.1$, respectively. Each polar curve has been calculated for an AoA ranging from -5 ° to 20 ° in steps of 0.2 °. Finally, all the optimizations have been run by employing the probability density function for AoA fluctuations which results from the Onshore scenario analysis, except when specified.

6.2 Optiflow Simulation Results

6.2.1 24 % thick airfoil

This section will discuss the results of the Optiflow simulations for a 24 % thick airfoil, using the cost functions described in section 5.4.1.

The results of the optimization can be observed in Figures 6.1 and 6.2. The figures use a color code to relate the points in the Pareto front to the correspondent airfoil shapes and aerodynamic characteristics. In particular, the points with a large value of CF1 are represented by the color blue while the points with a large value of CF2 are red. Figure 6.2 shows the evolution of the $\frac{C_l}{C_d}$ along the Pareto Front in the clean and rough configuration. For the clean configuration, it can be observed a progressive decrease in the maximum value of the Lift over Drag ratio along with an increase in the width of the curve. This shows that the optimization has worked correctly, because shifting from a point design towards a robust design, the airfoil will have worst performance at the optimal angle of attack but better performance over the estimated range of angle of attack. A different trend can be noticed for the rough configuration, where starting from low values of CF2 and narrow width of the curve, the maximum $\frac{C_l}{C_d}$ is progressively optimized moving towards large values of CF2 and larger width of the curve. In addition, it can be seen that the optimal angle of attack (either in the clean and rough configuration) moves towards larger values moving from blue to red. This evidence should be taken into account when designing airfoils. Indeed, broading up the discussion to the blade design level, a constant angle of attack over the blade span is required, which also means that the designer does not have much room for selecting the optimal angle of attack of each airfoil.

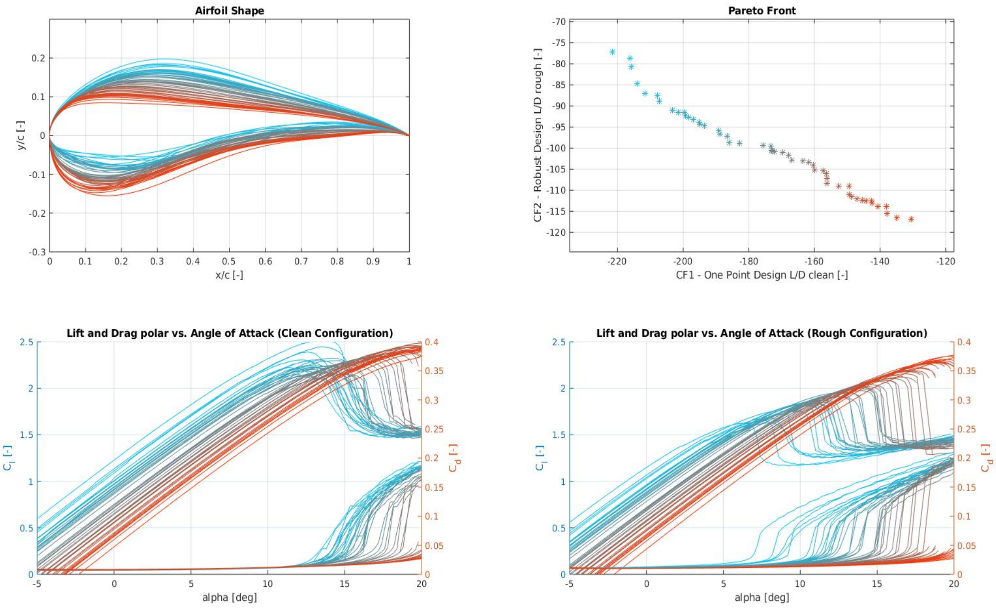

Figure 6.1: *Overview of the simulation result for a 24 % thick airfoil at 50 % of the span, CF1* = $CF1_{LD_{clean}}$ *and CF2* = $CF2_{LD_{rough}}$. *a) airfoil geometry, b) Pareto Front, c) polar curves in the clean configuration and d) polar curves in the rough configuration*

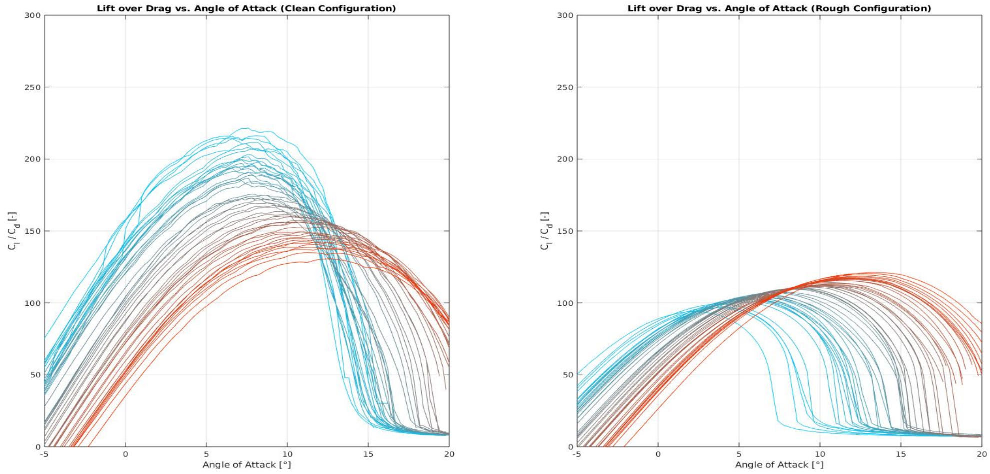

Figure 6.2: *Lift over Drag ratio versus Angle of attack in the clean (a) and rough (b) configuration for a 24 % thick airfoil at 50 % of the span, where CF1* $= CF1_{LD_{clean}}$ *and CF2* $= CF2_{LD_{rough}}$

In order to better evaluate the airfoil candidates Figure 6.3 and 6.4 are presented, where three relevant airfoils from the airfoil family (shown in Figure 6.1) along with the correspondent polar curves, $\frac{C_l}{C_d}$ and transition points on the suction and pressure side are plotted. The blue line corresponds to the airfoil candidate with the largest value of CF1, the red line to the airfoil candidate with the largest value of CF2 and the green line to a 50/50 compromise between CF1 and CF2. Regarding geometry, these three airfoils present different features and in particular, moving from blue to red, the location of the maximum thickness shifts towards lower values of $\frac{x}{c}$ along with a decrease in the camber. The effect of the decrease in the camber can be directly seen in the shift of the Lift polars, where the minimum angle of attack at which Lift is produced progressively increases.

Still regarding geometry, it can be observed that the three airfoils present an s-shaped lower surface tail while the blue airfoil additionally shows a sharp LE nose, in contrast with what can be seen for the other two airfoils. An s-shaped lower surface is desired in order to increase the aft-loading, which results in larger lift generated. This can be explained by thinking that if the lower surface thickness in the aft region decreases, the area where the fluid can flow increases and consequently velocity will decrease. For the Bernoulli's principle, a reduction of velocity is accompanied by an increase in pressure. A larger pressure on the lower surface will generate more Lift (this can also be observed by looking at the polar curves). A sharp LE nose is desired in order to promote an earlier transition and consequently delaying separation. However, it can be noticed that the red airfoil, which shows the larger LE curvature radius, also presents the earlier transition location on the upper surface. By comparing the geometry of the blue and red airfoils it can be seen that the location of the maximum upper thickness is around $\frac{x}{c} = 0.1$ and $\frac{x}{c} = 0.3$ for the red and blue airfoil, respectively. Since the airflow on the upper surface will be accelerated up to the point of maximum thickness, the maximum velocity (suction peak) will be found at different $\frac{x}{c}$ locations for the red and blue airfoil. The Stratford's criteria [54], estimates the effective BL length ($x^{'}$) when transition occurs depending on the history of the development of the boundary layer and in particular according to the effective BL length when the suction peak occurs, and depending on the location (x) of transition and of the suction peak, according to $x^{'}_{transition} = x^{'}_{lam_{suction}} + [x_{transition} - x_{suction}]$. This means that the earlier the suction peaks occurs, the earlier the flow will transit from laminar to turbulent. This argument can justify the earlier transition point for the red airfoil with respect of the blue airfoil. The presented discussion stresses the fact that the red airfoil geometry can be very effective for anticipating transition. Although, it must be pointed out that the red airfoil shows an optimal angle of attack of around 14°, which is much larger than typical values for wind turbine applications (between 5 and 7°). Airfoils with such a large optimal AoA could have the drawback, that, when operating at low AoAs, separation might occur on the lower surface and moreover, the values of C_l are really low. This means that the 'strategy' through which the early transition location is achieved for the red airfoil is not suited for wind turbine operations where a low optimal angle of attack is required and consequently, a sharp LE should still be adopted.

Regarding the aerodynamic characteristics, it should be pointed out that the difference between the optimal AoA and the stall AoA, progressively increases moving from blue to red, and in particular, for the latter, stall is not detected for AoA $< 20°$. This means that the probability of reaching stall decreases moving from the blue to the red airfoil. In addition, by comparing the clean and rough polars, it can be noticed that the roughness insensitivity is best for the red airfoil. All these considerations suggest that, the optimal solution for wind turbine applications will not be the one that maximizes the CF1 or the CF2, but it will be found somewhere in between. Indeed, by looking at the green airfoil's aerodynamic characteristics, it can be observed that it shows a good trade off between $\frac{C_l}{C_d}$, distance between the AoA_{opt} and the AoA_{stall} and roughness insensitivity.

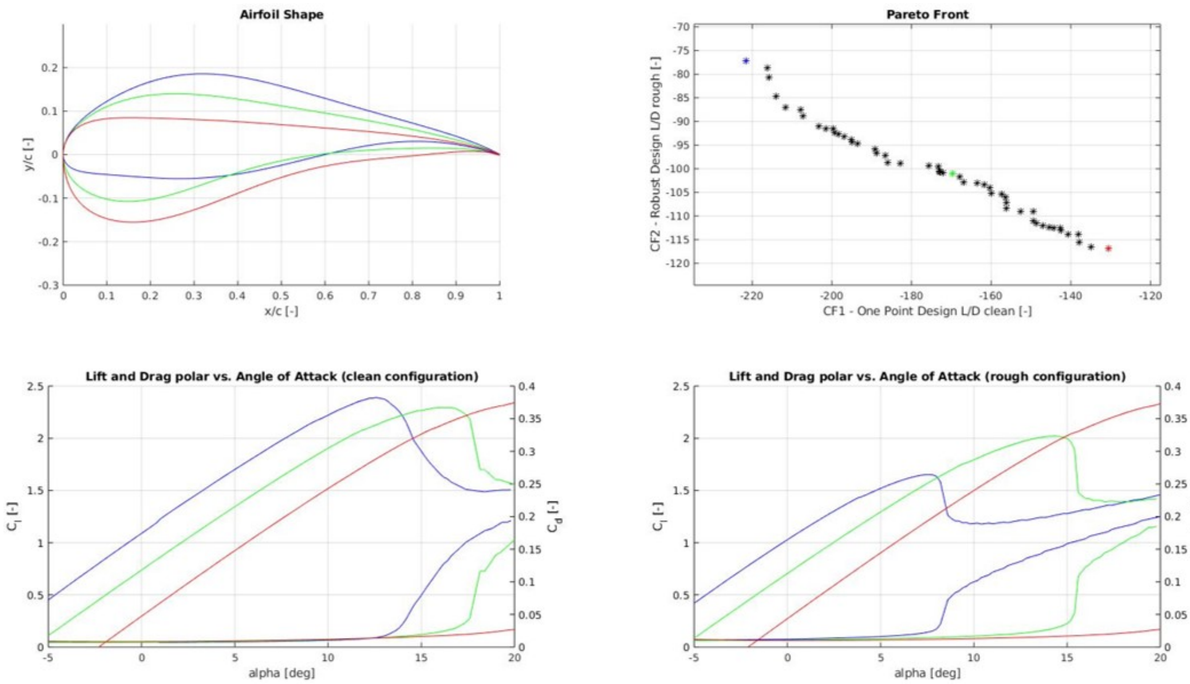

Figure 6.3: *(a) Airfoil shapes and (b) correspondent polar curves for a 24 % thick airfoil. The blue line correspond to the airfoil with largest value of CF1, the red lines to an airfoil with largest values of CF2 and the green lines to a 50-50 compromise between CF1 and CF2.*

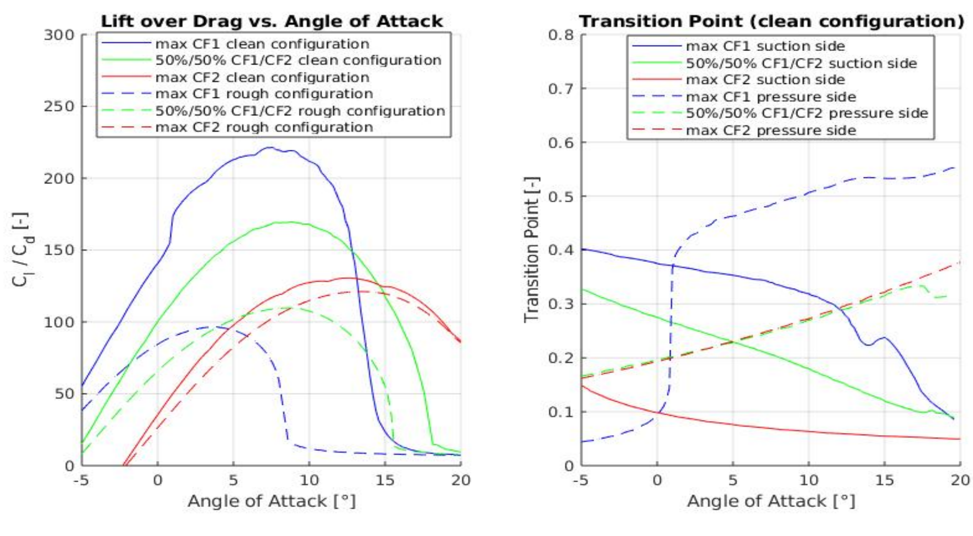

Figure 6.4: *(a) Airfoil shapes and (b) correspondent polar curves for a 24 % thick airfoil. The blue line correspond to the airfoil with largest value of CF1, the red lines to an airfoil with largest values of CF2 and the green lines to a 50-50 compromise between CF1 and CF2.*

6.2.2 35 % thick airfoil

Similarly to what has been done for a 24 % thick airfoil, the results of the optimization for a 35 % thick airfoil, evaluated by a CF1 = $CF1_{LD_{clean}}$ and a CF2 = $CF2_{LD_{rough}}$, are presented in Figure 6.5 and 6.6 (results using alternative CFs can be found in APPENDIX B.2).

As far as the airfoil geometry is concerned, the same general trend, with respect of the results for the 24% thick airfoil can be observed, meaning that moving from blue to red, the airfoil camber decreases, along with a reduction of the upper thickness and an increase in the lower thickness (to meet the design thickness). This tendency will again result in shift in the Lift polar and in a similar trend for the transition location, for the reasons explained in the previous section.

Regarding the aerodynamic characteristics in the clean configuration, it can be observed that the stall angle of attack of the three airfoils is comparable, while, in the rough configuration, it consistently differs. By looking at the transition location on the suction side at the stall angle of attack, it can be noticed that stall takes place when the transition point is located around the maximum upper thickness. In the rough configuration, the transition location on the upper surface is fixed at $\frac{x}{c} = 0.05[-]$. This means that if transition is promoted too early for the blue and the green airfoil, the combination of favourable and adverse pressure gradient caused by the shape of the upper surface results in an earlier flow separation and consequently those airfoil will stall earlier than the red one. This can be further explained by noticing that the transition location in the clean configuration of the red airfoil is closer to the $\frac{x}{c} = 0.05[-]$ threshold, which is also why the roughness insensitivity is best for the red airfoil. However, in general terms, poor roughness insensitivity performance are detected for the three airfoils. This evidence suggests that for inboard stations, the cost function should be implemented in order to enforce the roughness insensitivity requirement.

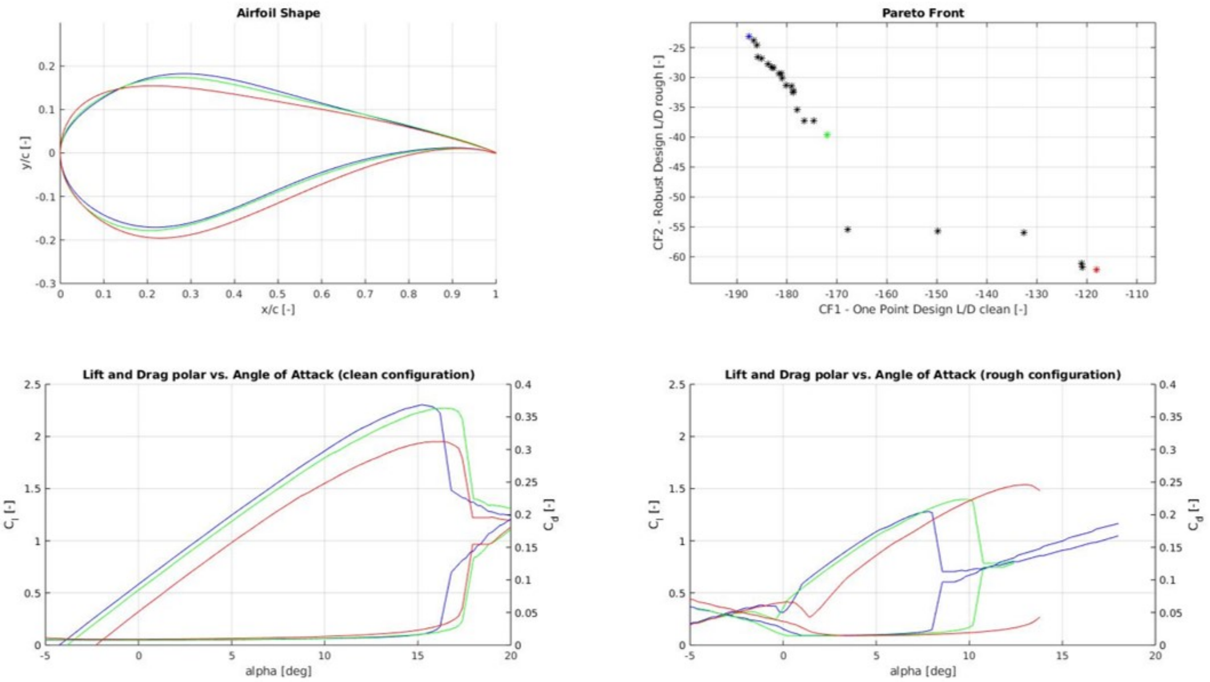

Figure 6.5: *Overview of the simulation result for a 35 % thick airfoil at 30 % of the span, where CF1 =* $CF1_{LD_{clean}}$ *and CF2 =* $CF2_{LD_{rough}}$*. a) airfoil geometry, b) Pareto Front, c) polar curves in the clean configuration and d) polar curves in the rough configuration*

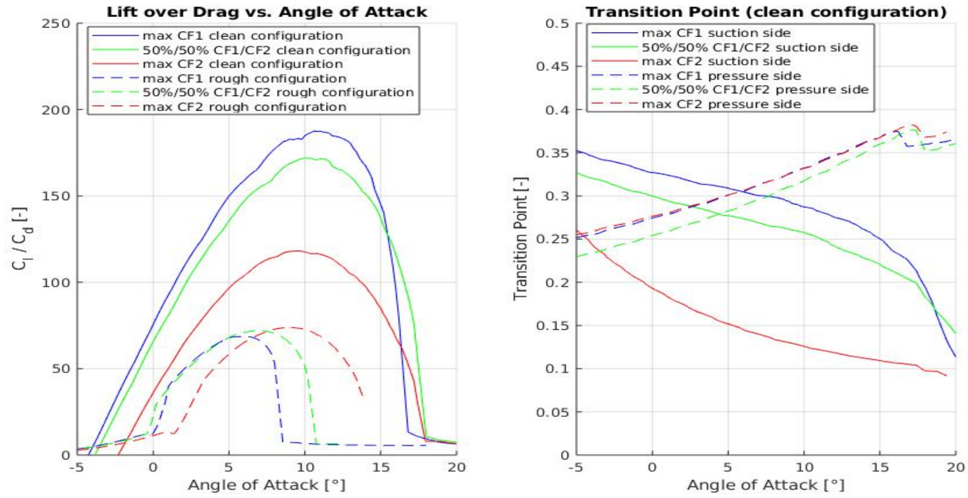

Figure 6.6: *Overview of the simulation result for a 35 % thick airfoil at 30 % of the span, where CF1 =* $CF1_{LD_{clean}}$ *and CF2 =* $CF2_{LD_{rough}}$*. a) L over D in the clean and b) rough configuration*

6.2.3 18 % thick airfoil

The results for an 18 % thick airfoil located at 70 % of the span for the NREL 5 MW machine are presented in Figure 6.8 and 6.7. With respect of the previous optimizations, the interval of the CF2 values is narrower. This can be explained by thinking that the range of angle of attack fluctuations is smaller, and consequently the difference between the values of CF1 (one point design) and CF2 (robust design) becomes smaller as well. In general terms, these results are very similar to the 24 % relative thickness case except for the transition locations for the three airfoils on the pressure side. Regarding the lower surface transition location of the blue airfoil, it can be noticed a weird trend in the interval $13° < AoA < 15°$, where the transition location drastically changes from 0.4 to 1 and back to 0.4. As already discussed, the transition location is calculated considering the history of the development of the boundary layer and in particular depending on the combination of favourable and adverse pressure gradient experienced by the BL. No physical explanation has been found to describe the peak shown in the graph and it might be possible that it is due to an art-effect of RFOIL. As far as the red airfoil transition location for large angles of attack, the flow is always laminar. By looking at the lower surface shape of the red airfoil, the laminar flow behavior can be explained by thinking that at that AoAs, the pressure gradient on the lower surface is always favourable and consequently the flow will not transit into the turbulent regime.

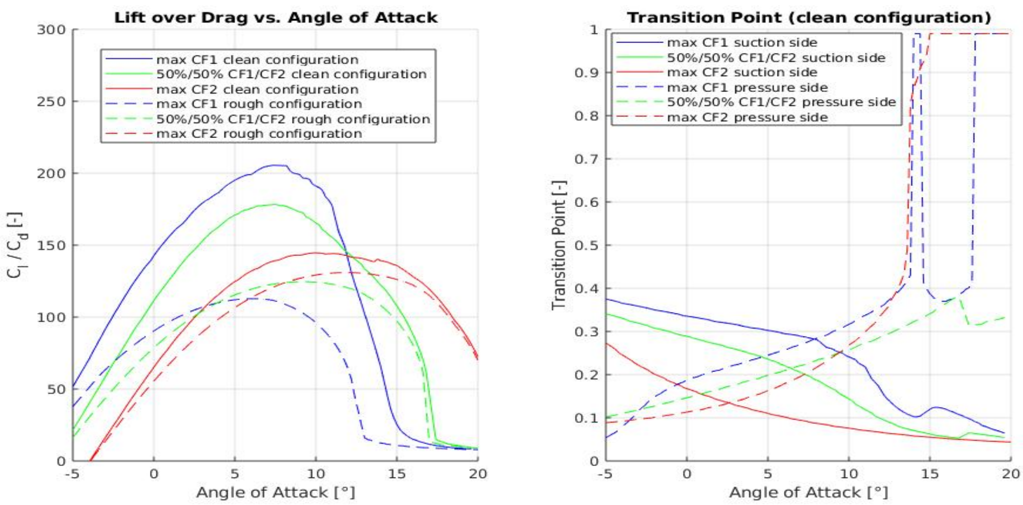

Figure 6.7: *Overview of the simulation result for an 18 % thick airfoil at 70 % of the span, where CF1 =* $CF1_{LD_{clean}}$ *and CF2 =* $CF2_{LD_{rough}}$*. a) L over D in the clean and b) rough configuration*

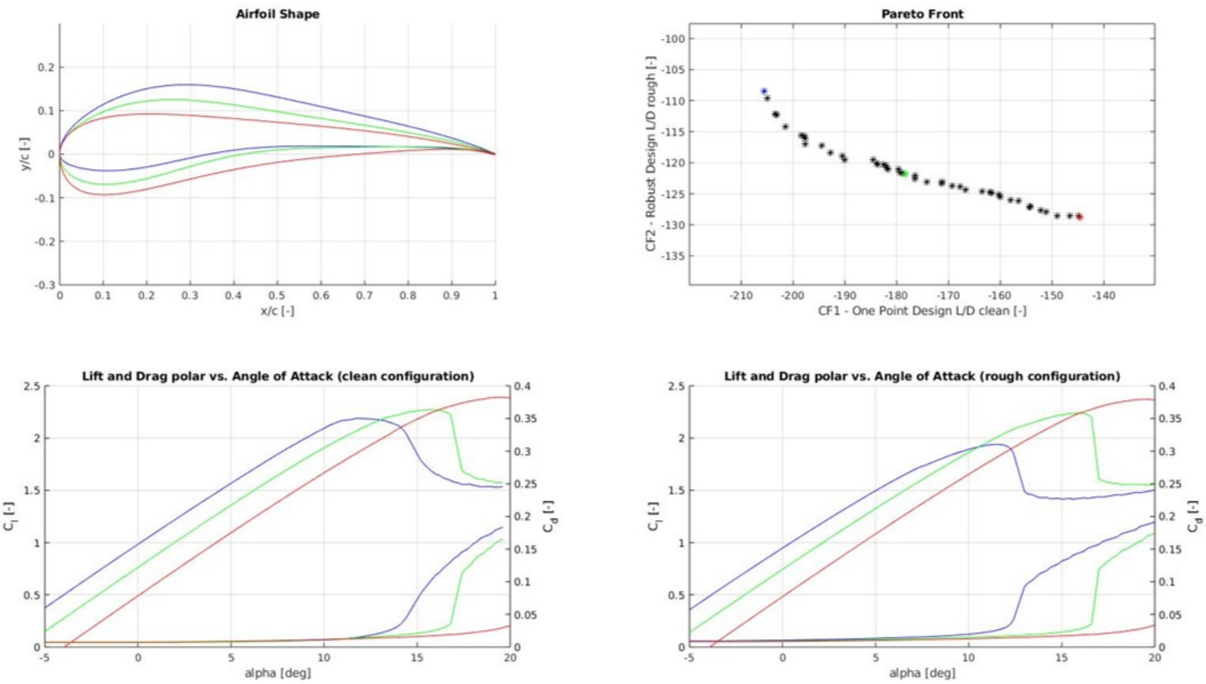

Figure 6.8: *Overview of the simulation result for an 18 % thick airfoil at 70 % of the span, where CF1 =* $CF1_{LD_{clean}}$ *and CF2 =* $CF2_{LD_{rough}}$. *a) airfoil geometry, b) Pareto Front, c) polar curves in the clean configuration and d) polar curves in the rough configuration*

6.3 Results with Alternative CFs for a 24% thick airfoil

As discussed in section 5.4.3, several cost functions can be used in order to design wind energy airfoils. The results of section 6.2 shows that, for a 24 % thick airfoil, compromising between a maximum $\frac{L}{D}$ in clean and rough configuration, along with using a 'point design' CF1 and a 'robust design' CF2, leads to fairly balanced solutions in terms of aerodynamic efficiency, large C_l, roughness insensitivity and broad interval between AoA_{opt} and AoA_{stall}. For these reasons, these requirements have not been enforced in the cost functions. This section aims to test what is the impact on the airfoil geometry when different CFs are used.

6.3.1 Modification of the main Cost Function

In this section, a similar optimization to the one carried out in section 6.2.1 will be performed, using the CF1 = $CF1_{LD}$ and CF2 = $CF2_{LD}$ described in section 5.4.3. The results are presented in Figure 6.9 and 6.10. The first thing that should be observed is the very narrow interval of the two CFs in the Pareto front, which is reflected by very small variations in the airfoil geometries. This should be mainly due to the choice of the CFs which present comparable outcomes, as discussed in section 5.4.3. For this reason, it has been decided to plot only three airfoils from the original airfoil family, for the sake of clarity. The color blue has been used for the airfoil candidate which maximizes the CF1, the red airfoil is the one that maximizes the CF2 while the green airfoil is taken as a 50/50 compromise between CF1 and CF2.

The airfoil shapes show the typical characteristics of wind energy airfoils, presenting a s-shaped lower surface tail and a relatively sharp leading edge nose. The location of the maximum thickness, with respect of the previous optimizations, is shifted in the downstream direction and the upper and lower thickness distribution is more uniform. This characteristics should imply that the flow will be subject to a weaker adverse pressure gradient. This evidence might justify the better roughness insensitivity of these airfoils with respect of the previous optimizations.

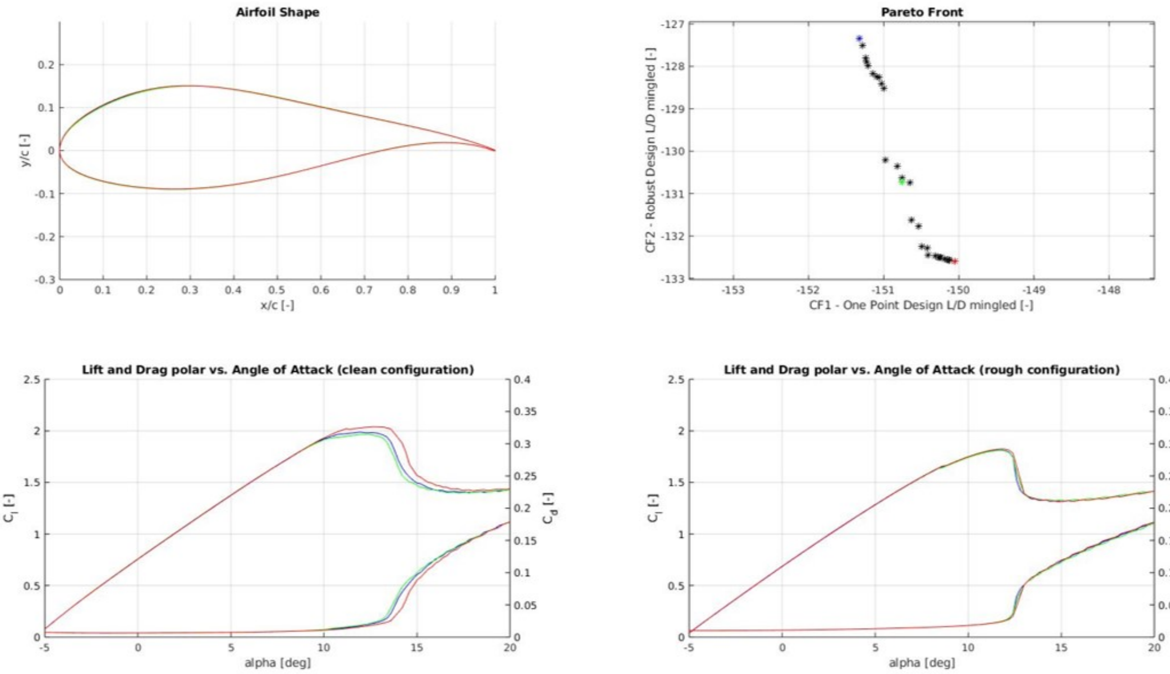

Figure 6.9: *Overview of the simulation result for a 24 % thick airfoil at 50 % of the span, where CF1* $= CF1_{LD}$ *and CF2* $= CF2_{LD}$*. a) airfoil geometry, b) Pareto Front, c) polar curves in the clean configuration and d) polar curves in the rough configuration*

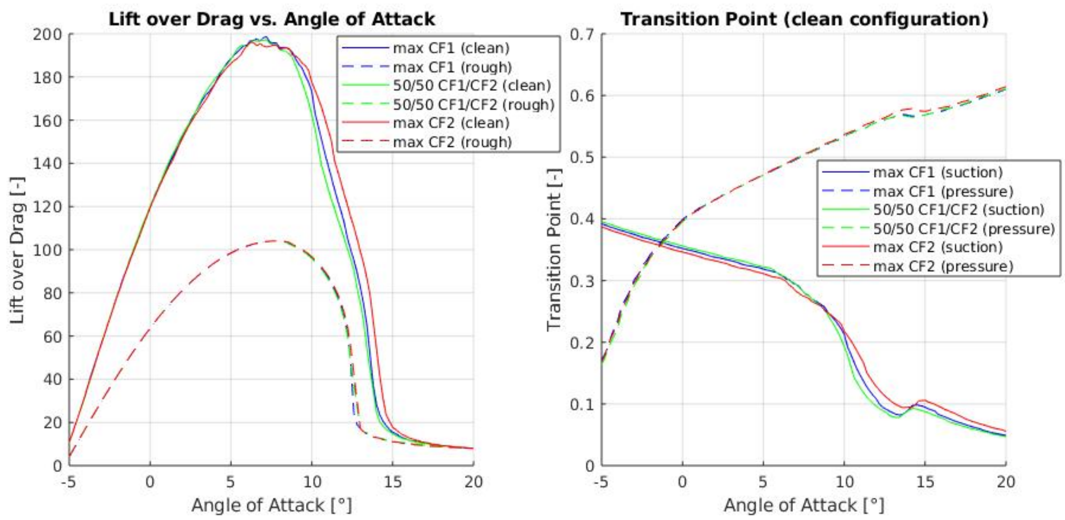

Figure 6.10: *Overview of the simulation result for a 24 % thick airfoil at 50 % of the span, where CF1* $= CF1_{LD}$ *and CF2* $= CF2_{LD}$*. a) L over D in the clean and b) rough configuration*

6.3.2 Influence of the probability of angle of attack fluctuations on airfoil geometry

In this section it is wanted to test what is the impact of choosing different probability of angle of attack fluctuations on the resultant airfoil geometry. In order to do so, the same optimization performed in the previous section will be run, but this time, the pdf which results from the Offshore installation site analysis will be used, rather than the one for the Onshore site. In this case, no large variations are expected, because the only difference in the two optimizations would be the smaller angle of attack operational range, mainly due to the lower turbulence intensity values, for the offshore site. This can be seen in Figure 6.11, which shows the airfoil shapes, the correspondent polar curves and transition points on the upper and lower surface. As expected, the two airfoils candidate show a similar geometry and the LE nose shape is one of the main differences.

Regarding the airfoil geometry, the maximum lower surface thickness is very close to the LE (for the offshore airfoil) which can justify the earlier transition location on the lower surface for low angles of attack. The very similar upper surface shape justifies the very small difference in terms of transition location on the upper surface. Finally, it can be observed that from the point of maximum thickness on, the offshore airfoil is thinner than the onshore airfoil. This lower thickness should cause a weaker adverse pressure gradient, which might be the reason for the larger stall angle for the offshore airfoil with respect of the onshore one.

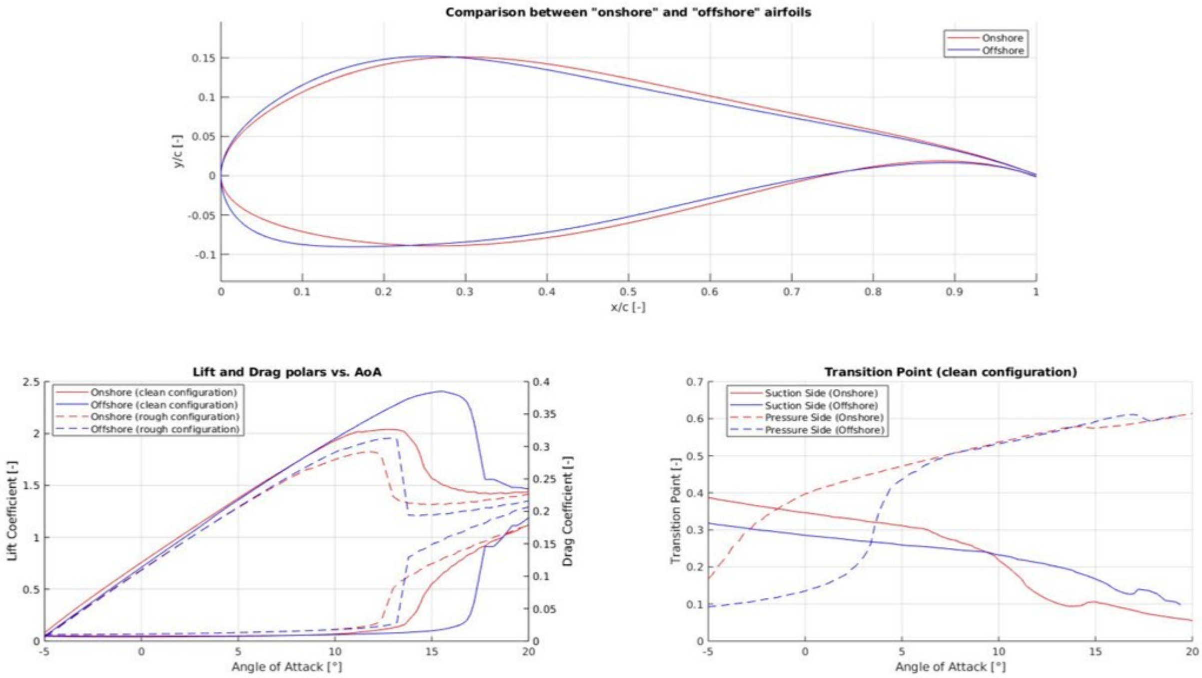

Figure 6.11: *Comparison between the simulation result for a 24 % thick airfoil at 50 % of the span, using the Onshore and Offshore pdf, where CF1 =* $CF1_{LD}$ *and CF2 =* $CF2_{LD}$*. a) airfoil geometry, b) polar curves in the clean and rough configuration and c) transition point in the clean configuration*

6.3.3 Load-oriented optimization

As discussed in section 5.4.3, a load-oriented optimization can be performed in order to limit the maximum values of the Lift coefficient in the estimated operational range of angles of attack, in order to decrease maximum aerodynamic load and to decrease the load fluctuations. This can be done by using a CF1 = CF_{load} and a CF2 = $CF2_{LD}$ and the results are plotted in Figure 6.12 and 6.13. It must be pointed out that some airfoils have been excluded from the Pareto front because of very poor performance or low manufactural feasibility and for the sake of clarity.

Regarding the aerodynamic characteristics, it can be seen how the goal of having a flat polar curve over the operational range of angle of attack is achieved for the blue airfoils, which present the unique characteristics of thick trailing edges along with a minimum thickness location in the mid-chord position. The fact that the minimum thickness is reached for a mid-chord location, implies that the flow is accelerated in two steps, first by the leading edge and subsequently from the point of minimum thickness up to about 80% of the chord. Of course, this comes at the expense of large $\frac{C_l}{C_d}$ which are best for the red airfoils. The red airfoils present a similar shape with respect of the results of the previous optimizations, but the thickness of the TE is larger than for the previous case, mainly due to the set-up of the optimization. For a better evaluation, Figure 6.14 is included, where only three airfoils have been selected and plotted along with the correspondent polars. In this case, the optimal angle of attack (dash-dot line) and the angle of attack range (dashed lines) can be directly seen in the figure, which allows to see how the lift coefficient for the blue airfoil will be fairly constant for positive variations in angle of attack while it will decrease with a lower slope (than for the red and green airfoils) for negative variations in AoA.

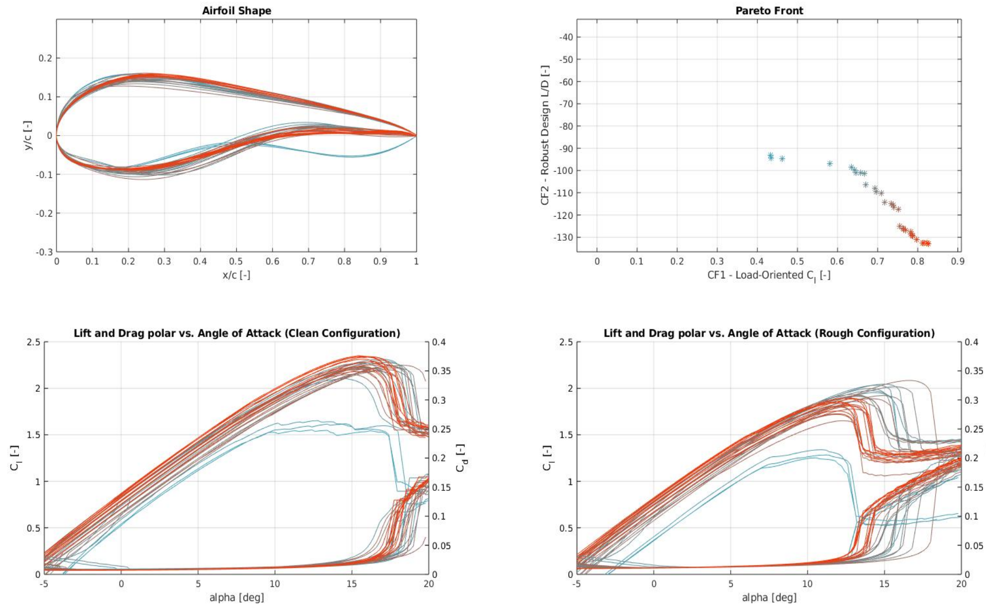

Figure 6.12: *Overview of the simulation result for a 24 % thick airfoil at 50 % of the span, where CF1 =* CF_{load} *and CF2 =* $CF2_{LD}$. *a) airfoil geometry, b) Pareto Front, c) polar curves in the clean configuration and d) polar curves in the rough configuration*

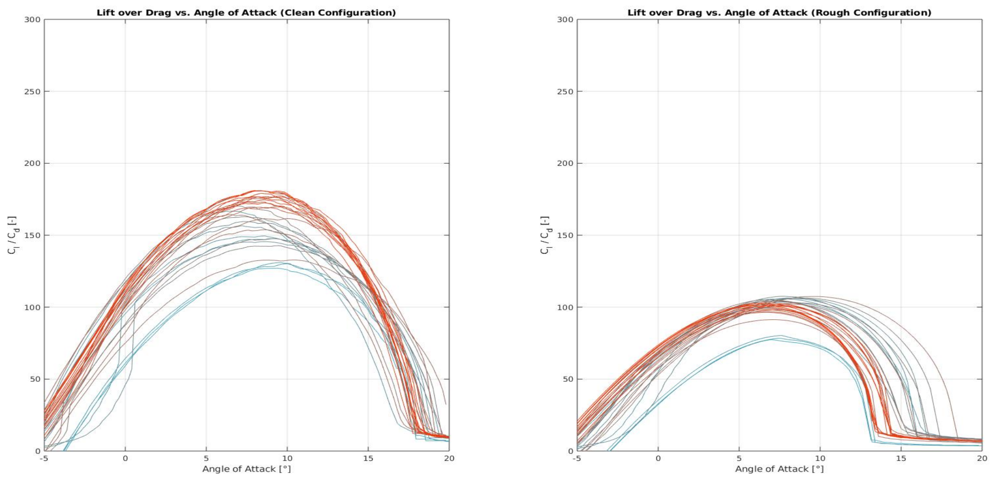

Figure 6.13: *Overview of the simulation result for a 24 % thick airfoil at 50 % of the span, where CF1 =* CF_{load} *and CF2 =* $CF2_{LD}$. *a) L over D in the clean and b) rough configuration*

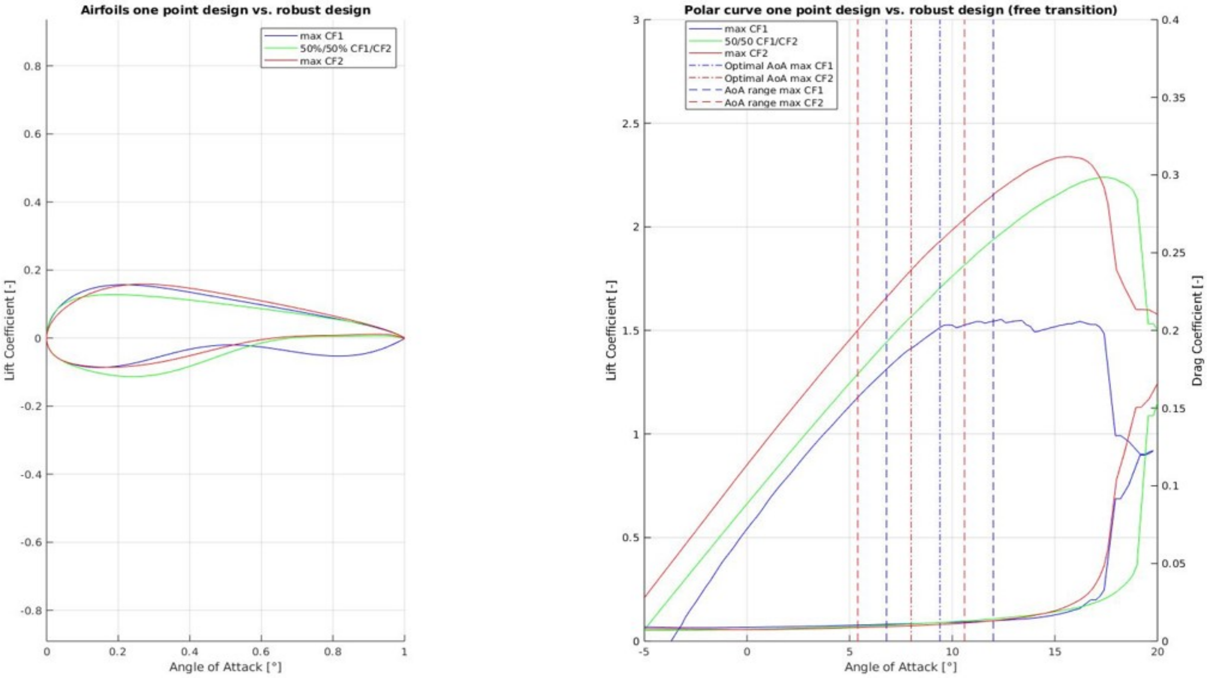

Figure 6.14: *Overview of the simulation result for a 24 % thick airfoil at 50 % of the span, where CF1 =* CF_{load} *and CF2 =* $CF2_{LD}$*. a) airfoil geometry, b) polar curves in the clean configuration*

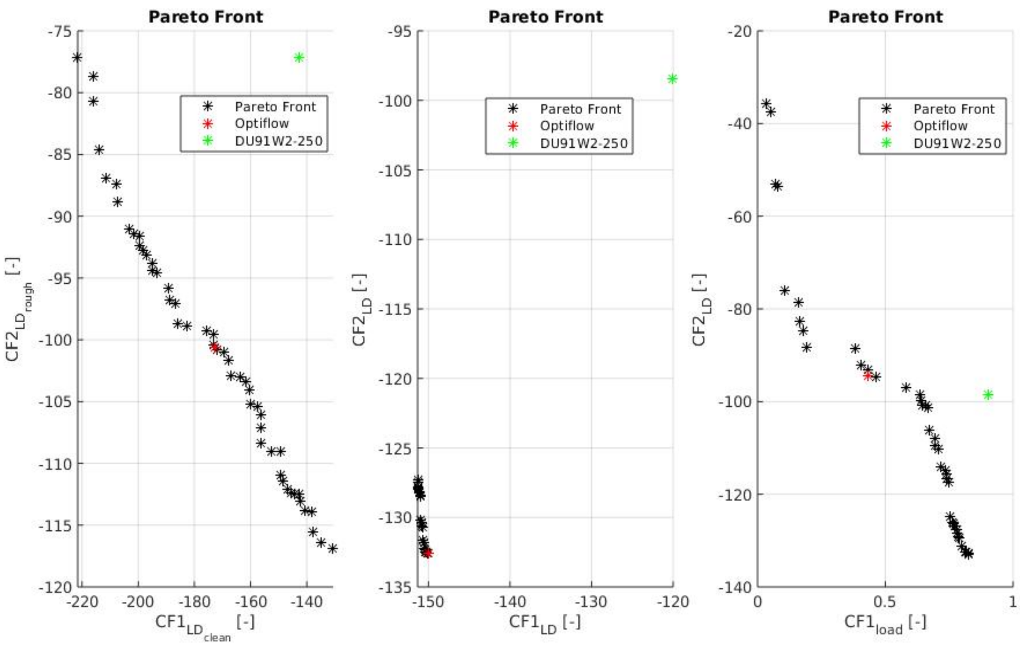

Figure 6.15: *Comparison between the Pareto Front of the 25 % thick DU91W2-250 airfoil and the 24 % thick airfoil obtained with Optiflow using a CF1 =* $CF1_{LD_{clean}}$ *and CF2 =* $CF2_{LD_{rough}}$ *a), CF1 =* $CF1_{LD}$ *and CF2 =* $CF2_{LD}$ *b) and CF1 =* $CF1_{load}$ *and CF2 =* $CF2_{LD}$ *c)*

It would seem that airfoils which presents a large TE thickness and a 'w-shaped' lower surface are suitable for a load-oriented goal. Although, such a shape would result in larger Drag and lower Lift values, having the drawback of reduced maximum efficiency and performance. Such a design might be more effective for inboard airfoils. Inboard stations have a lower contribution to the overall aerodynamic performance, so the decreased performance problem should be mitigated, and moreover they present the largest angle of attack fluctuation range and the largest influence of the unsteady effect, which means larger deviation from the quasi-steady polar curves behavior. These arguments suggest that inboard stations are better suited for load-control purposes.

6.4 Comparison with a DU91W2-250 airfoil

In this section, the main results of the previous optimizations for the 24% thick airfoil will be compared with the DU 91 W2-250 airfoil. It must be pointed out that the DU airfoil has a 25% thickness, consequently the comparison will be affected by this small difference. Figure 6.15 shows the the Pareto front of the Optiflow optimizations where the two airfoils that will be compared in this section are highlighted with the color red (Optiflow) and green (DU91W2-250).

6.4.1 Main Cost Function

In this section, the green airfoil shown in Figure 6.3 will be compared with the DU91W2250 airfoil, as can be seen in Figure 6.16. The two airfoils are quite different from each other, in particular, regarding geometry, a different thickness distribution and LE nose shape can be noticed. As already discussed, the more pronounced lower surface s-shaped tail for the red airfoils will make the C_l values to be larger than for the DU airfoil, although, the roughness sensitivity is increased.

Regarding the aerodynamic characteristics it can be noticed that for AoA $> 7°$ the transition point location for the DU airfoil is about 5% of the chord, which makes sense since the aerodynamic polar in the clean configuration matches the one in rough configuration where transition is forced to occur at that chord-wise position. This allows a very good roughness insensitivity and gentle stall, but the stall angle of attack occurs earlier than for the red airfoil, which also shows a broad interval between optimal and stall AoA (about 9 and 7° in the clean and rough configuration respectively).

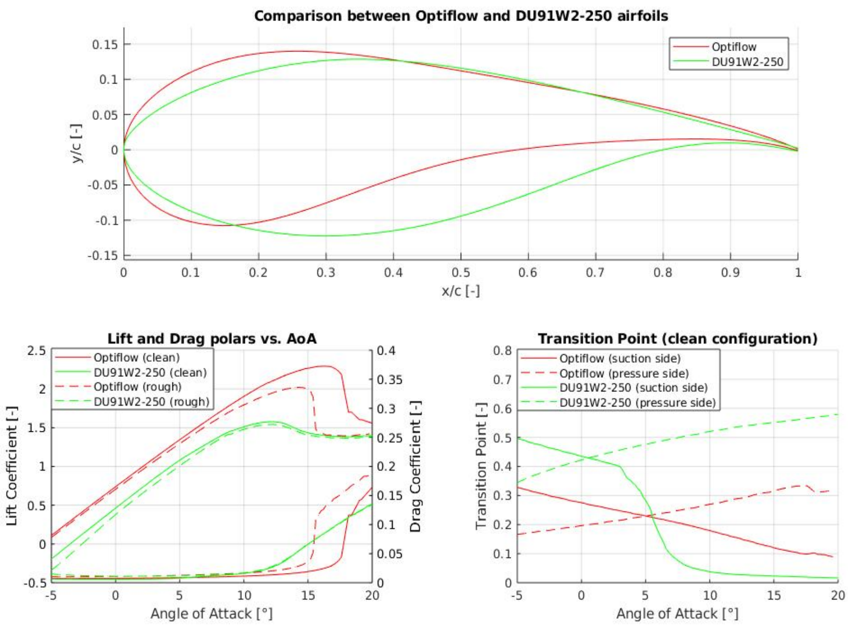

Figure 6.16: *Comparison between the 25 % thick DU91W2-250 airfoil and the 24 % thick airfoil obtained with Optiflow using a CF1 =* $CF1_{LD_{clean}}$ *and CF2 =* $CF2_{LD_{rough}}$*. a) airfoil geometry, b) polar curves in the clean and rough configuration and c) transition point on the upper and lower surface in clean configuration*

6.4.2 Modification of the Main Cost Function

In this section, the green airfoil shown in Figure 6.9 will be compared with the DU91W2250 airfoil, as can be seen in Figure 6.17. In this case, the two airfoil geometries are quite similar to each other, and the main difference is the larger camber of the red airfoil with respect of the DU airfoil, which directly results in a shift in the polar curve, allowing to reach larger Lift values for smaller angles of attack. It can also be observed that a similar LE nose shape results in a similar stall angle of attack for the red and the DU airfoil. Moreover, the maximum thickness for the DU airfoil is located more downstream than for the red airfoil, which, also considering the lower camber, might be the reason for the better roughness insensitivity achieved by the DU airfoil. This suggest that airfoils with a low camber along with a maximum thickness location between $0.3 < \frac{x}{c} < 0.4$ are best for such a requirement.

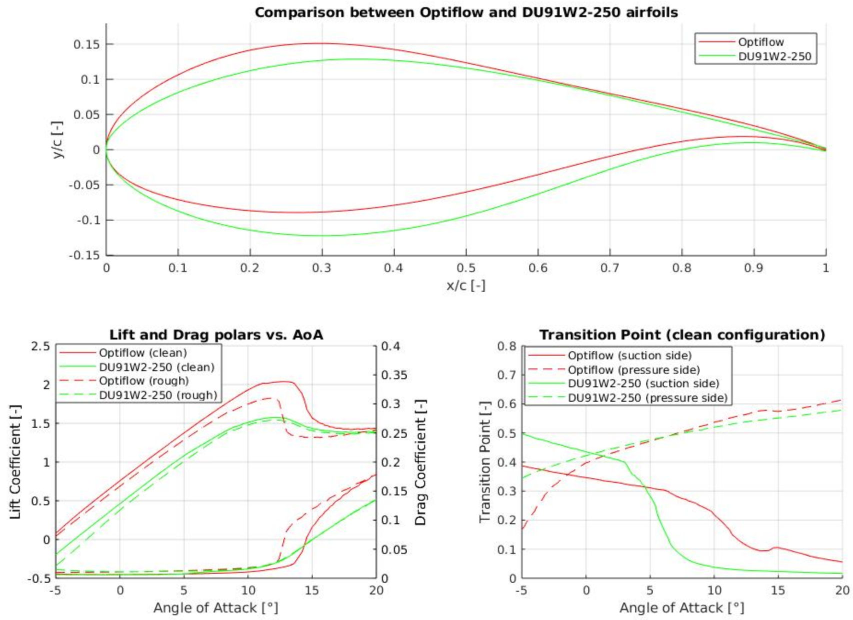

Figure 6.17: *Comparison between the 25 % thick DU91W2-250 airfoil and the 24 % thick airfoil obtained with Optiflow using a CF1 =* $CF1_{LD}$ *and CF2 =* $CF2_{LD}$*. a) airfoil geometry, b) polar curves in the clean and rough configuration and c) transition point on the upper and lower surface in clean configuration*

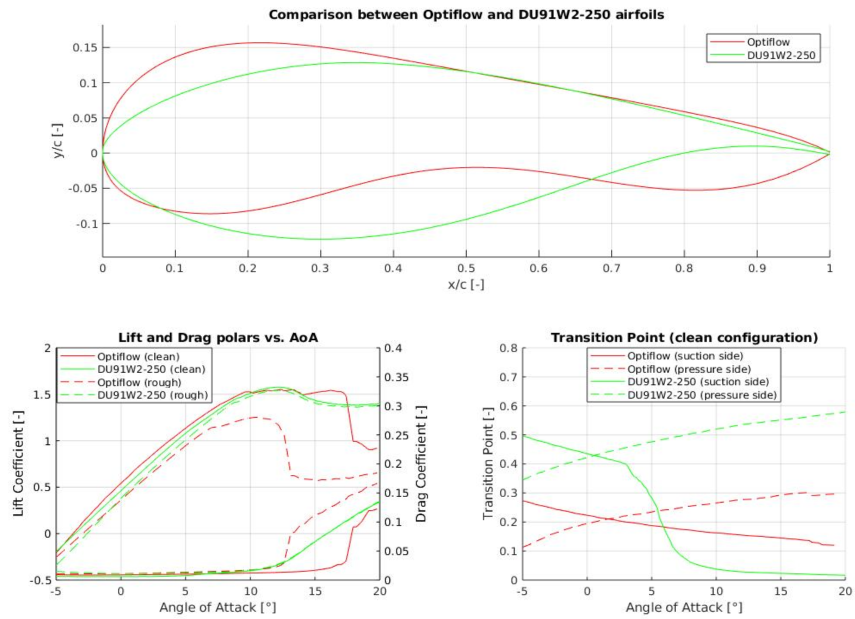

Figure 6.18: *Comparison between the 25 % thick DU91W2-250 airfoil and the 24 % thick airfoil obtained with Optiflow using a CF1 =* CF_{load} *and CF2 =* $CF2_{LD}$*. a) airfoil geometry, b) polar curves in the clean and rough configuration and c) transition point on the upper and lower surface in clean configuration*

6.4.3 Load-oriented Cost Function

This section compares the airfoil obtained throughout the load-oriented optimization with the DU91W2250 as can be seen in Figure 6.18. It is interesting to notice that, in clean configuration, the two very different airfoils shapes generate a very similar polar curve (up to AoA $= 14°$). Although, in rough configuration the aerodynamic performance are way worst for the red airfoil, suggesting that increasing the TE thickness along with a 'w-shaped' lower surface might not be the best solution in order to obtain a flat Lift polar.

Chapter 7

Conclusions

This thesis presented a probabilistic approach to design airfoils for HAWT. Starting from the description of the analytical model which is used to estimate the AoA fluctuations (depending on wind turbine operational parameters), the operational parameters which are relevant for HAWT have been studied and the probability of occurrence of each combination of operational parameters has been estimated. A verification of the probabilistic approach has been carried out by comparing the analytical model predictions with numerical results. Finally, the impact of the probabilistic approach on the airfoil design has been evaluated. The conclusions of the thesis will be discussed in section 7.1 and future recommendations will be provided in 7.2.

7.1 Lesson Learned

This work focused on the study of the variations of the angle of attack due to atmospheric non-uniform perturbations in the wind velocity and to the stochastic nature of turbulence. A good estimation of the angle of attack range experienced during wind turbines operations might result in a more efficient airfoil design, because it would allow to weight the airfoil aerodynamic performance based on the probability of occurrence of each AoA. This approach is believed to be more 'robust' than the 'point-design' approach where the aerodynamic performance are optimized at the optimal angle of attack, at which the airfoil will never constantly operate. In particular, the atmospheric perturbation sources which have been accounted for in the model are: wind shear, yaw misalignment and turbulence intensity. While wind shear and yaw misalignment can be addressed in a deterministic way, a probabilistic approach is needed to include turbulence and this is the reason why the term 'probabilistic' arises in this work.

The results of the **probabilistic approach** show that:

- Regarding wind shear, the fluctuations of the AoA have an increasing trend moving from inboard to outboard stations; this is mainly due to the larger difference between the wind speeds experienced over a revolution for an outboard station rather than an inboard station;
- Regarding yaw misalignment and turbulence intensity, the fluctuations of the AoA decrease moving from root-sections towards tip-sections. This is mainly due to the increasing trend of the tangential component of the relative velocity seen by the airfoil moving towards outboard stations, which makes the angle of attack progressively less sensitive to fluctuations. It must be pointed out that the probabilistic approach assumes the blade to be infinitely stiff. The effect of blade vibration on the relative wind speed seen by the airfoil is more acute towards outboard stations, which means that especially for wind speeds close to rated, the AoA fluctuations might increase moving towards blade tip sections;
- When all perturbation sources are combined, the AoA fluctuations show a decreasing trend moving from inboard towards outboard stations, suggesting that wind shear has a low impact overall.

A probabilistic design space mapping has been performed in order to relate the probabilistic approach outcomes with the airfoil design process. Namely, it has been evaluated what perturbation source has the largest impact on the AoA fluctuations and how likely a certain combination of perturbation sources can occur in practice. Three scenarios have been considered, namely Onshore, Near-Coastal and Offshore; for each scenarios different combination of operational parameters have been evaluated. The results of the **probabilistic design space mapping** show that:

- Turbulence intensity is dominant and, as such, the largest the turbulence intensity the largest the angle of attack fluctuations will be;
- On average, the Onshore scenario shows larger fluctuations of the AoA than the Offshore scenario, which makes sense since larger turbulence intensity values are expected for an Onshore location;
- The probability of occurrence of each combination of operational parameters has been obtained by combining the probability of occurrence of yaw misalignment angle, wind speed and the conditional probability of turbulence intensity given the wind speed; these probability density functions have been obtained by a fit of real data. It can be concluded that cases with large yaw angles (e.g. 20°) have a the lowest probability of occurrence; on the other hand, the largest probability of occurrence has been found for cases with moderate tip speed ratios (e.g. 4-5[-]) and relatively low values of turbulence intensity (e.g. 0.10-0.12 [-]). This can be attributed to the conditional probability of turbulence intensity to occur given the wind speed.

In order to evaluate the accuracy of the predictions of the angle of attack fluctuations range done by the model, a verification has been carried out using an aero-elastic simulation tool (FAST). Each single perturbation source modelling has been verified individually for different blade sections, ranging from 0.2 to 1 [-] and for different wind speeds (from 5 to 17 $\frac{m}{s}$ in steps of 4 $\frac{m}{s}$). Subsequently, the effect of combining perturbation sources has been verified, according to the typical HAWT operational parameters used in the probabilistic design space mapping, for the Onshore, Near-Coastal and Offshore location. The results of the **verification** shows that:

- Regarding wind shear, the analytical model is able to reproduce the trend of the angle of attack fluctuations (with respect to the blade span and wind speed) with a comparable magnitude. A better agreement has been found for large values of terrain roughness.
- Regarding yaw misalignment, the model follows the trend of the angle of attack fluctuations (with respect to the span and wind speed). The largest mismatch between the analytical and numerical results is found for large wind speeds and for outboard stations which can be justified by the analytical modelling of the axial induction factor, which proves not to be accurate at large span-wise fractions and for large wind speeds. The numerical and analytical results have also been compared with an empirical model, which shows that a better estimation of the axial induction factor (for large wind speeds) results in a better agreement with the numerical results. In addition, it has been found that neglecting the unsteady effects contributes to the difference between the analytical predictions and numerical results while, since wind speed is assumed to be steady, the effects of the blade vibrations are not large.
- Regarding turbulence intensity, a fair agreement between analytical and numerical results has been observed, even though the results of the analytical results shows a steeper evolution of the AoA fluctuations with respect of the span than the numerical results. The reason for this can be attributed to neglecting the effect of turbulence in the lateral and vertical direction as well as assuming an infinite stiffness of the blades.
- The combined effect of the perturbation sources modelling shows a very good agreement between the analytical model predictions and the numerical results. The largest difference is found for cases with large yaw misalignment. Although, recalling that cases with a large yaw angle have a low probability of occurrence, it can be concluded that the impact of the error is limited. On average (see section 4.6 for the definition of average) the difference between the results of the analytical and numerical model are lower than 1 °.

The airfoil design and optimization has been carried out by employing the genetic multi-objective optimization tool Optiflow. Different relative thicknesses have been considered (24%, 35% and 18%) as well as different cost functions, which are listed below:

- 1) CF1 evaluates the maximum $\frac{C_l}{C_d}$ at the optimal angle of attack in the clean configuration while, CF2 evaluates the maximum $\frac{C_l}{C_d}$ across the operational angle of attack range in the rough configuration;
- 2) CF1 evaluates the maximum $\frac{C_l}{C_d}$ at the optimal angle of attack as a 50/50 trade-off between the performance in the clean and rough configuration as well as CF2 evaluates the the maximum $\frac{C_l}{C_d}$ across the operational angle of attack range, again as a 50/50 compromise between the performance in the clean and rough configuration;

- 3) A load-oriented optimization has been also carried out by using a CF1 which limits the C_l variations along with angle of attack variations over the operational angle of attack range, while the CF2 evaluates the the maximum $\frac{C_l}{C_d}$ across the operational angle of attack range as a 50/50 compromise between the performance in the clean and rough configuration.

The results of the **airfoil optimization** show:

- 1) Regarding geometry, a progressive shift in the maximum thickness location towards lower $\frac{x}{c}$ as well as a reduction of the camber can be observed moving from a one-point design in the clean configuration towards a probabilistic design in the rough configuration. Regarding the aerodynamic characteristics, moving from a point-design towards a probabilistic design, the maximum value of the Lift over Drag ratio decreases along with an increase in the width of the curve. Overall, large values of C_l have been noticed. In addition, it can be concluded that the more suitable results for wind energy application is given by compromising between the CF1 and CF2, indeed, those airfoils show a good agreement between large $\frac{C_l}{C_d}$, large distance between optimal and stall angle of attack and roughness insensitivity. As far as the latter is concerned, for a 35 % thick airfoil, the results suggest that the roughness insensitivity requirement should be implemented in the cost function, since poor performances in this sense have been detected.
- 2) Regarding geometry, the typical features of sharp leading edge nose and s-shaped lower surface tail can be observed. Moreover, with respect of the previous optimization, the location of the maximum thickness is shifted downstream. Such a shape results in a better roughness sensitivity agreement as well as a good delay in stall. The C_l values are still large, but lower than the previous optimizations. Finally, these results show a very good agreement with the DU91W2-250 airfoil.
- 3) Regarding geometry, the airfoils which present a relatively flat C_l polar over the operational angle of attack present the unique feature of thick trailing edges along with a minimum thickness location in the mid-chord position. Although, by comparing these results with the DU91W2-250, which shows a relatively flat Lift polar, it can be noticed that better solutions for such a goal can be found and consequently the cost-function definition or the optimization set-up should be modified.

7.2 Outlook

The analytical model for angle of attack fluctuations is based on the assumptions of steady aerodynamics as well as infinite blade stiffness (neglecting structural dynamics) and, in addition, no tower shadow effect is included. It has been found that these assumptions have an impact on the AoA fluctuations predictions and consequently including these phenomena (e.g. dynamic stall, aerodynamic damping, exc..) should increase the accuracy of the analytical model.

The final probability density function of the AoA fluctuations has been obtained by weighting the contribution of the combinations of HAWT operational parameters and wind perturbation sources, based on their probability of occurrence. The probability of occurrence of each parameter has been estimated based on real data; in particular the yaw misalignment probability is estimated based on the 'Slufterdam-West' onshore site data, while the probability of turbulence intensity is derived from the 'Gedser' near-coastal site and the 'Vindeby' offshore site data. These sites have been chosen because few studies on the probability of occurrence of yaw angle and turbulence intensity have been found in the literature. Consequently, different sites should be explored to obtain different probability density functions for yaw misalignment angle and turbulence intensity, to obtain a more accurate estimation of how likely these perturbation sources are expected to occur in practice.

References

[1] OECD, 2011, 'Environmental Outlook to 2050';

[2] P. K. Kundu, I.M. Cohen, 2002, Elsevier Science, 'Fluid Mechanics 2nd edition', ISBN: 0-12-178251-4;

[3] M. O. L. Hansen, 2008, 'Aerodynamics of Wind Turbine 2nd', ISBN 978-1-84407-438-9;

[4] J.F. Manwell, J.G. McGowan, WILEY, 2009, 'Wind Energy Explained: Theory, Design and Application Second Edition', ISBN: 978-0-470-01500-1;

[5] B.R. Munson et al, 2013, 'Fundamentals of Fluid Mechanics 7th', ISBN 978-1-118-11613-5;

[6] F. Mohebbi, M. Sellier, 2014, Journal of Aerodynamics, volume 2014, article ID 676912, 'On the Kutta Condition in Potential Flow over Airfoil';

[7] C.P. van Dam et al, 2008, SANDIA Report, DAND2008-1781, 'Trailing Edge Modifications for Flatback Airfoils';

[8] C.A. Consul et al, 2009, 8th European Wave and Tidal Energy Conference, 'Influence of Solidity on the Performance of a Cross-Flow Turbine'.

[9] S. Hosseinverdi, M. Boroomand, 2010, Conference Paper, DOI 10.2514/6.2010-4290, 'Prediction of Laminar-Turbulent Transitional Flow over Single and Two-elements Airfoils';

[10] J. L. van Ingen, 2008, AIAA 2008-3830, 38th Fluid Dynamic Conference and Exhibit, 'The e^n method for transiction prediction: Historical review of work at TU Delft';

[11] K. Kusunose, H. V. Cao, AIAA 1994-2376, 25th Fluid Dynamic Conference and Exhibit, 'Prediction of Transition Location for a 2-D Navier Stockes solver for multi-element airfoil configurations';

[12] P.J. Schmid, D.S. Henningson, 2001, 'Stability and Transition in Shear Flows';

[13] G.J. Leishman, G.L. Martin, 2002, Wind Energy 5:85-132, 'Challenges in Modelling the Unsteady Aerodynamics of Wind Turbines', DOI: 10.1002/we.62;

[14] S.A. Huyer et al, 1996, AIAA Journal, volume 34, 'Unsteady Aerodynamics associated with Horizontal-Axis Wind Turbine';

[15] R. Stull, 2017, 'Practical Meteorology: An Algebra-based Survey of Atmospheric Science, ISBN-13:978-0-88865-283-6;

[16] T. Mücke et al, 2011, Wind Energy 14:301-316, 'Atmospheric Turbulence and its Influence on the Alternating Loads on Wind Turbine';

[17] D. Veldkamp, 2006, DUWIND, 'Chances in Wind Energy: A Probabilistic Approach to Wind Turbine Fatigue Design', ISBN-13:978-90-76468-12-9;

[18] K.O. Ronold, G.C. Larsen, 2000, ELSEVIER, Engineering Structures 22 (2000) 656-574, 'Reliability-based design of Wind-Turbine Rotor Blade against Failure in Ultimate Loading';

[19] G.C. Larsen, 2001, Wind Energy, 4:107-120, 'Offshore Fatigue Design Turbulence', DOI: 10.1002/we.49;

[20] S. Goossens, 2015, Master Thesis of Science, TU Delft, 'Field-Test of Nacelle-based Lidar to explore its applications for Vattenfal as Wind Park Operator';

[21] G.C. Larsen, 2001, WIND ENERGY, 4:107-120, 'Offshore Fatigue Design Turbulence', DOI:10.1002/we.49;

[22] H. Snel, J.G. Schepers, 1992, Journal of Wind Engineering and Industrial Aerodynamics, 39, 267-281, 'Engineering Moles for Dynamic Inflow Phenomena';

[23] P. K. Chaviaropoulos, M. O. L. Hansen, 2000, Journal of Fluids Engineering, vol 122, pp330-360, 'Investigating three-dimensional and rotational effects on wind turbine blades by means of a quasi-3D Navier-Stokes solver';

[24] IEC 61400-1:2005(E), INTERNATIONAL STANDARDS, 2005, 'Wind Turbine - Part 1: Design Requirements';

[25] IEC 61400-3:2009-02, INTERNATIONAL STANDARDS, 2009, 'Wind Turbine - Part 3: Design Requirements for Offshore Wind Turbines';

[26] N.N. Sørensen, J. Johansen, 2007, European Wind Energy Conference and Exhibition, 'UPWIND, Aerodynamics and aero-elasticity; Rotor Aerodynamics in Atmospheric Shear Flow';

[27] J.T. Petersen et al, 1998, RISØ-R-1045(EN), 'Prediction of Dynamic Loads and Induced Vibrations in Stall', ISBN 87-550-2437-8;

[28] P. Fuglsang et al, 2004, Wind Energy, 7:145-162, 'Development of the RISØWind Turbine Airfoils';

[29] P.J. Schubel, R.J. Crossley, 2012, Energies, 5, 3425-3449, 'Wind Turbine Blade Design', DOI: 10.3390/en5093425;

[30] R.P.J.O.M. van Rooij, W.A. Timmer, 2003, AIAA 2003-50, 41st Aerospace Sciences Meeting and Exhibit, 'Roughness Sensitivity Considerations for Thick Rotor Blade Airfoils';

[31] L. Xiong et al, 2010, Wind Engineering Volume 34 no 5, pp 543-560, 'Dynamic Response Analysis of the Rotating Blade of Horizontal Axis Wind Turbine';

[32] R. Pereira et al, 2018, IOP Conf. Series: Journal of Physics 1037 (2018) 022042, 'Probabilistic Design of Airfoil for Horizontal Axis Wind Turbines';

[33] S. Boyd, L. Vandenberge, 2018, Cambridge University Press, 'Introduction to Applied Linear Algebra: Vectors, Matrixes and Least Squares', DOI:10.1017/9781108583664;

[34] R. B. Ash, 2008, DOVER PUBLICATIONS, INC. 'Basic Probability Theory';

[35] M.J. Evans, J.S. Rosenthal, 2009, 'Probability and Statistics: the Science of Uncertainty 2nd edition', ISBN-13: 978-1429224628;

[36] J.J. Gorgoso-Varela, A. Rojo-Alboreca, 2014, Annals of Forest Science, Springer Verlang/EDP Sciences, 71 (7), pp. 741-750, 'Use of Gumbel and Weibull functions to model extreme values of diameter distributions of forest stands'.

[37] J. G. Schepers, 2012, TU Delft, 'Engineering models in wind energy aerodynamics: Development, implementation and analysis using dedicated aerodynamic measurements', ISBN: 978-94-6191-507-8;

[38] M. P. van der Lan, M. C. Kelly, N.N. Sørensen, 2017, Wind Energy, 20, 479-489, A new k-ϵ method consistent with the Monin-Obunkhov similarity theory, DOI: 10.1002/we.2017.

[39] J.A. Businger et al, 1971, Journal of Atmospheric Science, 28, 181-189, Flux-profile relationships in the atmospheric surface layer.

[40] A.J. Dyer, 1974, Boundary-Layer Meteorology, 7, 363-372, A review of flux-profile relationships.

[41] X. Li et al, Wiley, 2017, Overall Design Optimization of Dedicated Outboard Airfoils for Horizontal Axis Wind Turbine Blades, DOI: 10.1002/we.2164

[42] F. Grasso, 2011, Journal of Aircraft, Vol 48 no 1, 'Usage of Numerical Optimization in Wind Turbine Airfoil Design', DOI: 10.2514/1.C031089;

[43] J.M. Jonkman, M.L. Buhl Jr, NREL, Techincal Report, NREL/EL-500-38230, 'FAST User's Guide';

[44] A. Manjock, Germanischer Lloyid WindEnergie, 2005, Evaluation Report no 72042, 'Design Codes FAST and ADAMS for Load calculations of Onshore Wind Turbines';

[45] J.M. Jonkman, 2003, NREL/TP-500-34755, Technical Report, 'Modeling of the UAE Wind Turbine for Refinement of FAST-AD';

[46] J.G. Leishman, T.S. Beddoes, 1989, Journal of the American Helicopter Society, 'A Semi-Empirical Model for Dynamic Stall';

[47] J.G. Leishman, Cambridge Aerospace Series, 2016, 'Principles of Helicopter Aerodynamics Second Edition';

[48] A. Suzuki, A.C. Hansen, 1999, AIAA-99-0041, 'Generalized Dynamic Wake Model for YawDyn';

[49] D. M. Pitt, D. A. Peters, Sixth European ROtor Aircraft and Powered Lift Aircraft Forum, Paper no 47, 'Theoretical Prediction of Dynamic-Inflow Derivatives'.

[50] L. Andersen, S.R.K. Nielsen, 2008, 'Elastic Beam in Three Dimensions', ISSN: 1901-7286;

[51] B. M. Kulfan, 2007, Fourth International Conference on Flow Dynamics, 'CST Universal Parametric Geometry Representation Method with Applications to Supersonic Aircraft';

[52] G. de Oliveira, 2011, TU Delft Master Thesis, 'Wind Turbine Airfoils with Boundary Layer Suction: A Novel Design Approach';

[53] W. Banzhaf, 1994, Springer, Berlin, pp. 322-332, 'Genotype-Phenotype-Mapping and Neutral Variation - A Case Study in Genetic Programming';

[54] R. Pereira, 2016, TU Delft Phd Thesis, 'Active Stall Control of Horizontal Axis Wind Turbine: A Dedicated Study with Emphasis on DBD Plasma Actuators', ISBN 978-94-6299-417-1;

[55] F. Grasso, O. Ceyhan, 2014, Journal of Physics Conference Series 524(1):012030, 'Usage of Advanced Thick Airfoils for the Outer Part of Very Large Offshore Turbines', DOI: 10.1088/1742-6596/524/1/012030.

[56] D.K. Chaturvedi et al, 1999, Elsevier, Electrical Power and Energy System 21, 405-415, 'Load Frequency Control: a generalised neutral network approach';

[57] G. De Oliveira, R. Pereira, N. Timmer, R. Van Rooij, 2018, Journal of Physics: Conference Series, 1037(2), [022009], 'Improved airfoil polar predictions with data-driven boundary layer closure relations', DOI: 10.1088/1742-6596/1037/2/022009;

[58] G. S. T. A. Bangga et al. 2015, 11th EAWE PhD Seminar on Wind Energy in Europe, 'An Examination of Rotational Effects on Large Wind Turbine Blades';

[59] M. Paz, J.H. Kim, 2019, Springer, 'Structural Dynamics: Theory and Computation 6th edition', ISBN: 978-3-319-94742-6;

[60] R. Pereira, Universidade Técnica de Lisboa Master Thesis, 2010, 'Validating the Beddoes-Leishman Dynamic Stall Model in the Horizontal Axis Wind Turbine Environment'.

Appendix A

Combined Perturbation Sources Validation Gallery

A.1 Offshore Scenario

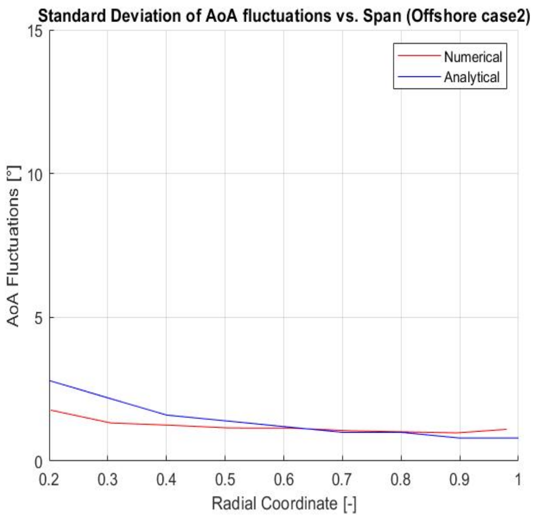

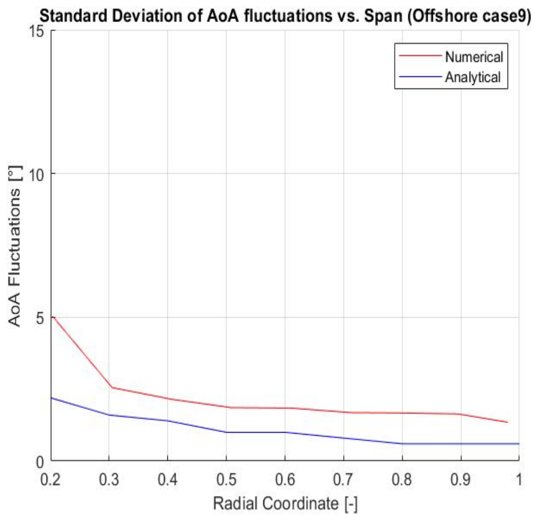

Figure A.1: *Standard deviation of the AoA fluctuations for the Offshore site case 2 (TSR=7[-], I=0.12[-],* β*=0[°] and* z_0*=0.0002[m]) (a) and for the Offshore site case 9 (TSR=7[-], I=0.10[-],* β*=20[°] and* z_0*=0.0002[m])(b)*

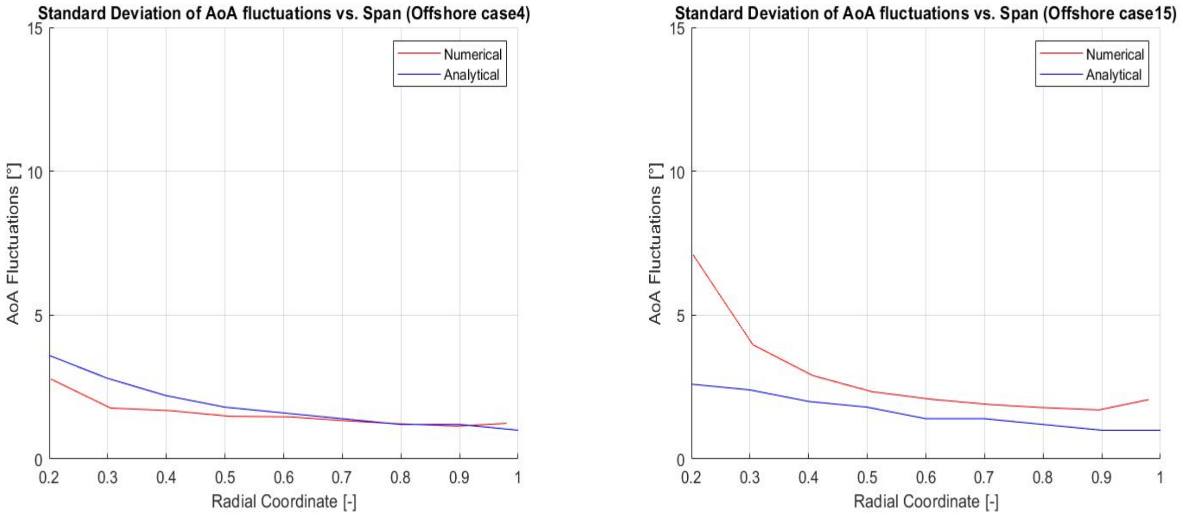

Figure A.2: *Standard deviation of the AoA fluctuations for the Offshore site case 4 (TSR=7[-], I=0.16[-], β=0[°] and z_0=0.0002[m]) (a) and for the Offshore site case 15 (TSR=5[-], I=0.10[-], β=20[°] and z_0=0.0002[m])(b)*

A.2 Near-Coastal Scenario

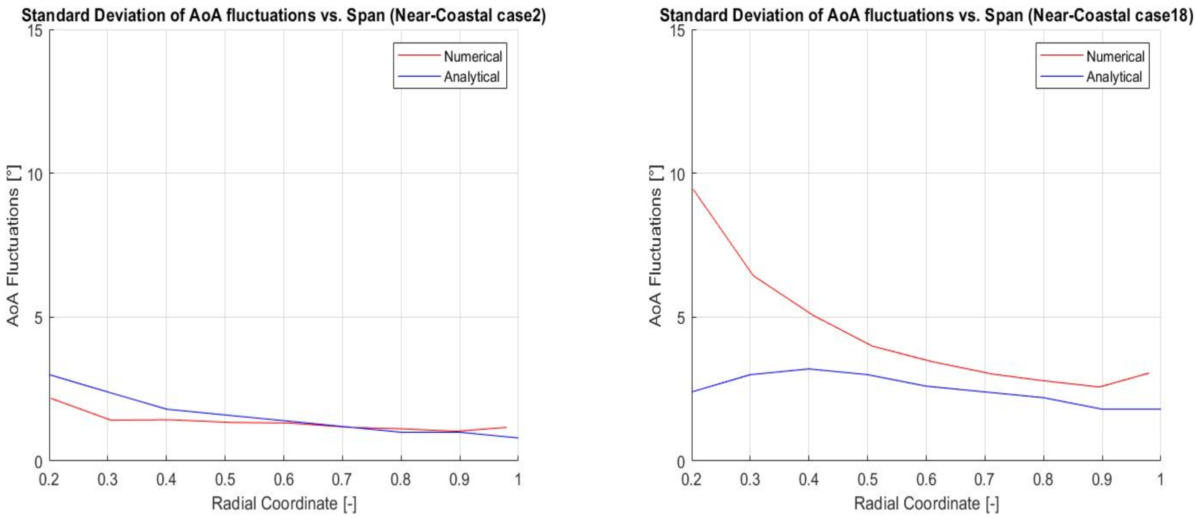

Figure A.3: *Standard deviation of the AoA fluctuations for the Near-Coastal site case 2 (TSR=7[-], I=0.14[-], β=0[°] and z_0=0.005[m]) (a) and for the Near-Coastal site case 18 (TSR=3[-], I=0.12[-], β=20[°] and z_0=0.005[m])(b)*

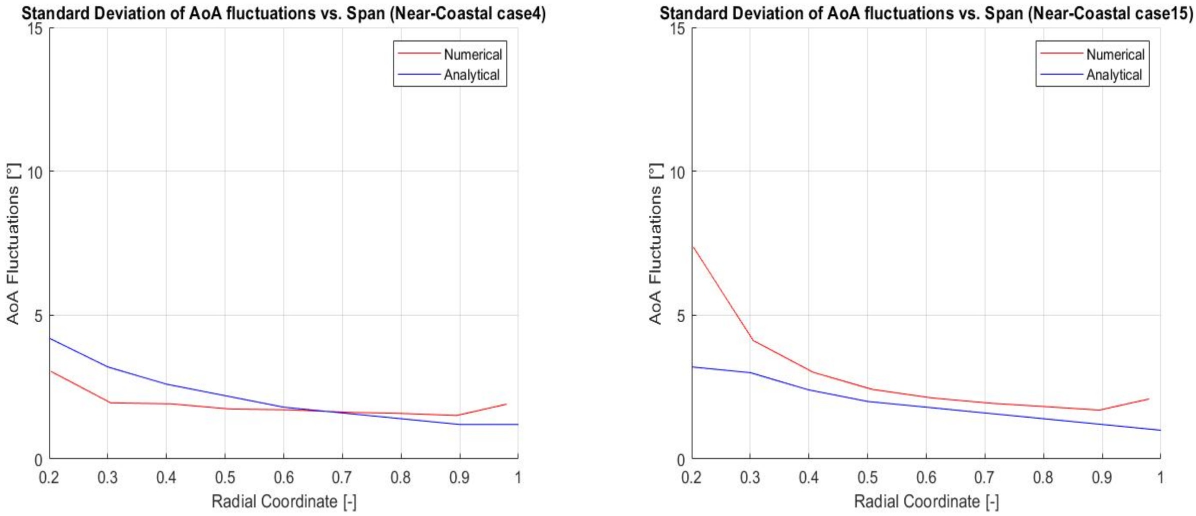

Figure A.4: *Standard deviation of the AoA fluctuations for the Near-Coastal site case 4 (TSR=7[-], I=0.18[-], β=0[°] and z_0=0.005[m]) (a) and for the Near-Coastal site case 15 (TSR=5[-], I=0.12[-], β=20[°] and z_0=0.005[m])(b)*

A.3 Onshore Scenario

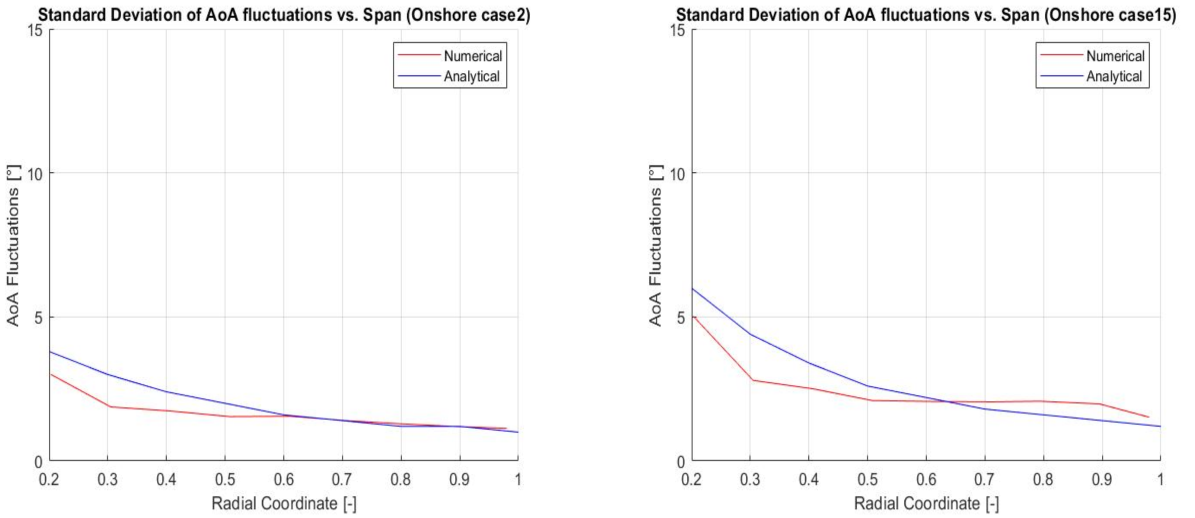

Figure A.5: *Standard deviation of the AoA fluctuations for the Onshore site case 2 (TSR=7[-], I=0.175[-], β=0[°] and z_0=0.1[m]) (a) and for the Onshore site case 15 (TSR=7[-], I=0.25[-], β=20[°] and z_0=0.1[m])(b)*

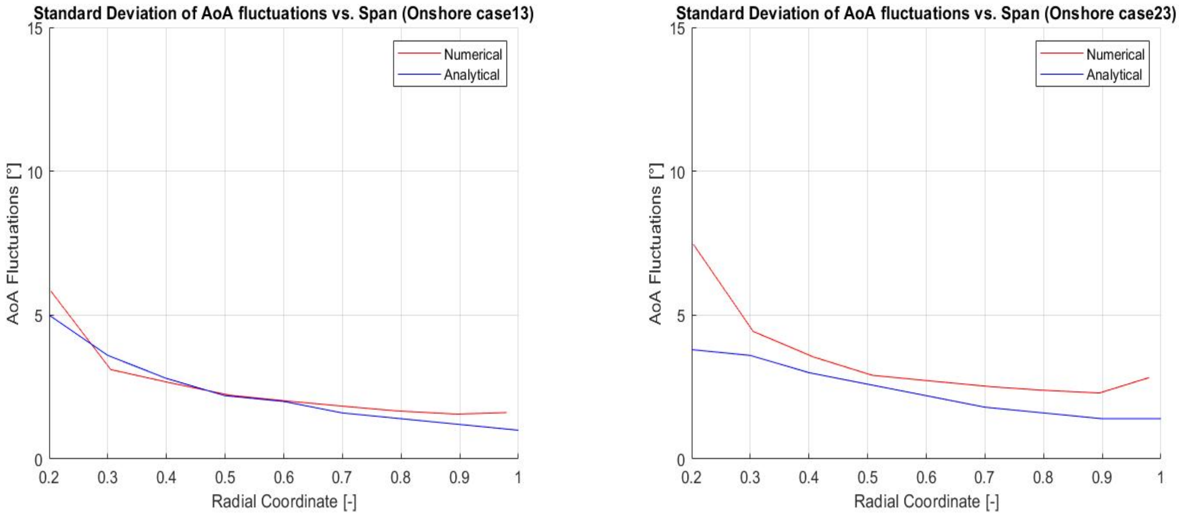

Figure A.6: *Standard deviation of the AoA fluctuations for the Onshore site case 13 (TSR=7[-], I=0.200[-],* β*=20[°] and* z_0*=0.1[m]) (a) and for the Onshore site case 23 (TSR=5[-], I=0.14[-],* β*=20[°] and* z_0*=0.1[m])(b)*

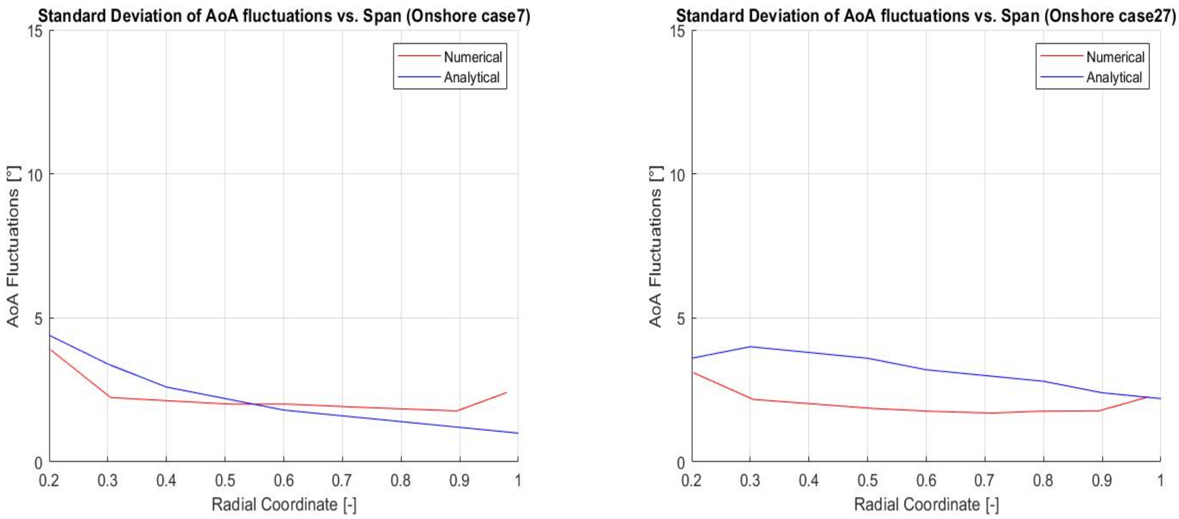

Figure A.7: *Standard deviation of the AoA fluctuations for the Onshore site case 7 (TSR=7[-], I=0.175[-],* β*=10[°] and* z_0*=0.1[m]) (a) and for the Onshore site case 27 (TSR=3[-], I=0.14[-],* β*=0[°] and* z_0*=0.1[m])(b)*

Appendix B

Optiflow Results Gallery

B.1 Influence of Constraints of Airfoil Geometry

B.1.1 Influence of constraining the upper surface concavity

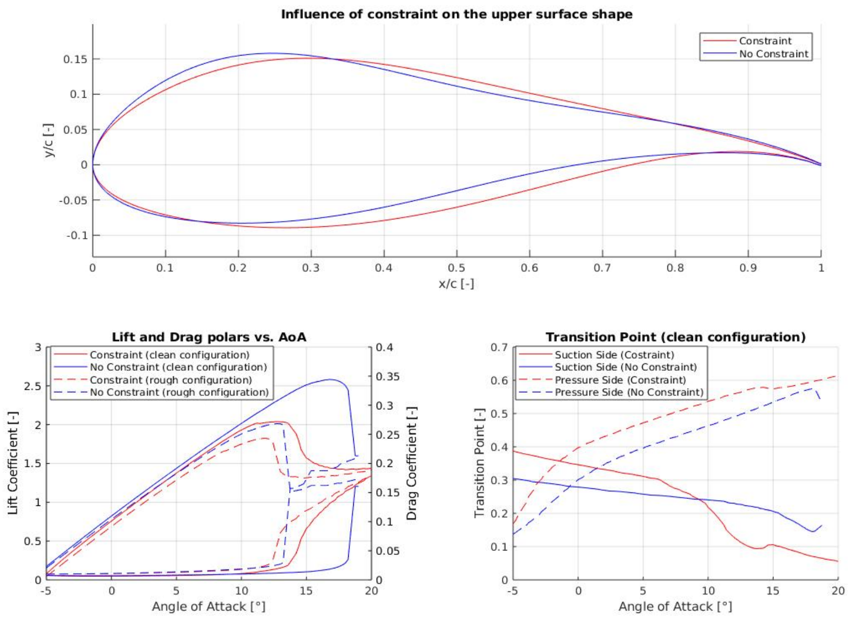

Figure B.1: *Influence of allowing a concave down shape only for the upper airfoil surface on the airfoil geometry. This results have been obtained by using a CF1* $=CF1_{LD}$ *and CF2* $= CF2_{LD}$

B.1.2 Influence of constraining the minimum optimal Angle of Attack

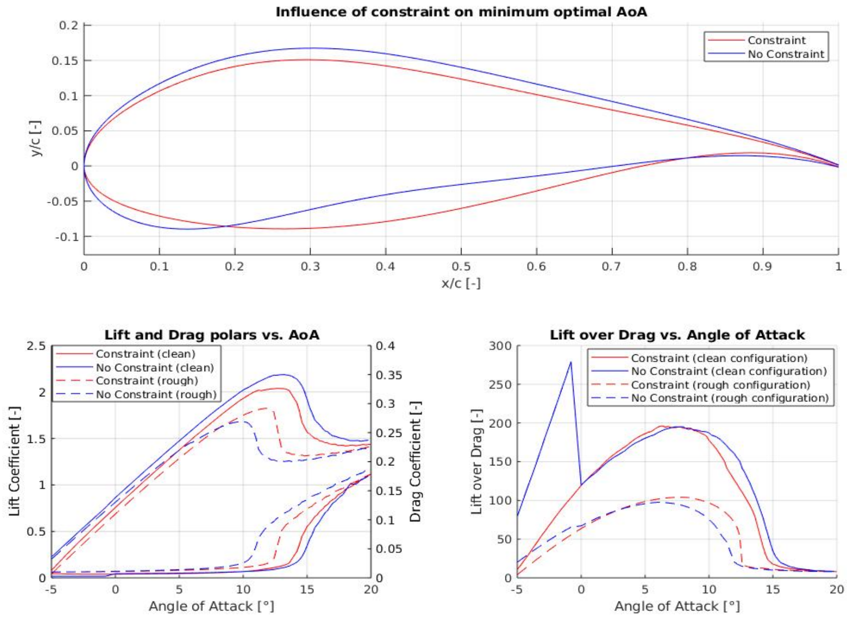

Figure B.2: *Influence of allowing a positive minimum optimal angle of attack only on the airfoil geometry. This results have been obtained by using a CF1 =*$CF1_{LD}$ *and CF2 =* $CF2_{LD}$

B.2 Alternative Results for a 35 % thick airfoil

B.2.1 Modification of the main Cost Function

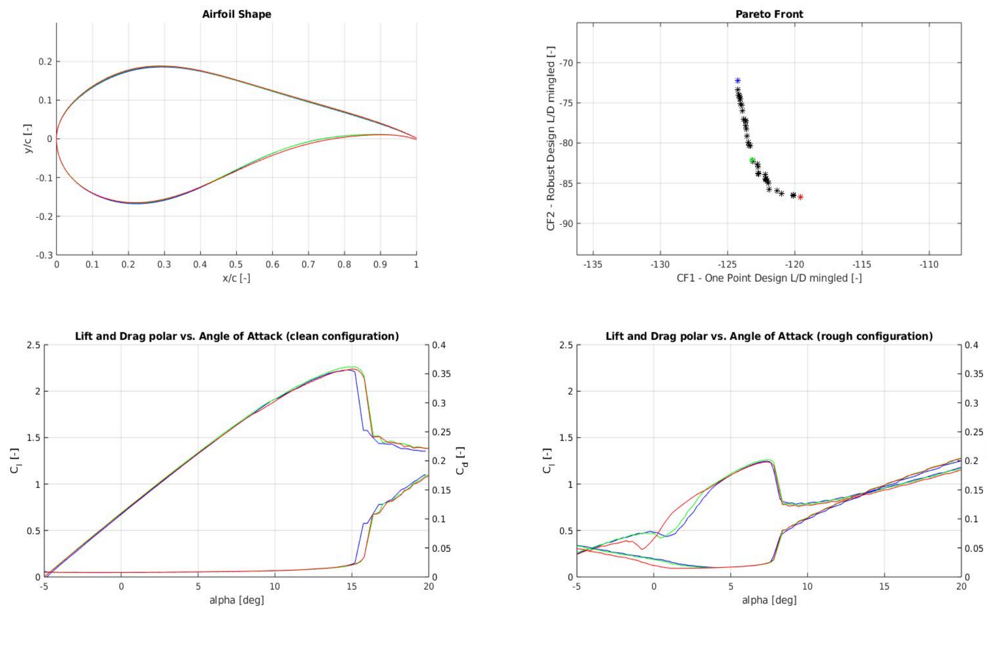

Figure B.3: *Results for a 35% thick airfoil obtained by using a CF1 =* $CF1_{LD}$ *and a CF2 =* $CF2_{LD}$

B.2.2 Load-oriented Cost Function

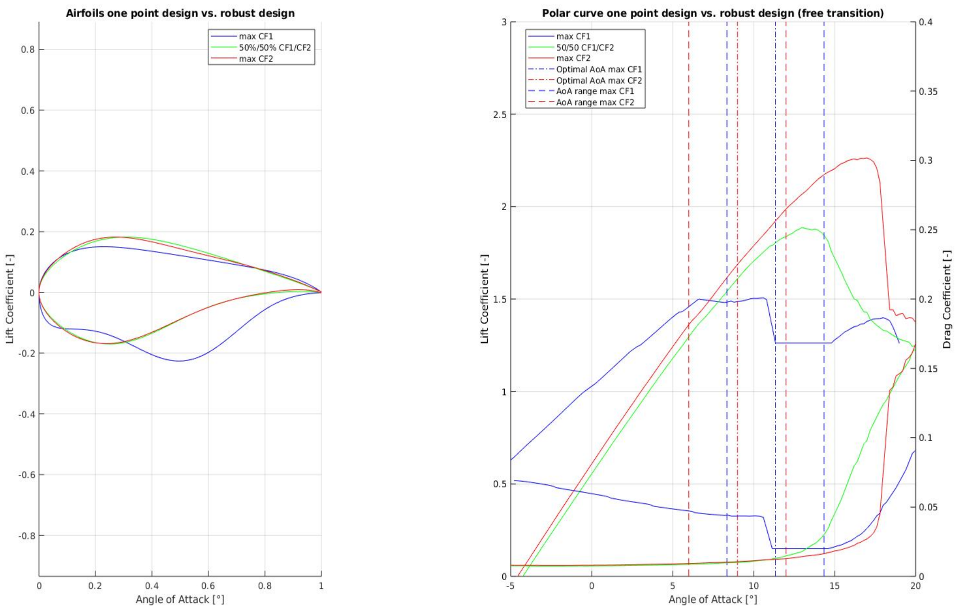

Figure B.4: *Results for a 35% thick airfoil obtained by using a CF1* $= CF1_{load}$ *and a CF2* $= CF2_{LD}$